Faculty of Sciences
Department of Physics and Astronomy

Light Curve Modelling of Novae at Soft X–Ray Energies

by

Bert VANDER MEULEN

Promoter: prof. dr. Maarten BAES
Co–promoter: dr. Peter CAMPS

A thesis submitted in fulfilment of the requirements
for the degree of Master of Science in Physics and Astronomy

Academic year: 2019 – 2020

Acknowledgements

My final academic year started mid–August 2019 in sunny Madrid, on the bus to Villafranca del Castillo, where I was offered the unique opportunity to work for six months at the European Space Astronomy Centre (*ESAC*). Supervised by the most dedicated *ESAC* scientist Jan–Uwe Ness, I could focus on full–time astronomical research in the most stimulating environment a young scientist could imagine. I would like to thank Jan–Uwe for introducing me to the wonderful world of novae, for sharing his insights and motivating me to work hard; for the training to become a "real scientist". I liked how he was always in a good laugh, and in for a talk, and I do look forward to our future collaborations. Those six months in Spain flew by, and I will remember those that were there with me: Diego, Zsofi, Alex, Mara, David, Anna and many more amazing people. You guys made my *ESAC* experience unforgettable. The daily Madrid–*ESAC* rides with Diego, listening to some Spanish rock music while being stuck on *el camino*, took a lot of time but were definitely fun.

I would like to thank my promoter Maarten Baes and co–promoter Peter Camps, for their quick and comprehensive feedback, for their interests in and remarks on my work, and for supporting me while writing a thesis on novae, which was quite off the UGent expertise. During my university studies, they both were the incredible lecturers to my favourite courses, and their contributions to this thesis are more extensive than the direct feedback during the last couple of months. In particular, they developed the amazing *SKIRT* code; I do hope to contribute to the *SKIRT*–team in the near future.

I am grateful for my parents, Hannelore and Bjarne, who took the time to double–check my English spelling. I do understand that it is not obvious to follow the flow of a story on novae, and all their efforts were very much appreciated. Above all, I would like to thank my parents for the opportunity to study, and even more to motivate and support me during these studies; it all meant a lot to me. I really liked forest walks with Hannelore during the last weeks of writing, and I would like to thank her for all the support, motivation and tips. Post–thesis and post–corona, I look forward to spending upcoming summer with my friends and girlfriend.

Bert Vander Meulen, June 2020

Summary

Novae are explosive outbursts on the surface of a white dwarf star in a close binary system. On the night sky, they appear as new stars (Latin: stella nova), which then fade over weeks, months or years. Novae are powered by hydrogen burning on the white dwarf surface, and once the obscuration in the nova system drops, this nuclear burning is observed as a bright source of soft X–ray emission. X–ray missions such as *Swift* and *XMM–Newton* are used to observe novae during this so–called SSS–phase (SSS: supersoft X–ray source).

This work focuses on observational data from novae during their SSS–phase, as observed with the *Swift* and *XMM–Newton* space missions. SSS–spectra from novae show an atmospheric continuum component between 0.3 and 0.7 keV, with corresponding light curves in soft X–rays that are highly variable. These light curves contain information on the clumpy structure of the ejecta which were expelled at the nova eruption, and by modelling their variability, one could derive system parameters for the underlying nova system. For this study, a flexible light curve simulation code named *DaRT* was developed, which combines binary dynamics with advanced Monte Carlo radiation transfer (*DaRT*: Dynamics and Radiative Transfer).

Three different novae were studied in great detail, focusing on their observational X–ray data: the recurring nova U Sco, the classical nova V5116 Sgr, and the symbiotic nova V3890 Sgr. For each of these novae, a geometric light curve model was presented and thoroughly tested using the *DaRT* simulation code. For V5116 Sgr, we found the first well–motivated model to explain the enigmatic soft X–ray light curve since its observation in 2007. The U Sco light curve contained clear evidence for the presence of an accretion disk corona, while the light curve model was based on the accretion disk reformation as soon as 22 days after the nova outburst. For V3890 Sgr, the light curve model allowed us to better understand the messy environment around the white dwarf star after the nova outburst, and provided information on the detailed clumpy structure of the ejecta.

Samenvatting

Novae zijn explosieve uitbarstingen op witte dwergsterren die deel uitmaken van een dubbelstersysteem. Aan het hemelgewelf verschijnen deze als nieuwe sterren (Latijn: stella nova), die vervolgens vervagen over enkele weken, maanden of jaren. Novae worden aangedreven door waterstofverbranding op het oppervlak van de witte dwergster, en eens het systeem voldoende transparant is, kan deze kernverbranding waargenomen worden als een heldere bron in zachte röntgenstralen. Met röntgenmissies als *Swift* en *XMM–Newton* observeert men novae tijdens deze zogenaamde SSS–fase (Engels: supersoft X–ray source, SSS).

Dit werk focust op observationele data van novae tijdens hun SSS–fase, zoals deze is waargenomen met de *Swift* en *XMM–Newton* ruimtemissies. SSS–spectra van novae vertonen een atmosferische continuüm component tussen 0.3 en 0.7 keV, met bijhorende lichtcurves in zachte röntgenstralen die hoogst variabel zijn. Deze lichtcurves bevatten informatie over de klonterige structuur van de ejecta die zijn uitgestoten bij de nova uitbarsting, en door hun variabiliteit te modelleren, wordt het mogelijk om systeemparameters af te leiden voor het onderliggende dubbelstersysteem. Voor deze studie werd een flexibele lichtcurve simulatiecode ontworpen, die dubbelster–dynamica combineert met Monte Carlo stralingsoverdracht, genaamd *DaRT*(Engels: Dynamics and Radiative Transfer, *DaRT*).

Drie verschillende novae werden uitgebreid bestudeerd aan de hand van hun observationele data: de terugkerende nova U Sco, de klassieke nova V5116 Sgr, en de symbiotische nova V3890 Sgr. Ten slotte werd voor elk van deze novae een geometrisch model voor hun lichtcurve voorgesteld, en grondig getest door middel van simulaties met de *DaRT* code. Voor V5116 Sgr vonden we een fyschisch gemotiveerd model, het eerste dat de raadselachtige lichtcurve in zachte röntgenstralen verklaart sinds de waarneming in 2007. De U Sco lichtcurve duidde op de aanwezigheid van een accretieschijfcorona, terwijl het lichtcurve model was gebaseerd op de heropbouw van de accretieschijf, 22 dagen na de nova uitbarsting. Voor V3890 Sgr stelde het lichtcurve model ons in staat om de chaotische omgeving rond de witte dwergster na de nova uitbarsting beter te begrijpen, en voorzag het informatie over de gedetailleerde klonterige structuur van de ejecta.

Contents

Chapter 1

Novae at Soft X–Rays

1.1 Classical novae

1.1.1 Introduction

Classical novae are thermonuclear outbursts on the surface of a white dwarf star that is accreting material from an evolved binary companion. Both stars are orbiting each other closely with a period between two and ten hours, and form a so–called interacting binary system: the evolved companion star has filled its Roche lobe, and gradually loses part of its hydrogen–rich outer layers, which are then accreted onto the white dwarf surface by formation of an accretion disk. This transfer of H–rich material continues until the accumulated shell of hydrogen reaches critical density and temperature conditions for nuclear fusion into helium. In a degenerate surface layer on top of the compact white dwarf core, the system will ignite in a thermonuclear runaway, which is observed as a classical nova. During this nova outburst, the emission output of the system is increased tremendously, and the source might appear as a new star on the night sky. Hence the name "nova", a Latin term which was coined by Tycho Brahe as title for his book *De Stella Nova* (about the new star).

In our Milky Way, about 30% of all stars form binaries, with over half of these systems being close enough to allow mass transfer by Roche lobe overflow (Vanbeveren, 2000). Interacting binaries with an accreting white dwarf star form the so–called group of *cataclysmic variables* (CVs), and often exhibit highly variable behaviour on short time scales, associated to fluctuations in the accretion onto the white dwarf star. Classical novae are just one type of outburst that could be observed in CV–systems. Other phenomena, expected in cataclysmic variables, are dwarf novae, when accretion disk instabilities temporarily enhance the accretion onto the compact white dwarf. About 25% of the CVs have highly magnetic white dwarf primaries, with magnetic fields that could influence the accretion flow (Bode & Evans, 2008). Systems with intermediate magnetic field strengths will have truncated accretion disks, while the strongest *polars* will guide the accretion stream directly towards the white dwarf poles and prevent the formation of a disk. In this work, we consider novae in cataclysmic variables with non–magnetic white dwarf primaries, and fully developed accretion disks.

It is believed that with the initial blast of the nova outburst, the accretion disk around the white dwarf star is destroyed (Drake & Orlando, 2010). In addition, a large fraction of the accumulated hydrogen is expelled from the white dwarf surface, in an optically thick shell of ejecta which obscures the central source of emission. As the accreted hydrogen did partly diffuse into the white dwarf surface before the eruption, these ejecta contain white dwarf core material, drenched up by Kelvin–Helmholtz instabilities (Casanova et al., 2011). The residual hydrogen on the white dwarf surface continues its nuclear burning for weeks, months, or years, which powers the nova radiation output, see subsection 1.1.2. During the early phases of the nova outburst, the total luminosity exceeds the Eddington limit, which radiatively drives an optically thick wind. Later, clumps could form in the surrounding ejecta by UV line–driven winds. Once the residual hydrogen burning ceases and the nova turns off, the system returns to hydrostatic equilibrium. As accretion sets in again and hydrogen accumulation continues, a next outburst could be expected on timescales of 10^4–10^5 yr, depending on the CV accretion rate (Ness et al., 2012).

1.1.2 Spectral evolution

During the nova outburst, the emission output produced by nuclear burning on top of the white dwarf surface is released through complex radiative transfer in the expanding ejecta. In this subsection, the spectral evolution of classical novae will be discussed, focusing on the origin and appearance of supersoft X–ray emission in the final stages of the outburst. Pre–outburst, the white dwarf is accreting hydrogen–rich material from its companion star, and the system is observed as a cataclysmic variable in quiescence: the optical spectra show an evolved companion star plus a white dwarf atmosphere, while variable hard X–ray emission traces ongoing accretion.

When the accumulated hydrogen layer reaches critical conditions for nuclear fusion into helium, the white dwarf surface ignites in a thermonuclear runaway. The explosive turn–on of hydrogen fusion causes part of the H–rich material to be ejected, mixed with drenched–up white dwarf core material. These ejecta form a dense shell, obscuring the residual hydrogen burning on the surface of the white dwarf core. Radiation emerging from this optically thick shell is observed as thermalised optical emission, with blue–shifted absorption lines caused by the NLTE radiative transfer through the expanding ejecta. Additional shock emission could be observed at hard X–rays when the ejecta collide with the surrounding material in the nova system. As the ejecta continue to expand and the obscuring shell thins, gradually one can see deeper into the system, i.e. closer to the central hydrogen burning. The photospheric radius of the nova system (where the optical depth $\tau = 1$) decreases over time, while its spectra shift towards higher photon energies at a constant bolometric luminosity. Increasingly harder radiation is observed, evolving from optical over NUV to FUV emission.

As the ejecta expand even more, the obscuring shell starts to clear, while the photospheric radius shrinks to coincide with the white dwarf core radius. The nova is observed as a supersoft X–ray source (SSS), with spectra resembling the persistent supersoft X–ray sources like Cal 83 and Cal 87, which steadily burn their accreted hydrogen (van den Heuvel et al., 1992). Supersoft X–ray sources are empirically defined as the class of soft X–ray emitters whose spectra resemble the

spectra of black body sources in the effective temperature range of 300–700 kK, with luminosities above 10^{35} erg s^{-1} (Greiner, 1996). This SSS–emission will be observed as a bright continuum in the 0.3–0.7 keV supersoft X–ray range (see subsection 1.2.2), and emerges from the compact surface layer on the white dwarf core, which is still burning residual hydrogen (Kahabka & van den Heuvel, 1997). The hot CNO–nuclear burning is not observed directly, but is slightly reprocessed by radiative transfer through the thin white dwarf atmosphere, causing the energy produced by H–fusion to thermalise and escape at SSS–energies. SSS–spectra can be reproduced reasonably well by the static *TMAP* hot white dwarf atmosphere models (Rauch et al., 2010), while better results can be obtained with expanding radiative transfer models based on the *PHOENIX* code (van Rossum, 2012). To a first approximation, the SSS–continuum emission can be described by a black body spectrum of $T_{\rm eff} \approx 500$ kK, see subsection 1.2.1. The SSS–phase lasts until the residual hydrogen content is consumed, which can take between several days and multiple years. It is predicted that the total duration of this SSS–phase is closely connected to the white dwarf primary mass. Once the ejecta have cleared, the binary accretion can set in again, which could happen before or after the SSS–phase turn–off. The nova system returns to quiescence, and will be observed as a cataclysmic variable.

1.1.3 Importance of novae

Classical novae are powerful outbursts in close binary systems, that are worthwhile studying for various reasons. As novae occur on accreting white dwarfs, they signal supernova Ia (SNIa) progenitor candidates in the so–called single–degenerate model (Whelan & Iben, 1973; Nomoto, 1982). Taking into account the accretion rate and total mass lost to the ejecta, one could determine whether or not the compact white dwarf is getting more massive over time and grows towards the Chandrasekhar mass limit. White dwarf stars can either have a carbon–oxygen (CO) or oxygen–neon–magnesium (ONeMg) composition, but only the CO–white dwarfs have enough nuclear binding energy to ignite as a SNIa. Nova systems are well–suited laboratories for studying white dwarf elementary properties such as their composition, as a fraction of the white dwarf core material will be drenched up by the nova outburst and could be identified in their spectra. Other white dwarf parameters such as their mass can be estimated from the binary motion, as well as from the critical conditions for thermonuclear runaway and the total duration of the SSS–phase, which both explicitly depend on this primary mass. By modelling the SSS–variability, one could obtain system parameters such as the stellar radii, and learn about the detailed structure of the ejecta.

During the SSS–phase, the residual hydrogen burning on top of the white dwarf surface is revealed, which offers the opportunity to study the physics of nuclear burning, a process that is otherwise deeply buried inside stars. Novae are the most luminous sources of soft X–ray emission in the Universe. As they temporarily illuminate part of the interstellar medium (ISM), they allow for studies on the ISM composition using soft X–ray features: e.g. the atomic data on interstellar CII and CIII were recently refined based on absorption lines in nova spectra (Gatuzz et al., 2018). In addition, nova outbursts inject processed material into the ISM. Nova ejecta containing enriched gas might be the main contribution to galactic ^{13}C, ^{15}N, ^{17}O (José et al., 2006) and ^{7}Li (Starrfield et al., 2020), while

IR observations of novae reveal dust formation processes (Gehrz et al., 1998). The optical light curves of novae fade over weeks, months or years, and empirically, a clear relation has been found between the maximum absolute magnitude at the outburst, and the total times for two and three magnitudes decay from this maximum. Consequently, the optical light curves of novae in outburst can be used to estimate the distance towards galaxies, as part of the cosmic distance ladder.

We discussed how soft X–ray observations during the SSS–phase of novae are interesting in their own right, but furthermore contain information on the physics of nuclear burning, and provide elementary white dwarf and binary system parameters. It is fortunate how the absorbed photospheric SSS–emission peaks in the energy range where the two most advanced X–ray observatories *XMM–Newton* and *Chandra* have their high–resolution grating instruments operating. As novae are the brightest sources in this soft X–ray range, they are the optimal target for these observatories, and therefore they have been studied thoroughly in large numbers. In the next section, we will introduce a selection of topics from observational X–ray astronomy, focusing on soft X–ray observations of the SSS–phase in novae.

1.2 X–ray astronomy

1.2.1 Soft X–ray spectra

In subsection 1.1.2, we discussed how novae evolve towards supersoft X–ray sources (SSS) during their outburst. Throughout this SSS–phase, the residual hydrogen burning on top of the white dwarf surface is observed, with black body–like emission at $T_{\text{eff}} \approx 500$ kK. The spectrum of a black body source is described by the Planck function $B_{\nu,T}$:

$$B_{\nu,T} = \frac{2h\nu^2}{c^2} \frac{1}{e^{\frac{h\nu}{kT}} - 1}, \tag{1.1}$$

which is defined such that the specific luminosity $L_{\nu,T}$ equals:

$$\begin{aligned} L_{\nu,T} &= \int_{2\pi} d\Omega \int_A (\vec{n} \cdot d\vec{A})\, B_{\nu,T} \\ &= \int_0^{\frac{\pi}{2}} d\theta \sin\theta \cos\theta \int_0^{2\pi} d\phi \int_A dA\, B_{\nu,T} \\ &= 4\pi^2 R^2 B_{\nu,T}, \end{aligned}$$

with R the white dwarf photospheric radius, and $\vec{n} \cdot d\vec{A}$ the cosine factor for a Lambertian emitter. Consequently, the observed flux $\mathcal{F}_{\nu,T}$ at a distance d is:

$$\begin{aligned} \mathcal{F}_{\nu,T} &= \frac{L_{\nu,T}}{4\pi d^2} \\ &= \frac{L_T}{d^2} \frac{B_{\nu,T}}{4\sigma T^4}, \end{aligned} \tag{1.2}$$

with $L_T = 4\pi R^2 \sigma T^4$ the Stefan–Boltzmann law for the total luminosity L_T, with Stefan's constant σ:

$$\sigma = \frac{2\pi^5 k^4}{15 c^2 h^3}.$$

X–ray instruments detect the incoming photon flux $F_{E,T}$ in counts s^{-1} cm^{-2} keV^{-1}, which is related to the flux $\mathcal{F}_{\nu,T}$ in erg s^{-1} cm^{-2} Hz^{-1} as:

$$\begin{aligned} F_{E,T} &= \frac{dN}{dA\ dt\ dE} \\ &= \frac{d\varepsilon/h\nu}{dA\ dt\ hd\nu} \\ &= \frac{\mathcal{F}_{\nu,T}}{h^2\nu}. \end{aligned}$$

Combined with Equation 1.2 and the Planck function in Equation 1.1, one finds:

$$F_{E,T} = \frac{L_T}{d^2}\left(\frac{k^4}{2c^2h^3\sigma}\right)\frac{1}{(kT)^4}\frac{E^2}{e^{\frac{E}{kT}}-1},$$

with $E = h\nu$ the incoming photon energy. Substituting Stefan's constant, and expressing the total luminosity as L_{39} in units of 10^{39} erg s^{-1} (i.e. $6.24 \cdot 10^{47}$ keV s^{-1}), and the distance as D_{10} in units of 10 kpc (with 100 kpc^2 $= 9.52 \cdot 10^{44}$ cm^2), we obtain a photon flux of:

$$\begin{aligned} F_{E,T} &= \left(\frac{L_{39}}{D_{10}^2}\right)\frac{6.24 \cdot 10^{47}\ \text{keV}}{9.52 \cdot 10^{44}\ \text{cm}^2\ \text{s}}\frac{15}{4\pi^5}\frac{1}{(kT)^4}\frac{E^2}{e^{\frac{E}{kT}}-1} \\ &= \left(\frac{L_{39}}{D_{10}^2}\right)\frac{E^2}{(kT)^4}\frac{8.0525}{e^{\frac{E}{kT}}-1}\frac{\text{keV}}{\text{cm}^2\ \text{s}}. \end{aligned} \tag{1.3}$$

Using this equation for the photon flux F as a function of the incoming photon energy E, one could constrain the effective temperature kT and the normalisation constant L_{39}/D_{10}^2 from observational data on the nova spectrum. If the distance towards the nova system is uncertain, the total luminosity L will usually be expressed as "per $(10\ \text{kpc})^2$".

1.2.2 Photoionisation

During their SSS–phase, the global spectra of novae resemble a black body curve at $T_{\text{eff}} \approx 500$ kK. However, these SSS-spectra are not observed in their intrinsic black body shape, as soft X–ray photons are severely affected by K–shell photoionisation (i.e. a bound inner–shell–electron in the transfer medium is liberated by absorption of a high energy photon). This radiative process introduces additional substructure in the observed spectra of novae, and occurs both locally and inside the interstellar medium. Absorption by photoionisation of a certain ionic species is characterised by the energy–dependent photoionisation cross section $\sigma_i(E)$ for this ion, and its column density N_i.

The photoionisation cross sections for neutral carbon CI, nitrogen NI and oxygen OI are shown in the top panel of Figure 1.1, with atomic data from Elam et al. (2002). These cross sections are zero below the ionisation potential for each element, i.e. when the incoming photon has too little energy to liberate an electron. The cross sections peak at the ionisation potential, and thereafter decrease exponentially with increasing photon energy, i.e. when the photon has too much kinetic energy to efficiently interact with a bound electron. Note how the CI, NI and OI ionisation potentials at soft X–ray energies correspond to K–shell photoionisation, i.e. an inner–shell electron is liberated from the

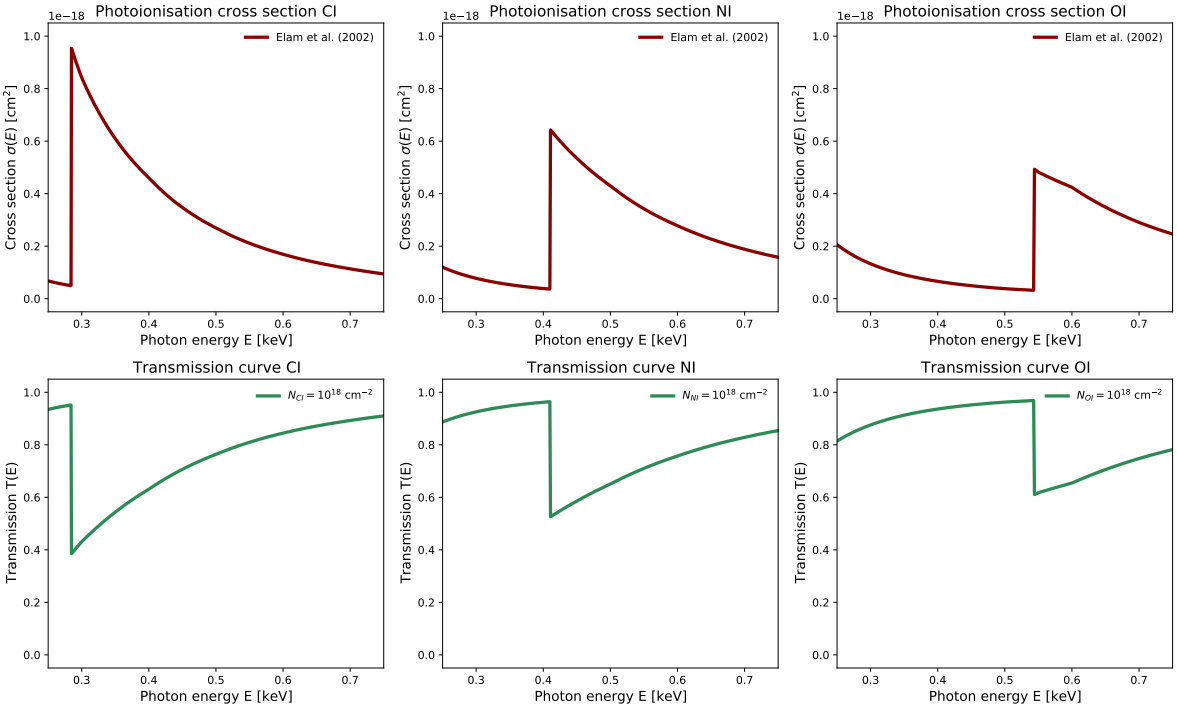

Figure 1.1: (top) Photoionisation cross sections for neutral carbon CI, nitrogen NI and oxygen OI, with atomic X–ray data from Elam et al. (2002). (bottom) The corresponding transmission curves.

neutral atom. Photoionisation of outer–shell electrons occurs at lower energies, and the exponential tail of their cross sections can be observed in the top panel of Figure 1.1.

A source spectrum $F_0(E)$, which passes through a medium of ions i with a column density N_i, will be observed as $F(E) = F_0(E) \cdot e^{-N_i \cdot \sigma_i(E)}$. The energy–dependent transmission curves $T(E) = e^{-N_i \cdot \sigma_i(E)}$ for a medium of neutral CI, NI and OI are shown in the bottom panel of Figure 1.1. Photon energies below the ionisation potential are not affected by photoionisation, while at higher energies, photons are partially absorbed depending on the cross section $\sigma_i(E)$ and column density N_i. Usually, one assumes a galactic composition for the transfer medium, and characterises the overall absorption by just one free parameter N_H, with all abundances set relative to this neutral hydrogen. However, one frequently has to correct the C, N and O abundances in order to reproduce the observed absorption in nova spectra, which suggests significant local absorption. At the ionisation potential energies, one recognises the so–called *absorption–edges*, introducing additional structure to the soft X–ray spectra, see Figure 1.2: a black body spectrum of $T_{\text{eff}} = 500$ kK, $L = 10^{39}$ erg s^{-1} and $d = 10$ kpc is shown in red, which is absorbed by a hydrogen column of $n_H = 3 \cdot 10^{21}$ cm^{-2}. With galactic C, N and O abundances from Wilms et al. (2000), the absorbed black body spectrum is shown in green, with prominent absorption–edges of CI K at 0.284 keV, NI K at 0.410 keV and OI K at 0.543 keV. Although the H–edge at 13.6 eV is located rather far out of the soft X–ray range, the exponential tail of the hydrogen cross section still contributes significantly to the total absorption, see Figure 1.2.

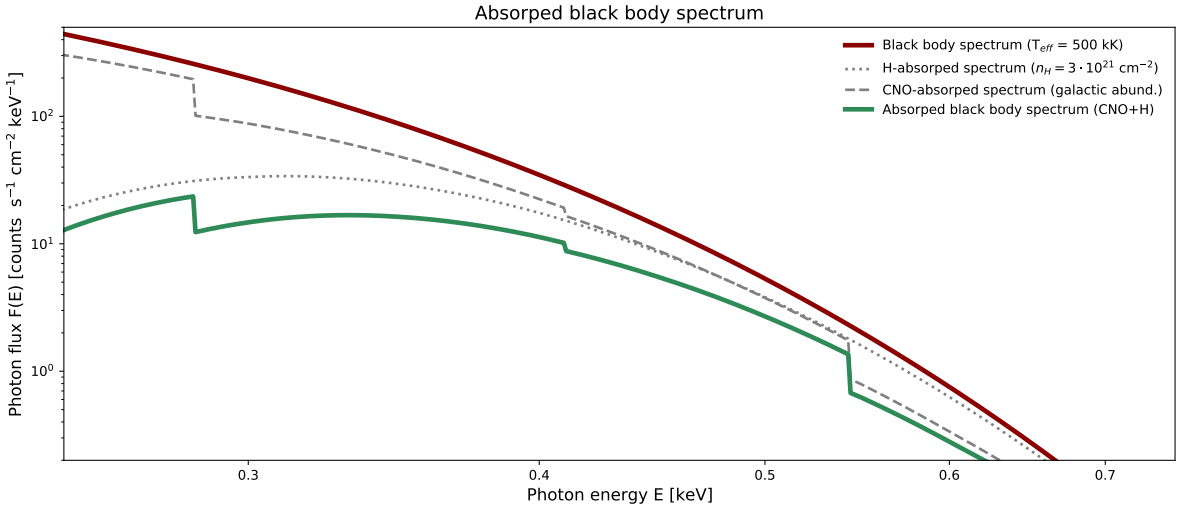

Figure 1.2: Absorbed black body spectrum for $T_{\text{eff}} = 500$ kK, $n_H = 3 \cdot 10^{21}$ cm^{-2} and galactic abundances for C, N and O from Wilms et al. (2000).

1.2.3 X–ray observations

Introduction

X–ray observations of novae during their SSS–phase provide crucial insights on the white dwarf basic properties (e.g. their mass, spin and composition), the physics of nuclear burning (e.g. the critical conditions for thermonuclear runaway), and the nature of the ejecta (e.g. their expansion velocities, mass and composition). As the Earth's atmosphere is opaque to high energy radiation beyond the near–ultraviolet range (with photons energies above $\sim$ 3.9 eV), X–ray observations cannot be obtained from ground–based observatories: most X–ray photons are absorbed by atmospheric oxygen and nitrogen, and consequently, developments in observational X–ray astronomy have always been closely connected to advancements in space technology. In the 1960s, balloons and sounding rockets opened the X–ray window to astronomy, with the first X–ray observations from space. Nowadays, several dedicated satellite missions are deployed to study the universe at high energy X–rays.

X–ray instrumentation

Space–borne X–ray telescopes focus the X–ray photons using barrel–shaped Wolter Type–I optics, built from nested cylindrical mirrors, which guide the X–rays by grazing incidence reflection. Conventional reflection telescopes would not work at these high energies, as X–ray photons would pass through the mirror, or be absorbed by the mirror material. When a single photon hits a pixel on the CCD detector in the focal plane, between 50 and 250 electron–hole pairs will be created in the semiconductor material, depending on the energy of the incoming photon. X–ray CCDs are read out at frequencies which are high compared to the rate of incoming photons. Consequently, the photon arrival time (i.e. the readout time bin), energy (i.e. the pulse height proportional to the number of electron–hole pairs) and incoming direction (i.e. the pixel on the CCD) are recorded for each pho-

ton individually. The output data of X–ray observations are so–called *event files*, which list all the individual photons as detected during the science exposure. X–ray spectra and light curves can be constructed from these event files by filtering on energy and time, respectively. For spatially resolved sources, X–ray images could be built from the incoming photon directions, although the angular resolution will be limited by deformations of the mirror surfaces, and the field of view will be narrow because of the grazing incidence conditions.

In consequence of how X–ray CCDs are designed, two photons that hit the same pixel within one time bin will be detected as one single photon with double the energy. This distortion of the photon spectrum is called *pile–up*, and causes a spurious second maximum at twice the energy of the original peak in the X–ray spectrum. The effect of pile–up is more significant for bright X–ray sources, with count rates that are high relative to the detector readout frequency. X–ray spectra of bright point sources are extracted from an annular region on the CCD, excluding the core of the point spread function which is most badly affected by pile–up, and the outer regions where the signal to noise ratio is too low. A good characterisation of the point spread function is now crucial to reconstruct the total photon flux from this limited extraction region.

While X–ray CCDs can measure the incoming photon energy and therefore can produce spectra, their energy resolution is rather limited. The introduction of X–ray gratings, as flown on the *XMM–Newton* and *Chandra* observatories, revolutionised the field of X–ray spectroscopy, as the dispersion of X–rays on a reflection grating, in conjunction with an imaging CCD detector, results in unprecedented spectral resolution. Future X–ray missions, such as *Athena* and *XRISM*, will be equipped with microcalorimeter detectors, which will directly measure the heat deposited by each single X–ray photon, based on the strong temperature dependence of the resistance in a superconducting transmission–edge sensor (TES). As most X–ray instruments cover a wide range of energies, the explicit energy–dependence of their effective areas will become important in reducing the observational X–ray data. Furthermore, this effective area is not a smooth function of energy, but shows additional structure caused by the interaction of X–rays with the mirror material, see the effective area for the *RGS1* instrument onboard *XMM–Newton* in Figure 1.3. Note how the edges between the nine distinct CCD chips are visible, and how the seventh chip, covering the 0.9 to 1.1 keV range, is inoperative. By multiplying the absorbed black body photon flux in Figure 1.2 with this *RGS1* effective area, one could estimate that a single X–ray photon is expected every 7.65 seconds at an energy bin centred on 0.4 keV (assuming energy bins of width 0.8 eV at 0.4 keV, where the *RGS1* resolving power is ~ 500). It is clear that in X–ray astronomy, one has to deal with low–number photon counting, and the associated Poissonian statistics. The *RGS1* instrument in itself will be discussed in the next paragraph, where we will briefly introduce the *Swift* and *XMM–Newton* X–ray missions.

X–ray missions

The *Neil Gehrels Swift Observatory* is a *NASA–UK* satellite mission, which was designed to study gamma–ray bursts (GRB), and launched in 2004. The mission carries a *Burst Alert Telescope* (*BAT*), which is a wide–field gamma–ray instrument to detect GRBs and trigger autonomous spacecraft

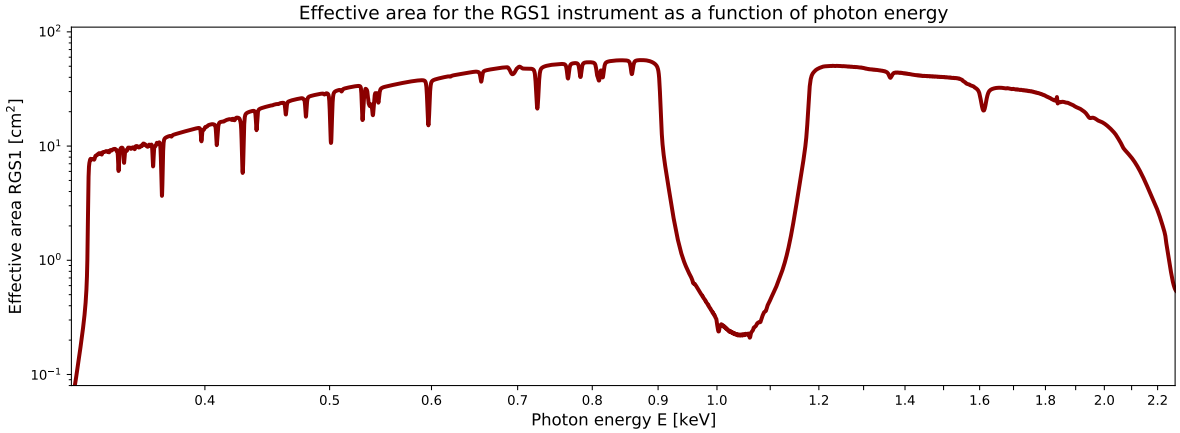

Figure 1.3: Effective area for the *XMM–Newton RGS1* instrument.

slews. Within a few seconds of the burst alert, the GRB afterglow can be observed by the *X–Ray Telescope* (*XRT*) and the *UV and Optical Telescope* (*UVOT*). The *XRT* CCD detector is a duplicate of the *XMM–Newton EPIC–MOS* instrument, on which X–ray photons are focused by twelve grazing incidence mirrors, nested in a Wolter Type I design. *XRT* covers the 0.3–10 keV soft X–ray range, and can operate in a conventional photon counting (PC) mode, or a 1D windowed timing (WT) mode with high 1.8 ms time resolution. While awaiting the next GRB, pointed observations of novae can be obtained as a filler program. However, as *Swift* is a low Earth orbit mission, no continuous observations can be obtained with exposure times more than 1.8 ks.

The *X–ray Multi Mirror* (*XMM–Newton*) mission is one of the cornerstone projects of the *ESA Horizon 2000* program. The X–ray observatory, which was launched in 1999, carries three high throughput X–ray telescopes with unprecedented sensitivity, built from 58 nested grazing incidence mirrors in a Wolter Type I design. X–ray CCDs are placed at the focus of each telescope, forming the *European Photon Imaging Camera* (*EPIC*): one *EPIC–PN* instrument (i.e. a pn CCD) and two *EPIC–MOS* instruments (based on metal–oxide–semiconductors). All three *EPIC* instruments are sensitive in the 0.1–10 keV range; *EPIC–PN* has an effective area between 200 and 1200 cm^2 and an energy resolution of $\sim$ 100 eV, while the *EPIC–MOS* detectors have an effective area between 50 and 500 cm^2 and an energy resolution of $\sim$ 50 eV. At two of the three X–ray telescopes, about half of the photons are dispersed by a reflection grating array and recorded by MOS–type CCDs, to form the *Reflection Grating Spectrometers* (*RGS*). The *RGS* instruments achieve resolving powers between 150 and 800 over the 0.33–2.5 keV range (i.e. an energy resolution between 0.5 and 2.0 eV in 0.3–0.7 keV range), with a total effective area (*RGS1+RGS2*) between 40 and 120 cm^2. Both *RGS* instruments have one inoperative CCD chip (see Figure 1.3), but luckily these gaps do not overlap in photon energy. Novae during their SSS–phase are extremely bright in the *RGS* energy range, and therefore ideal targets for spectroscopic studies with these instruments. With their superior resolving power, the *RGS* grating instruments could be used to identify individual line transitions at soft X–ray energies. The *EPIC* instruments will be used to obtain spectra above 2 keV (related to shocks and accretion), and for the extraction of light curves, as they are much more sensitive.

To study novae at SSS–energies, we will mainly focus on observational X–ray data from the *Swift* and *XMM–Newton* observatories. The *Chandra X–ray Observatory* is a *NASA* X–ray mission similar to *XMM–Newton*, but with a higher angular resolution, lower sensitivity and lower instrumental background. In chapter 5, we will work with observational data from the *Soft X–ray Telescope* (*SXT*) on board of the Indian multi–wavelength mission *AstroSat*. Although its energy and time resolution are rather poor, *SXT* covers a wide energy range and allows for long science exposures, providing a clear overview of the spectral evolution of novae. The future for X–ray astronomy is bright, with the planned succession of the *XMM–Newton* and *Chandra* flagship observatories by *Athena* and *Lynx*, respectively. The *XRISM* mission (2022) will be equipped with microcalorimeter detectors similar to those that were flown on the tragically lost *HITOMI* mission, which will provide spatially resolved spectroscopy with unprecedented spectral resolution. Microcalorimeter X–ray detectors will also be flown on the future European flagship observatory *Athena* (2031).

Chapter 2

Light Curve Modelling

2.1 Introduction

In each of the next three chapters, we will discuss one particular nova in great detail. We will provide the essential background for each nova system, analyse the observational data from various X–ray missions, and focus on the variability in the X–ray light curves. To this end, we have developed a flexible light curve simulation code named *DaRT*, which combines binary dynamics with advanced Monte Carlo radiative transfer (*DaRT*: Dynamics and Radiative Transfer). The *DaRT* code is used to study the recurrent nova U Sco in chapter 3, the classical nova V5116 Sgr in chapter 4, and finally the symbiotic nova V3890 Sgr in chapter 5. In this chapter, we will review the two–body problem and provide a short introduction to Monte Carlo radiative transfer. In section 2.4, we will describe the functionalities of the *DaRT* code.

2.2 Binary dynamics

2.2.1 The two–body problem

Consider a white dwarf star of mass M_1 (position vector $\vec{r_1}$), which forms a binary system with a companion star of mass M_2 (position vector $\vec{r_2}$). The binary motion for both stars follows from solving the gravitational two–body problem. In the centre of mass reference frame, we have:

$$\vec{r_1} = -\frac{M_2}{M}\vec{r} \tag{2.1}$$

$$\vec{r_2} = \frac{M_1}{M}\vec{r}, \tag{2.2}$$

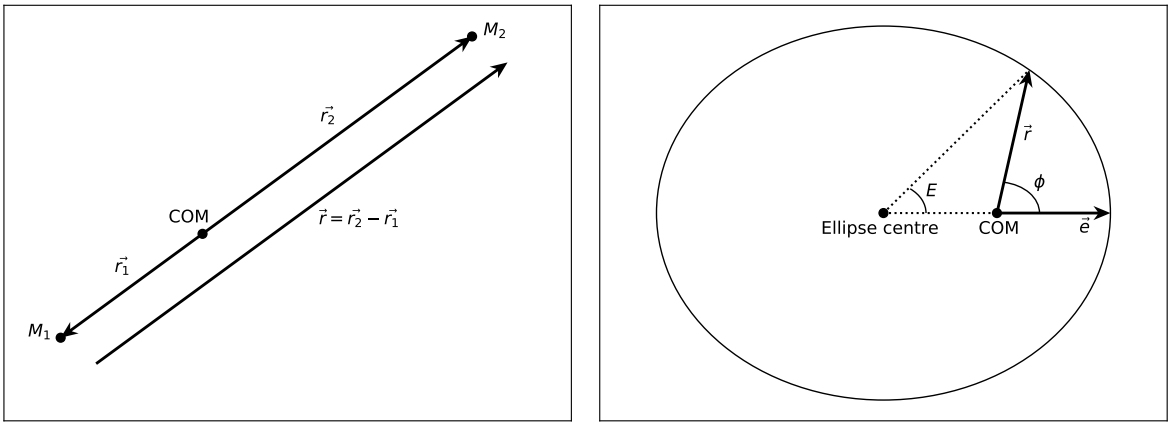

Figure 2.1: (a) Gravitational two–body problem in the centre of mass (COM) reference frame. (b) Definition of the true anomaly ϕ and the eccentric anomaly E.

with total mass $M = M_1 + M_2$ and $\vec{r} = \vec{r_2} - \vec{r_1}$ the relative position vector, as shown in Figure 2.1a. The equation of motion for $\vec{r}$ is given by the law of universal gravitation:

$$\begin{aligned}\ddot{\vec{r}} &= \ddot{\vec{r_2}} - \ddot{\vec{r_1}} \\ &= -\frac{GM_1M_2}{r^2M_2}\frac{\vec{r}}{r} - \frac{GM_1M_2}{r^2M_1}\frac{\vec{r}}{r} \\ &= -GM\frac{\vec{r}}{r^3}. \end{aligned} \tag{2.3}$$

The orbital angular momentum of the binary system is:

$$\begin{aligned}\vec{l} &= -\frac{M_2}{M}\vec{r} \times -\frac{M_1M_2}{M}\dot{\vec{r}} + \frac{M_1}{M}\vec{r} \times \frac{M_2M_1}{M}\dot{\vec{r}} \\ &= \vec{r} \times \mu\dot{\vec{r}},\end{aligned}$$

with $\mu = M_1M_2/M$ the reduced mass of the system. This angular momentum is conserved:

$$\begin{aligned}\dot{\vec{l}} &= \dot{\vec{r}} \times \mu\dot{\vec{r}} + \vec{r} \times \mu\ddot{\vec{r}} \\ &= \dot{\vec{r}} \times \mu\dot{\vec{r}} - \vec{r} \times \mu GM\frac{\vec{r}}{r^3} \\ &= \vec{0},\end{aligned}$$

which confines the two stellar bodies to a fixed orbital plane, as both $\vec{r}$ and $\dot{\vec{r}}$ are perpendicular to $\vec{l}$. The angular momentum has a magnitude l:

$$\begin{aligned}l &= \mu|\vec{r} \times (\dot{r}\,\vec{e_r} + r\dot{\phi}\,\vec{e_\phi})| \\ &= \mu r^2\dot{\phi},\end{aligned} \tag{2.4}$$

with $r\dot{\phi}\,\vec{e_\phi}$ the tangential vector component of $\dot{\vec{r}}$. The polar angle ϕ is called the true anomaly, see Figure 2.1b. The dimensionless Laplace–Runge–Lenz vector of the binary system is defined as:

$$\vec{e} = \frac{\dot{\vec{r}} \times \vec{l}}{\mu GM} - \frac{\vec{r}}{r}, \tag{2.5}$$

and is conserved during the binary motion:

$$\begin{aligned}\dot{\vec{e}} &= -\frac{\vec{r}}{r^3} \times (\vec{r} \times \dot{\vec{r}}) - \frac{\dot{\vec{r}}}{r} + \frac{\vec{r}}{r^2}\dot{r} \\ &= -\left(\frac{\vec{r}}{r^3} \cdot \dot{\vec{r}}\right)\vec{r} + \left(\frac{\vec{r}}{r^3} \cdot \vec{r}\right)\dot{\vec{r}} - \frac{\dot{\vec{r}}}{r} + \frac{\vec{r}}{r^2}\dot{r} \\ &= \vec{0},\end{aligned}$$

using Equation 2.3 for $\ddot{\vec{r}}$. With both $\dot{\vec{r}} \times \vec{l}$ and $\vec{r}$ in the orbital plane, $\vec{e}$ is a constant vector in the orbital plane which can serve as the reference direction for defining the true anomaly ϕ:

$$re\cos\phi = \vec{r} \cdot \vec{e}.$$

Plugging in the definition for the Laplace–Runge–Lenz vector (Equation 2.5), this can be solved for r as a function of the true anomaly:

$$\begin{aligned} re\cos\phi &= \frac{\vec{r} \cdot (\dot{\vec{r}} \times \vec{l})}{\mu GM} - \frac{\vec{r} \cdot \vec{r}}{r} \\ \iff re\cos\phi &= \frac{(\vec{r} \times \mu\dot{\vec{r}}) \cdot \vec{l}}{\mu^2 GM} - r \\ \iff r(\phi) &= \frac{l^2/\mu^2 GM}{1 + e\cos\phi}.\end{aligned}$$

We obtain the equation of an ellipse with an eccentricity $e = |\vec{e}| = \sqrt{1 - b^2/a^2}$, and one focus at the centre of mass. For an ellipse, one has:

$$\begin{aligned} r(\phi) &= \frac{a(1-e^2)}{1 + e\cos\phi} \\ \iff \frac{l^2}{\mu^2 GM} &= a(1-e^2),\end{aligned} \tag{2.6}$$

with a the semi–major axis and $b = a\sqrt{1-e^2}$ the semi–minor axis. The orbital separation $r(\phi)$ is minimal at $\phi = 0$, hence the Laplace–Runge–Lenz vector $\vec{e}$ points in the direction of the periapsis.

In order to obtain the binary positions as a function of time, one needs to transform to a new angle coordinate E, called the eccentric anomaly. This eccentric anomaly E is the polar angle for a position on the ellipse as measured from the ellipse centre, see Figure 2.1b. One has:

$$\begin{cases} r\cos\phi = a\cos E - ae \\ r\sin\phi = b\sin E, \end{cases} \tag{2.7}$$

with ae the distance between the centre of mass and the centre of the ellipse. This system can be solved for r as a function of E by summing the squared equations:

$$\begin{aligned} r^2 &= a^2\cos^2 E - 2a^2 e\cos E + a^2 e^2 + b^2\sin^2 E \\ &= a^2(\cos^2 E - 2e\cos E + e^2 + (1-e^2)(1-\cos^2 E)) \\ &= a^2(1 - e\cos E)^2,\end{aligned}$$

using $b = a\sqrt{1-e^2}$. We find r as a function of the eccentric anomaly E:

$$r(E) = a(1 - e\cos E), \tag{2.8}$$

with:

$$\dot{r} = ae\sin E\dot{E}. \tag{2.9}$$

Deriving the System 2.7 with respect to time, one obtains:

$$\begin{cases} -\sin\phi\ \dot{\phi} = -\dfrac{a\sin E\ \dot{E}}{r} - \dfrac{a\cos E - ae}{r^2}\ \dot{r} \\ \cos\phi\ \dot{\phi} = \dfrac{b\cos E\ \dot{E}}{r} - \dfrac{b\sin E}{r^2}\ \dot{r}. \end{cases}$$

Combined with Equation 2.8 and 2.9 for r and $\dot{r}$, respectively, this system is equivalent to:

$$\begin{cases} \sin\phi\ \dot{\phi} = \dfrac{a^2}{r^2}\sin E\ \dot{E}(1-e^2) \\ \cos\phi\ \dot{\phi} = \dfrac{ab}{r^2}\ \dot{E}(\cos E - e), \end{cases}$$

and can be solved for $\dot{\phi}$ as a function of $\dot{E}$ by summing the squared equations:

$$\begin{aligned} \dot{\phi}^2 &= \frac{a^4\dot{E}^2}{r^4}(1-e^2)\Big(\sin^2 E(1-e^2) + (\cos E - e)^2\Big) \\ &= \frac{b^2\dot{E}^2}{r^2}\frac{a^2(1 - 2e\cos E + e^2\cos^2 E)}{r^2} \\ &= \frac{b^2\dot{E}^2}{r^2}, \end{aligned}$$

again $r = a(1 - e\cos E)$, see Equation 2.8. We find:

$$\dot{\phi} = \frac{b\dot{E}}{r}, \tag{2.10}$$

Plugging Equation 2.8 and 2.10 in the formula for the angular momentum (Equation 2.4), one has:

$$\begin{aligned} l &= \mu ab(1 - e\cos E)\dot{E} \\ \Rightarrow l\int_{t_0}^{t} dt' &= \mu ab\int_0^E (1 - e\cos E')dE' \\ \Rightarrow l(t - t_0) &= \mu ab(E - e\sin E), \end{aligned}$$

with $E(t_0) = 0$ and l a constant. Combined with Equation 2.6 for the angular momentum, one finds:

$$E - e\sin E = \sqrt{\frac{GM}{a^3}}(t - t_0), \tag{2.11}$$

which provides a relation between the eccentric anomaly E and time. We can rewrite this equation using Kepler's laws. The surface area, covered by $\vec{r}$ per unit of time is:

$$\begin{aligned} \frac{dA}{dt} &= \frac{\dot{\phi}r^2}{2} \\ &= \frac{l}{2\mu}, \end{aligned}$$

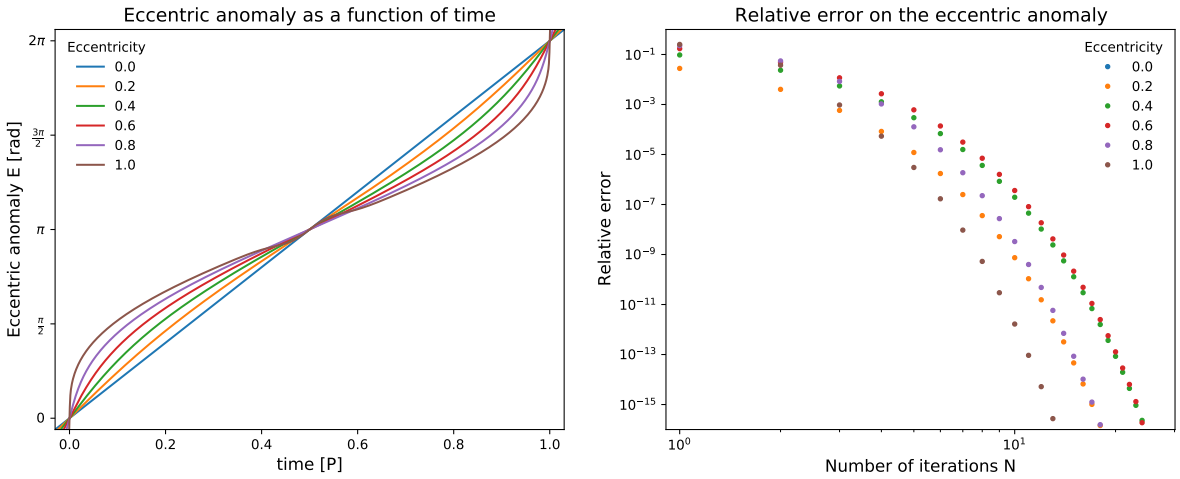

Figure 2.2: (a) Eccentric anomaly E as a function of time for various eccentricities and $N = 50$. (b) Relative error on the eccentric anomaly E as a function of the number of iterations N at $t = 0.1\ P$.

using Equation 2.4 for the angular momentum. This is the second law of Kepler, which is apparent from Figure 2.1b. Integrating this equation over one period P of time, one has:

$$\begin{aligned} \int_0^A dA' &= \int_0^P \frac{l}{2\mu} dt' \\ \iff ab\pi &= \frac{lP}{2\mu} \\ \iff P &= \frac{2\pi\mu a^2\sqrt{1-e^2}}{l}, \end{aligned}$$

with $ab\pi$ the surface area of an ellipse. Using Equation 2.6 for l, we find the third law of Kepler:

$$\boxed{P = \sqrt{\frac{4\pi^2}{GM}} a^{3/2}.} \tag{2.12}$$

Using this relation between a and P, we can rewrite Equation 2.11 as:

$$E - e\sin E = \frac{2\pi}{P}(t - t_0). \tag{2.13}$$

The right–hand side is defined as the mean anomaly $M(t)$, which increases at a constant rate in time:

$$M(t) = \frac{2\pi}{P}(t - t_0), \tag{2.14}$$

and so Equation 2.13 further reduces to the Kepler equation for the eccentric anomaly $E(t)$:

$$\boxed{E(t) - e\sin E(t) = M(t),} \tag{2.15}$$

with $E(t)$ as shown in Figure 2.2a. One obtains the relative position vector $\vec{r}(t)$ from Equation 2.7:

$$\begin{cases} x(t) = a\cos E(t) - ae \\ y(t) = b\sin E(t), \end{cases}$$

with $z(t) = 0$. From this $\vec{r}(t)$, the positions $\vec{r_1}(t)$ and $\vec{r_2}(t)$ are found using Equation 2.1 and 2.2:

$$\boxed{\begin{cases} \vec{r_1} = -\dfrac{M_2}{M}\big(a\cos E(t) - ae,\ b\sin E(t),\ 0\big) \\ \vec{r_2} = \dfrac{M_1}{M}\big(a\cos E(t) - ae,\ b\sin E(t),\ 0\big). \end{cases}} \tag{2.16}$$

However, the Kepler Equation 2.15 for the eccentric anomaly $E(t)$ is a transcendental equation, which cannot be solved analytically for E as a function of time. The eccentric anomaly can only be obtained numerically, with the most popular numerical method being an iteration of the form:

$$\begin{cases} E_0(t) = M(t) \\ E_{N+1}(t) = M(t) + e\sin E_N(t), \end{cases} \tag{2.17}$$

with the mean anomaly $M(t)$ given by Equation 2.14. Figure 2.2b shows the relative error on the calculated eccentric anomaly as a function of the number of iterations N. The values for E were obtained numerically at $t = 0.1\ P$, where the deviation from the mean anomaly is maximal (see Figure 2.2a). The relative error was calculated with respect to the $N = 50$ solution. The iterative results improve quickly with N, and for $N = 25$, the numerical float precision of 10^{-16} is reached for all eccentricities. Note how there is no error for $e = 0$, as here the $E(t) = M(t)$ solution is exact.

2.2.2 Close binary systems

We mention some important results for close binary systems, without a full mathematical derivation. In close binaries with orbital periods between 2 and 10 hours (see subsection 1.1.1), tidal forces lead to a circularisation of the binary orbit, i.e. $e \to 0$. The stellar motion in Equation 2.16 reduces to:

$$\begin{cases} \vec{r_1} = \dfrac{M_2 a}{M}\big(\cos(\omega t + \pi),\ \sin(\omega t + \pi),\ 0\big) \\ \vec{r_2} = \dfrac{M_1 a}{M}\big(\cos\omega t,\ b\sin\omega t,\ 0\big), \end{cases} \tag{2.18}$$

with ω the constant angular velocity:

$$\omega = \sqrt{\frac{GM}{a^3}} \tag{2.19}$$

$$= \frac{2\pi}{P}, \tag{2.20}$$

see Equation 2.12 and 2.14. While this means a significant simplification of the binary motion, the full elliptical implementation of Equation 2.15 and 2.16 will still be needed for the next chapters, when obscuration effects from clumpy ejecta moving on highly elliptical trajectories will be studied.

In close binaries which are evolving towards a nova outburst, mass is transferred from the nuclear–burning companion star to the white dwarf primary by Roche lobe overflow. The critical Roche surface is the dumbbell–shaped equipotential surface in the co–rotational frame, where the centrifugal force is just balanced by the gravitational attraction. It consists of two tear–shaped Roche lobes, both

containing one star, and separated by the inner Lagrangian point L_1. Only if matter resides inside a Roche lobe, it will be gravitationally bound to the corresponding stellar component. In interacting binaries, the evolved companion star fills its Roche lobe and consequently loses mass by Roche lobe overflow, which is then captured by the white dwarf. The Roche lobe radius R_{Roche} is defined as the radius for a sphere with the Roche lobe volume, and can be approximated to better than 1% over the entire mass range by the Eggleton (1983) Formula:

$$R_{\text{Roche}}(q,\ a) = \frac{0.49q^{2/3}}{0.6q^{2/3} + \ln\left(1 + q^{1/3}\right)} \cdot a, \tag{2.21}$$

with q the mass ratio, i.e. $q_2 = M_2/M_1$ for calculating the Roche radius of the companion star, and $q_1 = M_1/M_2$ for the Roche lobe of the white dwarf. In interacting binaries, the companion star fills its Roche lobe with $R_2 \approx R_{\text{Roche}}(q_2,\ a)$, while the compact white dwarf will only occupy a negligible fraction of its Roche lobe. However, from $R_{\text{Roche}}(q_1,\ a)$, one can estimate the size of the accretion disk around the white dwarf, see subsection 4.3.3.

One of the most important parameters linked to a nova eruption, is the total amount of mass ΔM_e that is ejected during the outburst. First, because the obscuring ejecta determine the spectral appearance of novae, with spectra shifting towards higher photon energies as the shell of ejecta clears while expanding (see subsection 1.1.2). Second, because the net mass balance is important to determine whether or not the white dwarf star is getting more massive over time, and grows towards the Chandrasekhar mass limit as a SNIa progenitor candidate. This is especially important for recurrent novae, which have multiple outbursts on human timescales (see chapter 3). Yet, the ejected mass is only poorly constrained by both theoretical models of the thermonuclear runaway, and observational data from erupting novae. In theory, the ejected mass ΔM_e could be obtained from precise measurements of the orbital period before and after the nova outburst (e.g. from optical photometry and spectroscopy during quiescence). For a circularised binary system, the orbital angular momentum is:

$$\begin{aligned} l &= \mu a^2 \omega \\ &= M_1 M_2 \sqrt[3]{\frac{G^2 P}{2\pi M}}, \end{aligned}$$

using Equation 2.12 and 2.20 for a and ω as a function of P. Taking the logarithmic derivative yields:

$$\frac{dl}{l} = \frac{dM_1}{M_1} + \frac{dP}{3P} - \frac{dM_1}{3M}, \tag{2.22}$$

with M_2 a constant and $dM = dM_1$. When some mass $|dM_1|$ is ejected isotropically from the white dwarf star, the binary system loses angular momentum as:

$$\begin{aligned} dl &= dM_1 r_1^2 \omega \\ &= dM_1 \frac{M_2^2 a^2}{M^2} \omega \\ \Rightarrow \frac{dl}{l} &= \frac{dM_1 M_2}{M M_1}. \end{aligned} \tag{2.23}$$

Combining Equation 2.22 with Equation 2.23, one has:

$$\begin{aligned}
&\iff \frac{dM_1}{M_1} + \frac{dP}{3P} - \frac{dM_1}{3(M_1+M_2)} = \frac{dM_1 M_2}{(M_1+M_2)M_1} \\
&\iff \frac{dM_1}{M_1} + \frac{dP}{3P} - \frac{dM_1}{3(M_1+M_2)} = \frac{dM_1}{M_1} - \frac{dM_1}{M_1+M_2} \\
&\iff \frac{dM_1}{M_1+M_2} = -\frac{dP}{2P}.
\end{aligned}$$

As the primary mass decreases from $M_{1,i}$ to $M_{1,f}$, the orbital period increases from P_i to P_f, and the above differential equation is easily integrated as:

$$\begin{aligned}
&\int_{M_{1,i}}^{M_{1,f}} \frac{dM_1}{M_1+M_2} = -\frac{1}{2}\int_{P_i}^{P_f} \frac{dP}{P} \\
\iff &\ln\left(M_{1,f}+M_2\right) - \ln\left(M_{1,i}+M_2\right) = -\frac{1}{2}\left(\ln P_f - \ln P_i\right) \\
&\iff \frac{M_{1,f}+M_2}{M_{1,i}+M_2} = \sqrt{\frac{P_i}{P_f}}.
\end{aligned}$$

As a result, one can determine the total amount of ejected mass $\Delta M_e = M_{1,i} - M_{1,f}$ from the observed change in the orbital period as:

$$\boxed{\Delta M_e = \left(1 - \sqrt{\frac{P_i}{P_f}}\right)\left(M_{1,i}+M_2\right).} \tag{2.24}$$

2.3 Monte Carlo radiative transfer

2.3.1 Radiative transfer

What we know about the astrophysical universe, derives exclusively from the electromagnetic radiation that we observe on Earth. However, while travelling from source to observer, this light was altered by scattering, absorption and re–emission, both locally and inside the interstellar medium. Radiative transfer modelling describes this alteration of light by the travel medium, and is important for understanding how the intrinsic emission of astrophysical sources translates to observations.

Mathematically, the radiation field at a position $\vec{r}$ in a direction $\vec{k}$ is described by the specific intensity $I_E(\vec{r},\ \vec{k})$. Consider an infinitesimal surface at $\vec{r}$, with a surface area dA and a unit normal $\vec{n}$. When $d\mathcal{E}$ is the total radiant energy of photons with $h\nu$ in the $(E,\ E+dE)$–range, crossing this surface during a time interval dt within a solid angle $d\Omega$ around $\vec{k}$, then the specific intensity $I_E(\vec{r},\ \vec{k})$ is defined as:

$$I_E(\vec{r},\ \vec{k}) = \frac{d\mathcal{E}}{(\vec{k}\cdot\vec{n})dA\ dE\ dt\ d\Omega},$$

with $\vec{k}$ a unit vector. We consider the specific intensity as being time–independent, i.e. the transfer medium changes on timescales which are significantly larger than the photon travel times, and for each

point in time the radiation field is obtained in the time–frozen configuration. The spatial evolution of the specific intensity is described by the radiative transfer equation:

$$\frac{dI_E}{ds}(\vec{r},\ \vec{k}) = j_E(\vec{r},\ \vec{k}) - \kappa_E(\vec{r})\rho(\vec{r})I_E(\vec{r},\ \vec{k}), \tag{2.25}$$

with s the path length along the beam in the $\vec{k}$–direction. The sink term on the right–hand side is proportional to the intensity of the radiation field I_E and the total amount of material ρ. The proportionality constant κ_E is a material property of the transfer medium, which might depend on the photon energy E, and is called the opacity. This term accounts for two physical processes removing energy from the radiation field, absorption and scattering:

$$\kappa_E = \kappa_E^{abs} + \kappa_E^{sca}. \tag{2.26}$$

The source term j_E in Equation 2.25 describes how energy is added to the radiation field. Not considering (re–)emission by the transfer medium, this term accounts for the primary source of SSS-emission and the effect of scattering (which is elastic, see section 3.3). Away from the central primary source, j_E just describes how scattering redirects photon energy into a new direction:

$$j_E(\vec{r},\ \vec{k}) = \int d\Omega' \Big(\kappa_E^{sca}(\vec{r})\rho(\vec{r})I_E(\vec{r},\ \vec{k'})\Big)\Phi_E(\vec{r},\ \vec{k},\ \vec{k'}). \tag{2.27}$$

The factor $\int d\Omega' \big(\kappa_E^{sca}\rho I_E(\vec{k'})\big)$ corresponds to the total energy which is removed from the radiation field by scattering at $\vec{r}$, integrated over all incoming $\vec{k'}$–directions. This photon energy is shuffled into a new direction as described by the scattering phase function $\Phi_E(\vec{k},\ \vec{k'})$, which is defined as the probability distribution for scattering out of the $\vec{k'}$–beam into $d\Omega$ around $\vec{k}$. This Φ_E is just $(4\pi)^{-1}$ for isotropic scattering, but can also describe a wide variety of anisotropic scattering modes. We assume that the distribution of matter $\rho(\vec{r})$, and the optical properties $\kappa_E(\vec{r})$ and $\Phi_E(\vec{r})$, are provided with the configuration setup. Now consider the original fraction of a beam in the $\vec{k}$–direction, which survives before getting lost to absorption or scattering (i.e. Equation 2.25, only considering the sink term):

$$\frac{dI_E}{ds}(s) = -\kappa_E(s)\rho(s)I_E(s), \tag{2.28}$$

with all properties evaluated at a path length s along the beam. We transform to a new position coordinate along the path, the dimensionless optical depth $\tau_E(s)$, which is defined as:

$$\begin{aligned} \tau_E(s) &= \int_0^s ds' \kappa_E(s')\rho(s') \\ \Rightarrow d\tau_E &= \kappa_E(s)\rho(s)ds, \end{aligned} \tag{2.29}$$

using the fundamental theorem of calculus. We do not introduce a new notation for quantities as evaluated in optical depth space, i.e. $I_E(\tau_E) \equiv I_E(s(\tau_E))$. Now, Equation 2.28 can be solved for τ_E:

$$\begin{aligned} dI_E &= -d\tau_E\ I_E \\ \iff \int_{I_{E0}}^{I_E} \frac{dI'_E}{I'_E} &= -\int_0^{\tau_E} d\tau'_E \\ \iff I_E(\tau_E) &= I_E(0)\ e^{-\tau_E}. \end{aligned} \tag{2.30}$$

In optical depth space, $1-e^{-\tau_E}$ is the total fraction of energy from the original $\vec{k}$–beam which got lost to absorption or scattering by the transfer medium, after propagating a distance τ_E. However, the full radiative transfer equation cannot be solved analytically in arbitrary 3D–geometries, as the scattering term in Equation 2.27 couples all beam directions $\vec{k}$, at each position $\vec{r}$. Furthermore, Thomson scattering on a plasma of relativistic electrons will couple all photon energies E, see section 3.3.

2.3.2 Monte Carlo radiative transfer

The Monte Carlo technique is the most popular numerical method to address the nonlinear and non-local radiative transfer problem in general 3D–geometries. Photon propagation is simulated directly, with relevant propagation physics being emulated by drawing random events from the appropriate probability distributions. The basic idea of Monte Carlo radiative transfer (MCRT) is to discretise the radiation field in energy quanta, called photon packages, which are launched sequentially from the primary sources, and tracked individually as they propagate through the transfer medium.

Consider N_0 photon packages being launched into a single direction $\vec{k}$. Equation 2.30 tells that on average, $(1-e^{-\tau_E})\cdot N_0$ photons will have interacted with the transfer medium after travelling a distance τ_E, i.e. either by absorption or scattering. This can be interpreted statistically as having a cumulative distribution $F(\tau_E)$ for the optical depth covered before an interaction:

$$F(\tau_E) = 1 - e^{-\tau_E} \tag{2.31}$$

$$\iff f(\tau_E) = e^{-\tau_E}, \tag{2.32}$$

with $f(\tau_E)$ the normalised probability density function for the distance τ_E towards the next interaction point for an individual photon package. From this exponential distribution, one can generate a random τ_E between 0 and $+\infty$, using the univariate transformation method for probabilities:

$$U_1 = F(\tau_E)$$

$$\iff \tau_E = -\ln(1-U_1), \tag{2.33}$$

with U_1 a uniform deviate between 0 and 1, and $F(\tau_E)$ the cumulative distribution in Equation 2.31.

For each of the N_{pp} photon packages in a MCRT simulation, the photon life cycle proceeds as follows: The photon package is launched into the computational domain, at a position $\vec{r}$ and in a direction $\vec{k}$ as specified by the primary source definition. First, a random interaction point τ_E is generated using Equation 2.33. If this τ_E is larger than the total optical depth of the transfer medium, the photon package passes through without interacting, and could be observed in the $\vec{k}$–direction. When there is an interaction, the physical path length s towards the interaction point can be obtained from τ_E by inverting Equation 2.29 numerically, as both $\kappa_E(s)$ and $\rho(s)$ are known. At the interaction point $\vec{r_I}$, the photon package will scatter when $U_2 \leq \omega_E(\vec{r_I})$, and will be absorbed when $U_2 > \omega_E(\vec{r_I})$, with U_2 a uniform deviate between 0 and 1, and ω_E the scattering albedo defined as:

$$\omega_E = \frac{\kappa_E^{sca}}{\kappa_E^{abs} + \kappa_E^{sca}}, \tag{2.34}$$

with κ_E^{abs} and κ_E^{sca} the absorption and scattering opacity, respectively (see Equation 2.26). If the photon package is absorbed, its life cycle is terminated and the next package can be launched from the primary sources. If the photon package is scattered, then a new propagation direction is generated from the scattering phase function $\Phi_E(\vec{r_I})$, which is provided as a material property of the transfer medium. A next interaction point is drawn using Equation 2.33, and the photon life cycle continues until this photon package is either absorbed or leaves the transfer medium, where it can be detected. By statistically analysing the photon paths at the end of the Monte Carlo radiative transfer simulation, one can reconstruct the radiation field. However, because of the random nature of this technique, the simulation results will inevitably contain a certain amount of Poisson noise.

2.3.3 The *SKIRT* code

SKIRT is a state-of-the-art Monte Carlo radiative transfer code, developed and maintained at the Astronomical Observatory in Ghent (Baes et al., 2003, 2011; Camps & Baes, 2015, 2020). The simulation code focuses on radiative transfer in dusty astrophysical systems, and implements a Monte Carlo photon life cycle emulating scattering, absorption and re-emission by dust. MCRT simulations in full 3D–geometries are facilitated by the introduction of various acceleration mechanisms, which are mostly based on importance sampling, and are implemented in the so–called weighted photon life cycle. Moreover, *SKIRT* was designed into a hybrid parallelisation scheme, which combines multi-threading and multi-processing, and allows users to run simulations efficiently both on laptops and at high-performance computing facilities (Verstocken et al., 2017).

Acceleration mechanisms

The most important optimisation technique in *SKIRT*, compared to the simple MCRT as described in the previous subsection, is the photons package *peel–off* towards the detector at each emission and scattering event. The observed peel–off photon packages are corrected with a bias factor W:

$$W = P(\vec{k_o})\, e^{-\tau_o},$$

accounting for the probability of being directed towards the observer $P(\vec{k_o})$, and for the fraction of energy lost to the medium (see Equation 2.31). Peel–off causes all photon packages to contribute to the science output, instead of inefficiently studying a system by only using photons that leave the transfer medium in one particular $\vec{k_o}$–direction. Each time a photon package is launched, there is an *emission peel–off* to the instrument, weighted by a directional bias in the case of anisotropic sources. A next interaction point is generated from a biased τ–distribution, to cover the total range of optical depths more uniformly. *Continuous absorption* corrects the photon energy for absorption by the medium between two interactions, while *forced scattering* ensures that each photon will scatter at least once. For each scattering interaction, there is a *scattering peel–off* to the instrument, corrected for the anisotropy of the scattering phase function at that position (Steinacker et al., 2013). Along with these biasing techniques, *composite biasing* was introduced to prevent large bias factors, which might cause a significant amount of noise in the simulation results (Baes et al., 2016).

SKIRT input

SKIRT simulations are built up from a *.ski* input file, containing all the simulation parameters (e.g. the total number of photon packages N_{pp}) and the configuration setup, i.e. the definition for the transfer media and primary sources. The *SKIRT* code provides a suite of built–in geometries $\rho_C(\vec{r})$ which can be moved, scaled and combined in an arbitrary fashion. Given the geometry $\rho_C(\vec{r})$ for each component (normalised to $M_C = 1$), the density of the transfer medium is fully defined by providing the component masses M_C. The final geometry is then efficiently introduced on a numerical grid using the hierarchical octree and k–d tree algorithms, which are available to partition the computational domain according to some maximum density criterion (Saftly et al., 2013, 2014).

Optical properties

The optical properties for the transfer media in a light curve simulation are characterised by three parameters, which do not depend on the photon energy. Each component C has a constant opacity κ_C, which provides the transformation between optical depth τ and path length s, see Equation 2.29 with $\rho(s) = M_C\rho_C(s)$. The scattering albedo ω_C is a dimensionless constant, which sets the probability for scattering at the component, relative to absorption (see Equation 2.34). Finally, the scattering anisotropy is characterised by a dimensionless asymmetry parameter g_C between -1 and 1. Isotropic scattering is obtained for $g_C = 0$, while $g_C \neq 0$ is linked to anisotropic scattering with a scattering phase function Φ_{g_C} modelled by the one–parameter family of Henyey–Greenstein phase functions (Henyey & Greenstein, 1941). As the optical properties for the transfer media do not depend on the photon energy E, the energy range and spectral profile of the primary sources are rather meaningless, and can be represented by one central energy bin. The primary sources will be reconsidered in section 3.3, when Thomson scattering on a plasma of relativistic electrons will be studied.

SKIRT output

Eventually, photon detectors are set up to record the photon packages leaving the transfer medium. The `SEDInstrument` and `FrameInstrument` are designed to mimic spectrometers and imaging–CCDs, respectively, and provide multi–wavelength images and global spectral energy distributions (SED). However, these smart detectors can do more than just counting the total number of photons for each energy or direction bin, as they are able to obtain in–simulation information such as the scattering level and origin of each observed photon, which normally is not accessible to the observer. A variety of unit systems are available for the simulation output, although none of these units is really suited for the X–ray range, as *SKIRT* was designed to operate from IR to UV energies. *SKIRT* simulations will be run in SI–units, and the post–processing in *DaRT* will include a unit conversion from SI–flux to a photon flux F in counts s^{-1} cm^{-2} keV^{-1}.

2.4 The *DaRT* code

DaRT is a simulation code for obtaining light curves from highly dynamical astrophysical systems. It introduces a time grid to the MCRT code *SKIRT*, and is written in `Python`. For each time in the time grid, all positions and orientations in the dynamical system are updated, and Monte Carlo radiative transfer is performed in the time–frozen configuration. For the radiative transfer simulations, *DaRT* calls the *SKIRT* code version 9 (Camps & Baes, 2020). Yet, the *DaRT* time–interface was designed to be fully compatible with any future version of *SKIRT*, especially with full X–ray support in prospect.

2.4.1 Implementation

DaRT input

A *DaRT* simulation is set up from an input text file, which contains the simulation parameters listed in human–readable form (*"parameter = value"*). First, the simulation time grid is specified by a start time, stop time and the appropriate time step. Alternatively, a custom time grid can be imported from an *ASCII* file, which is especially useful for simulating light curves on the same time grid as the available observational data. The *DaRT* total runtime is dominated by the MCRT–calls, and thus scales linearly with the total number of time steps N_t. The next few parameters in the input file configure the radiative transfer simulations, with e.g. the total number of photon packages N_{pp} and the path to an empty *.ski SKIRT* template (i.e. without sources or transfer media).

Components

Central to the *DaRT* code is the `Configuration` class, which keeps track of all components in the simulation, i.e. both obscuring bodies and sources. The configuration is initialised by reading the component parameters from the input text file, where an arbitrary number of components can be declared. The `Component` class is a container for the component parameters (e.g. luminosity, radius, mass or position), which are stored as instances of the `Quantity` class. Each quantity can either have a fixed value (*"parameter = value"*), can vary as a function of time (*"parameter = function f"*) or can be read from an *ASCII* file (*"parameter = read path"*). The time–dependent quantities are updated throughout the simulation, while most will be fixed. Positions are updated using Equation 2.16 and 2.17, with the stellar masses, semi–major axis and eccentricity provided as component parameters. It should be noted that the iteration in Equation 2.17 reaches numerical float precision for $N \approx 25$ (see Figure 2.2), and has a negligible computational cost compared to e.g. launching $N_{pp} = 10^7$ photon packages for each point in the time grid.

Geometries

For declaring the component geometries (i.e. their spatial distribution of matter $\rho_C(\vec{r})$), one can use the built–in *SKIRT* geometries by referencing the appropriate geometry class name in the *DaRT* input file (e.g. *"geometry =* `SersicGeometry`*"*). Additionally, the *SKIRT* functionality was expanded

with the option to load arbitrary geometries into the transfer medium, imported from a 3D–data cube. The *DaRT* code provides the *.fits* data cube and a pixel scale (i.e. the physical size of one pixel), which allows *SKIRT* to sample this geometry as part of the transfer medium. Throughout the simulation, *DaRT* controls both the position and orientation of the cube component. This will be important in chapter 4, where an asymmetric accretion disk will be introduced as a data cube geometry, with an accretion bulge that should always face the Roche–lobe–overflowing companion star.

Grids

At each point in time, the total distribution of matter inside the transfer medium is introduced on a numerical grid using one of the hierarchical gridding algorithms available in *SKIRT*. Partitioning the configuration top–down using an octree gridding technique has proven to be the most reliable and efficient approach in this context of few–body systems: The transfer medium is mostly empty, but contains a few obscuring bodies where high grid resolution is desired. The octree algorithm is based on a maximal mass criterion, which should depend on the overall scale of the astrophysical system. Further, a minimal and maximal octree subdivision level are specified, which are chosen as a correct balance between resolution and computational runtime. The grid extends are re–calculated for each point in time, from the positions and radii of all components. For non–spherical components, their radius should be interpreted as a measure for the bounding box enclosing the component.

Detectors

Even within our galaxy, the two stellar components of cataclysmic variables cannot be resolved individually with any observational instrument, nor can smaller, obscuring bodies inside these binaries. Nova systems are observed as point sources, and in a best–case scenario, one could obtain SEDs as a function of time. However, in modelling these observational data one could generate artificial resolved images, offering a unique view on the close binary system. The *DaRT* input file provides information on the `FrameInstrument` and `SEDInstrument` detectors recording the MCRT simulation output at each configuration, i.e. the inclination, field of view and distance towards the system. For the imaging instruments, one can choose to centre their field of view on one specific component throughout the simulation. This feature is used frequently to follow the white dwarf source of SSS–emission while studying the SSS–variability. For the spectral instruments, one can set the number of individual photon scattering levels that should be recorded.

DaRT output

As the configuration evolves in time, the input file for the *SKIRT* simulation is kept up to date by the `SKIRT_input` class. At the start of a *DaRT* simulation, all relevant sources, transfer media and instruments are loaded into the *.ski* template, and for each time step, the time–dependent parameters (e.g. positions, grid extends and instrument pointings) are updated. Once the appropriate information is added to the *.ski* input file, the MCRT simulation is run automatically using the *Python Toolkit for*

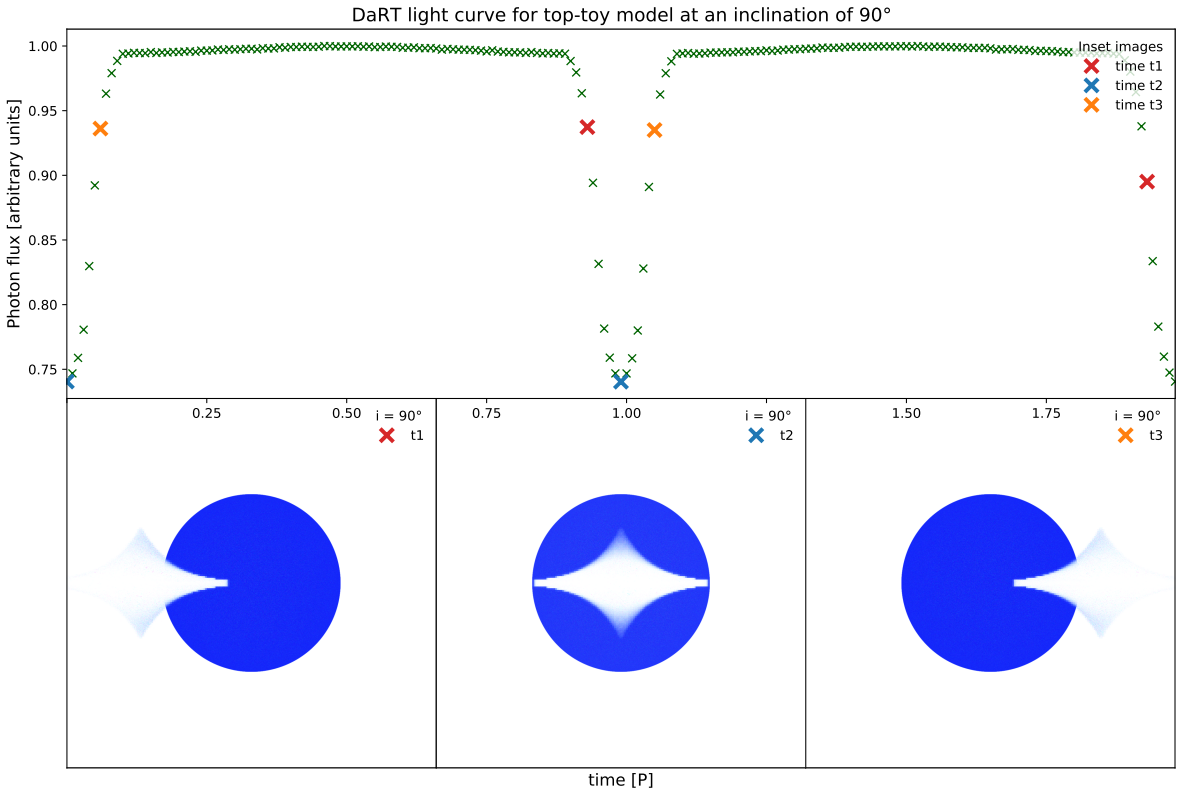

Figure 2.3: An example *DaRT* simulation for a top–toy in orbit around a stellar surface ($i = 90°$).

SKIRT (*PTS*). The *SKIRT* simulation output is collected and reduced by the `Datacentre` class, which also stores a dynamics log file. False–colour *.png* images are created from the *.fits* multi–wavelength imaging data, and the SEDs in W m^{-3} are converted to counts s^{-1} cm^{-2} keV^{-1}, and then integrated to counts s^{-1} using the energy–dependent effective areas for the *XMM–Newton* instruments *EPIC–PN*, *EPIC–MOS* or *RGS*. Finally, the reduced data is stored to an output folder with the simulation's name, and a first look on the calculated light curve is shown.

2.4.2 Example *DaRT* simulation

A geometric example simulation was performed to illustrate the *DaRT* functionalities, with results as shown in Figure 2.3 and Figure 2.4. The underlying model contains a top–toy–shaped obscuring body, in orbit around a `StellarSurface` source at a distance of 10^{-3} AU. The stellar source has a flat emission spectrum between 0.2 and 0.7 keV, and is much more massive than the obscuring body. The top–toy was introduced to *DaRT* as a data cube geometry, built from 57080 cubic blocks with a corresponding pixel scale of $6 \cdot 10^{-6}$ AU. The component mass was set to 10^{-5} $M_\odot$, with spatial dimensions $(4 \times 6) \cdot 10^{-4}$ AU comparable to the stellar surface, resulting in a uniform density component of $\rho \approx 500$ kg m^{-3}. The optical properties of the obscuring top–toy are: a scattering albedo of $\omega = 0.85$ (most photons will scatter), an asymmetry parameter of $g = 0$ (isotropic scattering) and an arbitrary high extinction opacity κ (the component is fully opaque). *DaRT* was run to simulate two full periods, with $P = 0.01$ day (for $M = 1.35$ $M_\odot$, see Equation 2.12) and $N_{pp} = 5 \cdot 10^7$.

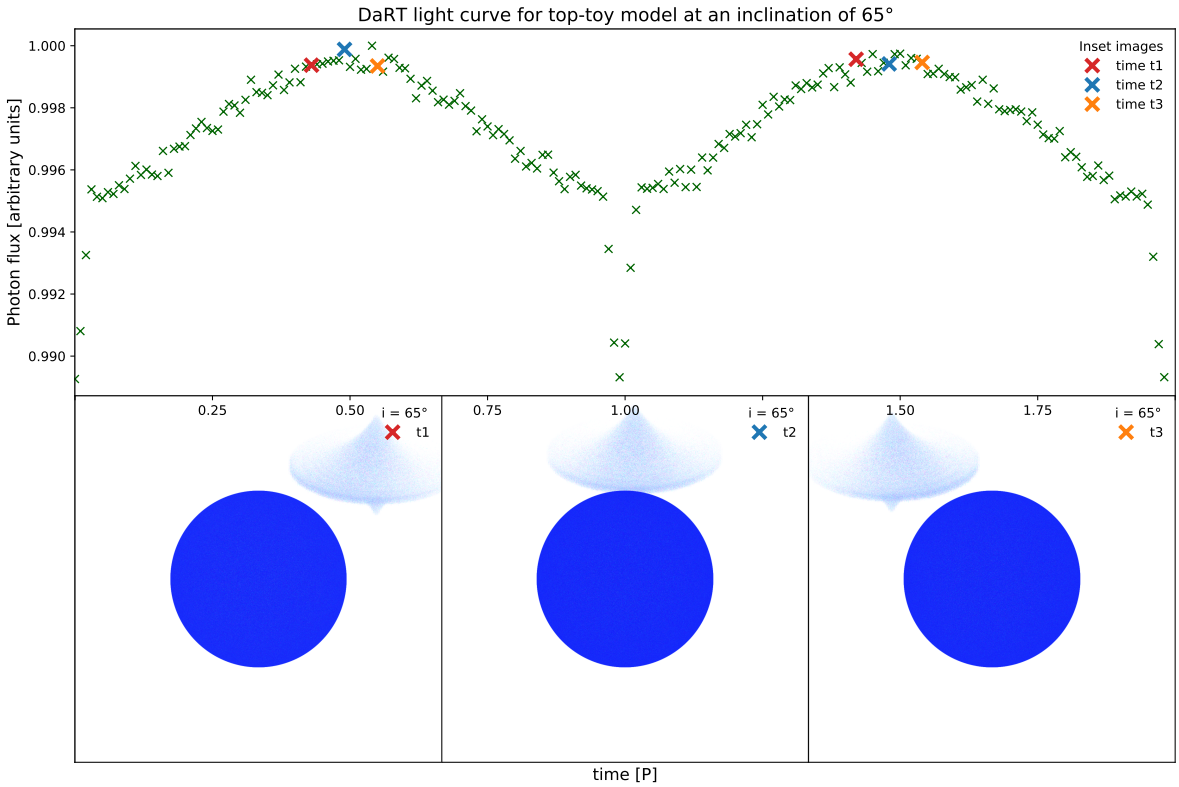

Figure 2.4: An example *DaRT* simulation for a top–toy in orbit around a stellar surface ($i = 65°$)

In Figure 2.3, the *DaRT* simulation results are shown for the edge–on system ($i = 90°$). The top panel contains the total light curve, covering two orbital periods in 200 data points. Centred on $t = P$, the top–toy is observed to transit the stellar source. Imaging data of this transit is shown in the bottom panel, at times as indicated on the light curve. For optimal contrast, the false colours were inverted, i.e. the stellar emission is shown in blue, and the empty, black background in white. The obscuring body is fully opaque, and covers one quarter of the stellar surface at $t = P$, while the light curve drops by 25%. In Figure 2.4, the same system is observed at an inclination of $i = 65°$. The light curve in the top panel reaches a maximum when the top–toy is behind the stellar source at $t = 0.5P$. For $i = 65°$, the top–toy is visible at all times during the orbit, and at $t = 0.5P$ the irradiated side will face the detector, as shown in the imaging data below. Thus, the observed 0.5% modulation in the light curve is caused by a variable fraction of scattered light. At $t = P$, the tip of the top–toy is observed in front of the stellar source, causing an additional obscuration effect in the light curve.

To summarise, we have designed a light curve simulation code, which combines binary dynamics with advanced Monte Carlo radiative transfer (*DaRT*: Dynamics and Radiative Transfer). The *DaRT* code offers the flexibility to incorporate arbitrary 3D–geometries, adjustable reflection properties, advanced transfer media and the capability of dealing with time–dependent system parameters (this includes importing tabulated positions, e.g. N–body simulation output). We have implemented the possibility to run *Dart* as a `Python` function, optionally with parameter arguments, which is useful for setting up a fitting routine. The *DaRT* code will be used thoroughly in the next three chapters.

Chapter 3

U Sco 2010

3.1 Introduction

U Sco is a recurrent nova (RN) system in the constellation of Scorpius, with ten recorded outburst since 1863. It is one of the ten galactic novae identified as being recurrent, and with 7.88 years between its 1979 and 1987 outburst, U Sco has the shortest inter–eruption time of all galactic novae (Schaefer, 2010a). (Faster RNe have been discovered in M31, e.g. M31N 2008–12a with a duty cycle of ~ 1 year (Darnley et al., 2015).) Next to its short recurrence timescale, U Sco is observed to have the fastest outburst evolution of all novae, rising to optical maximum in less than six hours, then fading by three magnitudes in about three days (Schaefer, 2010b). As half of the ten U Sco outbursts have only been discovered retrospectively from archival photographic plates, and given that U Sco evolves exceptionally fast, it is likely that more outburst went unnoticed. The five most recent eruptions in 1969, 1979, 1987, 1999 and 2010 suggest a recurrence timescale of about 10 years, and a next outburst was predicted for 2020.7 ± 0.6 (Schaefer, 2019). However, there has been argued for a scenario where a 2017 outburst went unnoticed when U Sco could not be observed by solar constraints, as of this writing no outburst has been detected.

While all novae are predicted to recur, classical novae will only experience a next outburst on timescales of 10^4–10^5 yr (Ness et al., 2012), in contrast to the group of recurrent novae with recurrence times less than a hundred years. These short inter–eruption times strongly constrain the RNe system parameters, in order to allow for a thermonuclear runaway on human rather than astronomical timescales. First, the accretion rate should be high, to accumulate sufficient hydrogen on the white dwarf surface in a short period of time. RNe have an above–average accretion rate for cataclysmic variables, up to 10^{-7} $M_\odot$ yr^{-1} (Hachisu & Kato, 2000b,a) and two orders of magnitude higher than accretion in classical novae (Livio, 1994). Secondly, the white dwarf star should be massive, with a mass $M_{WD} > 1.3$ $M_\odot$, close to the Chandrasekhar mass limit (Truran & Livio, 1986; Hachisu & Kato, 2001). In this way, the high surface gravity allows the critical temperature and density conditions for thermonuclear runaway to be reached more easily (Schaefer, 2010a). Additionally, higher intrinsic white dwarf luminosities cause the surface temperature to increase, which facilitates the nova

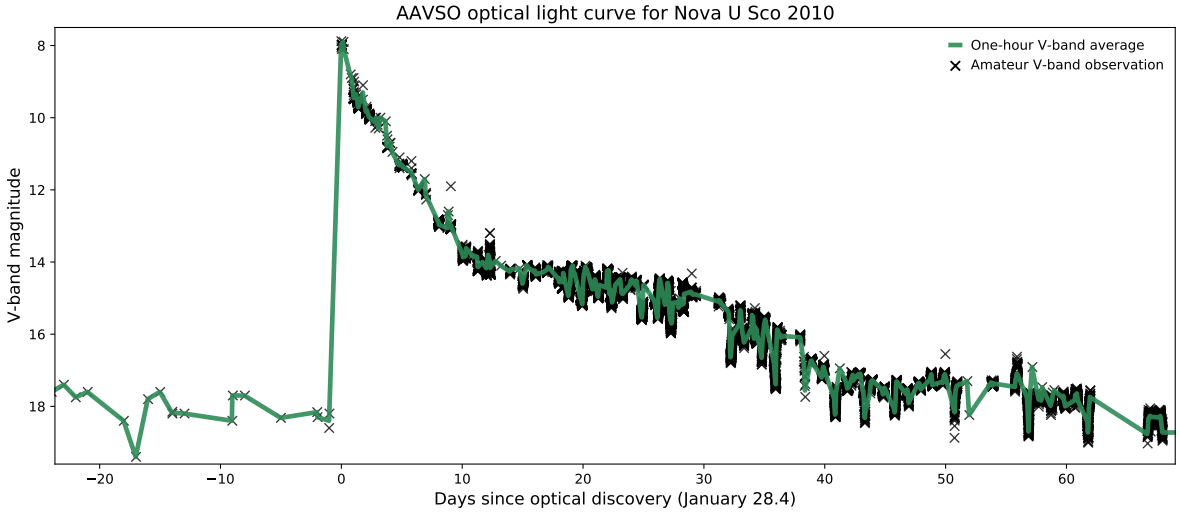

Figure 3.1: Optical monitoring of U Sco throughout the 2010 eruption, with over 12500 magnitude measurement from the AAVSO–database within the first 70 days after outburst.

ignition process (Webbink et al., 1987). With high accretion rates and white dwarf masses closes to the Chandrasekhar mass limit, RNe are a strong supernova Ia progenitor candidate, provided that the white dwarf has a CO–composition (Nomoto et al., 1984). However, with large uncertainties on the amount of ejected mass at each outburst, there is a lot of debate about whether or not the white dwarf mass increases over each eruption cycle (Starrfield et al., 1988, 1985; Livio & Truran, 1992).

U Sco is a double–line eclipsing close binary at high inclination (Schaefer & Ringwald, 1995), which allows for a detailed determination of the system parameters. It has been identified as a semi–detached system with a white dwarf primary of mass $M_{WD} > 1.31\ M_\odot$, and an evolved nuclear–burning secondary of mass $M_2 = 0.88 \pm 0.17\ M_\odot$ (Thoroughgood et al., 2001; Hachisu & Kato, 2000a). The white dwarf mass should not exceed the Chandrasekhar mass limit, but these measurements indicate that M_{WD} may be close to the limit, as required for such fast recurrent nova. The secondary star is a sub–giant of spectral class F IV–V, with a radius $R_2 = 2.1 \pm 0.2\ R_\odot$, and fills up its Roche lobe (Maxwell et al., 2014). Spectral analysis suggests an ONeMg–composition for the white dwarf, although not at the confidence level to rule out its fate as SN Ia progenitor (Mason, 2011, 2013). Both the ephemeris for the primary eclipse and the orbital period have been determined with high precision from optical light curve analysis:

$$E_{eclipse} = 2451234.5387 + N \cdot 1.23054695 \text{ days}, \tag{3.1}$$

with N the number of cycles since the eclipsing minimum at JD 2451234.5387 (Schaefer & Ringwald, 1995; Ness et al., 2012). With precise measurements of the orbital period before and after the nova outburst, the total amount of ejected mass was be estimated, as described by Equation 2.24 in section 2.2. In this way, U Sco was found to have ejected about $2.5 \cdot 10^{-5}\ M_\odot$ at its 2010 outburst, which is ten times the mass accreted since the previous outburst in 1999, and suggests that U Sco is not growing towards the Chandrasekhar mass limit (Schaefer, 2013). As no useful parallax has been obtained yet, *Gaia* only provides a lower limit of $D = 14.3$ kpc for the distance towards U Sco,

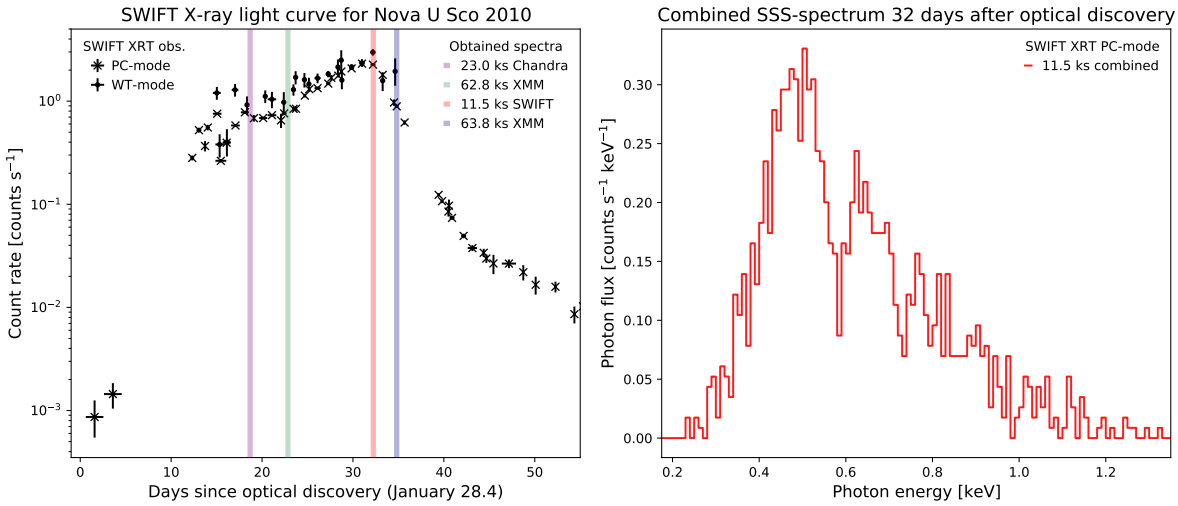

Figure 3.2: (a) *Swift* X–ray monitoring of U Sco in the 0.3–10.0 keV range. (b) *Swift XRT* spectrum showing U Sco as a SSS–continuum, 32 days after optical discovery.

which disagrees with light curve model–based distances of D = 3.3–8.6 kpc and the D = 12 ± 2 kpc distance derived from the companion's spectral flux (Schaefer, 2018; Kato, 1990; Schaefer, 2010a).

The most recent U Sco outburst was discovered by B. Harris on January 28th 2010, who observed a Johnson V–band magnitude of 7.88, compared to the quiescent state of V = 17.77, see the AAVSO light curve in Figure 3.1. As U Sco was predicted to erupt in 2009.3 ± 1.0, frequent optical monitoring of this system started before the actual outburst (Schaefer, 2005). From day 18 after optical discovery on, the fading light curve is sufficiently sampled by amateur observations to distinguish individual eclipses every 1.23 days. The exact timing of the 2010 eruption was extrapolated from this light curve to a Julian Date of 2455224.305 (Schaefer et al., 2010b). Within three hours of the optical discovery, the outburst was confirmed from optical and NIR–spectroscopy, with an expansion velocity for the ejecta of about 10000 km s^{-1} (Arai et al., 2010; Ashok et al., 2010; Das et al., 2010). A well–prepared multi–wavelength monitoring campaign was triggered, and less than 4 hours later U Sco was observed at X–ray energies by the *INTEGRAL* and *Swift* observatories. *INTEGRAL* did not detect any significant X–ray emission above 3 keV, which suggests that U Sco was surrounded by little matter that would cause shocked emission at hard X–rays (Manousakis et al., 2010). No X–ray photons were detected by *Swift* until 3 days later, once a faint spectral component emerged around 4.8 keV, indicating some weak collisional emission from the ejecta (Schlegel et al., 2010a).

Swift X–ray monitoring in the 0.3–10.0 keV range continued after five days of lunar constraints, see the X–ray light curve in Figure 3.2a. Each of these data points represents a single *Swift XRT* observation of $\sim$ 1 ks, extracted from the UK Swift Science Data Centre as described by Evans et al. (2007, 2009). Significant X–ray emission was detected 12 days after optical discovery, and the low–resolution *Swift* spectra revealed U Sco as a strong SSS–continuum: The observed spectra could be fitted with an absorbed blackbody of effective temperature 325 ± 93 kK and column density $N_H = (3.8 \pm 1.4) \cdot 10^{21}$ cm^{-2}, which indicated that the residual hydrogen–burning on top of the white

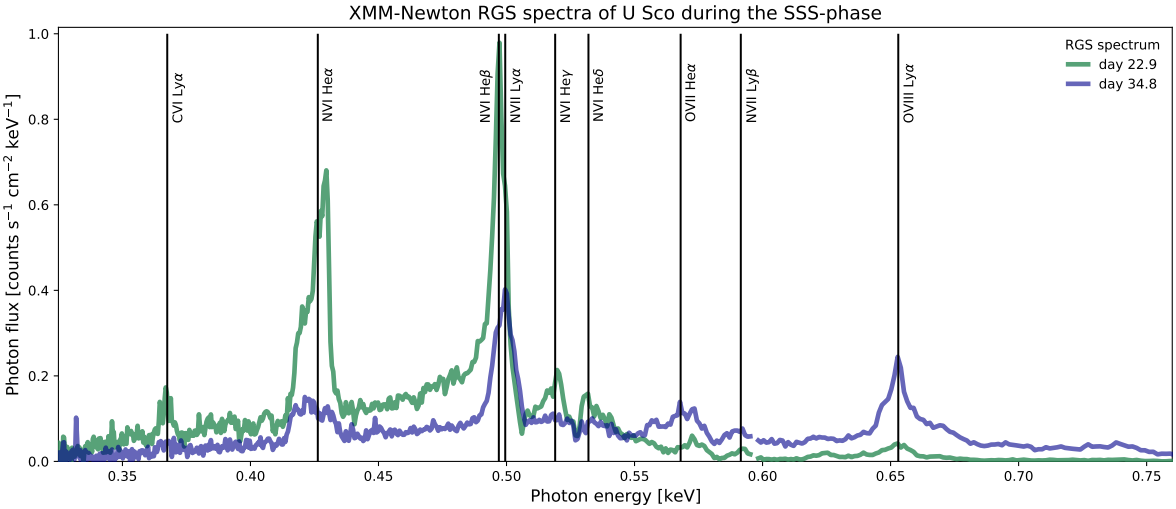

Figure 3.3: *RGS* spectra of U Sco during the SSS–phase with emission lines from Ness et al. (2010).

dwarf was exposed and U Sco had entered the SSS–phase (Schlegel et al., 2010b). The unabsorbed SSS–luminosity was found at $\sim 2 \cdot 10^{37}$ erg s^{-1}, with the associated soft X–ray photon flux being two orders of magnitude higher than the initial harder X–ray component (Schlegel et al., 2010b). From day 12 to day 33 after optical discovery, an X–ray–bright plateau at 1–2 counts s^{-1} was observed in the *Swift* light curve, see Figure 3.2a. On Figure 3.2b, an 11.5 ks combined *XRT* spectrum is shown, obtained at the end of this X–ray plateau and marked in red on Figure 3.2a, which demonstrates that U Sco was still burning residual hydrogen at SSS–energies on day 32, and proves that this plateau indicates the SSS–phase. The optical light curve formed a similar plateau during this SSS–phase, at a V–band magnitude of about 14 (see Figure 3.1), which suggests that soft X–ray radiation was reprocessed and contributed to the optical emission.

With short interval *Swift* observations during the SSS–phase, *UVOT* photometry detected strong UV eclipses, while *XRT* found only partial X–ray eclipses (Osborne et al., 2010). This suggests that a significant fraction of the soft X–ray emission emerged from a large scattering region around the hydrogen–burning white dwarf (Osborne et al., 2010). Observations during the X–ray eclipses have not been included in the *XRT* light curve for clarity (see Figure 3.2a), but will be discussed in section 3.4. Further *Swift* monitoring noticed a drop in the soft X–ray brightness on March 1st, 33 days after the optical discovery, and confirmed that the SSS–phase had ended (Schaefer et al., 2010a). At the UV, optical and IR bands, a fading light curve was observed, and the recurrent nova U Sco turned back to its quiescent state (Schaefer et al., 2010a).

3.2 High–resolution grating spectra

Next to its importance for studying the overall X–ray evolution of novae, *Swift* monitoring serves as guidance for deep observations with the *XMM–Newton* and *Chandra* X–ray grating observatories. The moment *Swift* confirmed U Sco to be at a bright SSS–state, target–of–opportunity obser-

vation were triggered on these missions, which are marked on the X–ray light curve in Figure 3.2a: One *Chandra* observation of 23.0 ks on day 18.7 (purple), an *XMM–Newton* observation of 63.8 ks on day 22.9 (green) and another *XMM–Newton* observation of 62.8 ks on day 34.8 (blue). The high–resolution *XMM–Newton RGS* grating spectra were extracted from the XMM–Newton Science Archive (XSA), and the *RG1+RGS2* merged spectra are shown in Figure 3.3.

Both X–ray spectra contain a SSS–continuum component, with strong emission lines superimposed. About 20 % of the total flux is centred at one of the prominent nitrogen lines: The hydrogen–like NVII Lyα line at 500 eV, and the helium–like NVI Heα and Heβ lines at 426 eV and 497 eV respectively (Orio et al., 2010, 2013). At 525 eV the OI Kα interstellar absorption line is observed. No strong carbon lines were detected (see Figure 3.3), and the overabundance in N over C is a result of the hot–CNO nuclear burning on top of the white dwarf surface. The emission line widths correspond to expansion velocities of about 3000 km s^{-1}, and the presence of more highly ionised lines in the second spectrum indicates a temperature increase from day 22.9 to day 34.9 (Ness et al., 2010).

The continuum component in each spectrum can be fitted with an absorbed blackbody model of effective temperature $T = 400$ kK and $T = 1000$ kK respectively, with sub–solar neutral oxygen abundances in order to reproduce the OI K absorption edge at 542 eV (Ness et al., 2012). The rise in temperature can also be observed from the Wien tail, which is only little affected by absorption and shifted towards higher energies by day 34.9. Blackbody emission serves as a first approximation for more realistic expanding NLTE white dwarf atmosphere models (van Rossum & Ness, 2010; van Rossum, 2012), and the absorbed blackbody fit merely indicates that the observed continuum component is of atmospheric origin. However, no atmospheric absorption lines can be observed in the high–resolution *RGS* spectra, which could be explained by Thomson scattering on a plasma of fast electrons, with random Doppler–shifts smearing out the continuum features (Ness et al., 2012).

Similar spectra were observed for Cal 87, which is a persistent supersoft X–ray source with an accretion disk blocking the direct X–ray radiation. Photospheric SSS–emission from the central white dwarf surface can only be observed after scattering on a highly ionised, optically thin accretion disk corona (Ebisawa et al., 2010). During the first *XMM–Newton* observation, the central X–ray source was eclipsed by the companion star without full suppression of the SSS–emission, which indicates that part of the X–rays were indeed reflected by a large scattering region (Ness et al., 2010). Further evidence for such accretion disk corona was found as reflected lines features in the *Chandra* grating spectra, that otherwise could not have escaped the high inclination system (Orio et al., 2013).

While our main focus is on the modelling of soft X–ray light curves, in the next section we will investigate the spectral effect of Thomson scattering by an accretion disk corona of fast electrons. The *XMM–Newton EPIC* X–ray light curves will be discussed in section 3.4.

3.3 Doppler–smeared absorption lines

In this section, we will study the Thomson scattering of soft photons by a plasma of relativistic electrons, and analyse the effect on SSS spectra. More specifically, we want to investigate if the

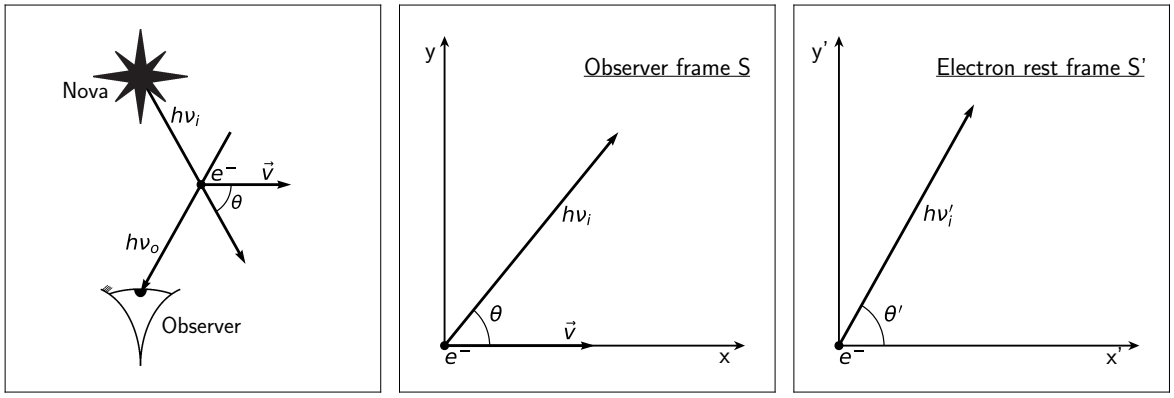

Figure 3.4: Definition of the inertial frame S and the inertial frame S'.

random Doppler–shifts on the photon energies can effectively spread out absorption lines, and in result blur the atmospheric absorption features from nova spectra.

3.3.1 Expression for the Doppler shift

The coordinate frame S, with (xy)–plane defined by the electron velocity $\vec{v}$ and the incoming photon direction, is shown in Figure 3.4. S is the inertial frame of the observer, while S' is the electron rest frame, obtained by Lorentz boosting the S frame by v along the joint x–direction. A Lorentz transformation on the incoming photon four-momentum P_{γ_i} yields:

$$\begin{aligned} h\nu_i' &= \gamma(h\nu_i - \beta p_{ix}c) \\ &= \gamma h\nu_i(1 - \beta\cos\theta) \qquad (3.2) \\ p_{ix}'c &= \gamma(p_{ix}c - \beta h\nu_i) \\ &= \gamma h\nu_i(\cos\theta - \beta) \qquad (3.3) \\ p_{iy}'c &= p_{iy}c \\ &= h\nu_i \sin\theta \qquad (3.4) \\ p_{iz}'c &= p_{iz}c = 0, \end{aligned}$$

with $P_\gamma c = (E,\ \vec{p}c)$, $\beta = v/c$, and $\gamma = (1-\beta^2)^{-1/2}$, using $E = pc = h\nu$ for photons. Equivalently, for the outgoing photon energy $h\nu_o$ there is a Lorenz transformation:

$$h\nu_o = \gamma(h\nu_o' + \beta p_{ox}'c). \qquad (3.5)$$

By dividing Equation 3.3 and 3.4 by Equation 3.2, two relations can be derived for the angle θ' between the incoming photon direction and the x'–axis in the S' frame:

$$\cos\theta' = \frac{p_{ix}'}{h\nu_i'} = \frac{\cos\theta - \beta}{1 - \beta\cos\theta} \qquad (3.6)$$

$$\sin\theta' = \frac{p_{iy}'}{h\nu_i'} = \frac{\sin\theta}{\gamma(1 - \beta\cos\theta)}. \qquad (3.7)$$

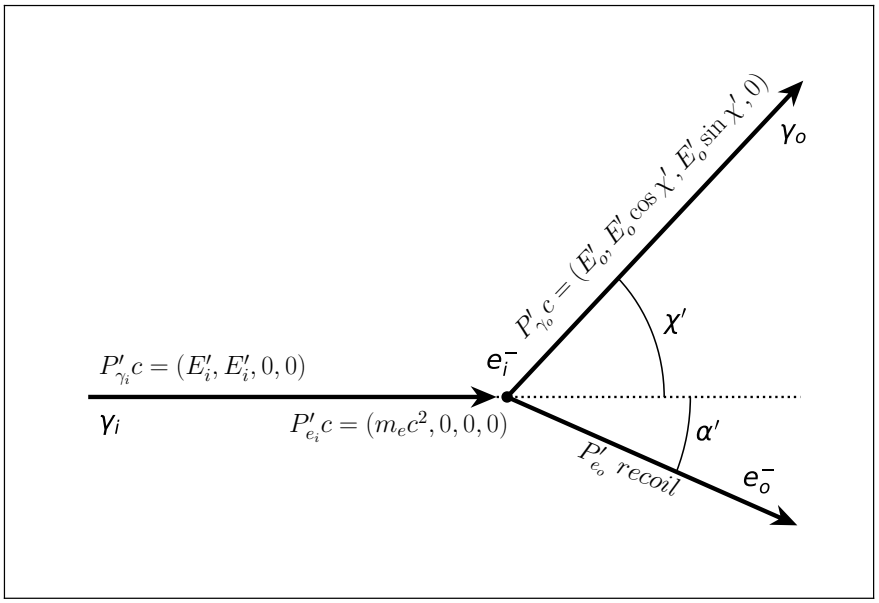

Figure 3.5: Photon scattering plane in the electron rest frame S'.

Now, we consider the scattering event in the electron rest frame, as illustrated in Figure 3.5. Conservation of four-momentum, with components as indicated on the figure, yields:

$$\begin{aligned}
P'_{\gamma_o} + P'_{e_o} &= P'_{\gamma_i} + P'_{e_i} \\
\iff {P'_{e_o}}^2 &= (P'_{\gamma_i} + P'_{e_i} - P'_{\gamma_o})^2 \\
\iff m_e^2c^2 &= m_e^2c^2 + 2P'_{\gamma_i}\cdot P'_{e_i} - 2P'_{\gamma_i}\cdot P'_{\gamma_o} - 2P'_{e_i}\cdot P'_{\gamma_o} \\
\iff E'_i &= E'_o\big(1 + \frac{E'_i}{m_ec^2}(1-\cos\chi')\big) \\
\iff h{\nu_o}' &= \frac{h{\nu_i}'}{1 + \frac{h{\nu_i}'}{m_ec^2}(1-\cos\chi')}.
\end{aligned} \tag{3.8}$$

This result is known as the Compton formula, which states that the incoming photon energy $h{\nu_i}'$ is reduced by a factor $1 - C(h{\nu_i}', \chi')$ when scattered on an electron at rest. The Compton factor $C(h{\nu_i}', \chi')$ follows from Equation 3.8:

$$\begin{aligned}
C(h{\nu_i}', \chi') &= \frac{h{\nu_o}'}{h{\nu_i}'} \\
&= \big(1 + \frac{h{\nu_i}'}{m_ec^2}(1-\cos\chi')\big)^{-1}.
\end{aligned} \tag{3.9}$$

In the electron rest frame, a photon can only lose energy, as energy is transferred to the recoiling electron. This energy loss increases with the scattering angle, and peaks when the photon is backscattered at $\chi' = \pi$, see Figure 3.6a. The Compton effect grows more significant at higher photon energies: For soft X–ray photons with $h{\nu_i}' \sim 0.5$ keV, the Compton factor is $\sim 99.8\%$ at $\chi' = \pi$ and $\sim 99.9\%$ at $\chi' = \pi/2$, see Figure 3.6b. Therefore, we can state that at soft energies scattering is practically elastic, with $h{\nu_o}' = h{\nu_i}'$. The same Compton factor $C(h{\nu_i}', \chi')$ appears in the differential

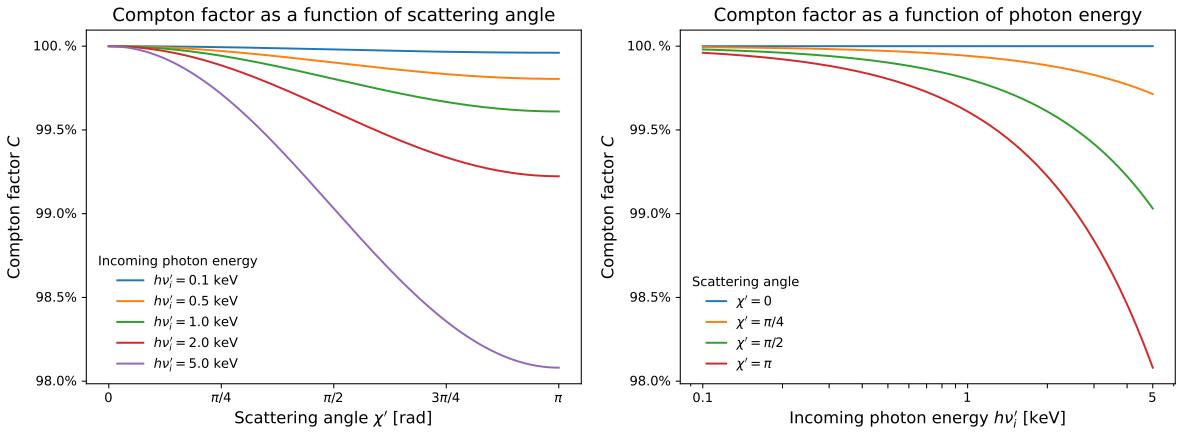

Figure 3.6: (a) The Compton factor $C = h\nu_o'/h\nu_i'$ as a function of the scattering angle. (b) The Compton factor as a function of the incoming photon energy.

cross section for Compton scattering, given by the Klein-Nishina formula (Klein & Nishina, 1929):

$$\frac{d\sigma}{d\Omega}(\chi', \phi') = \frac{\hbar^2\alpha^2}{2m_e^2c^2}\Big(C^3(h\nu_i{}', \chi') + C(h\nu_i{}', \chi') - C^2(h\nu_i{}', \chi')\sin^2\chi'\Big), \tag{3.10}$$

with α the fine-structure constant. At soft X–ray energies, $C \approx 1$ and the Klein-Nishina formula agrees with Thomson scattering at the 0.5% level (see Figure 3.7a). For $C = 1$, Equation 3.10 reduces to the differential cross section for Thomson scattering:

$$\begin{aligned}\frac{d\sigma}{d\Omega}(\chi', \phi') &= \frac{\hbar^2\alpha^2}{2m_e^2c^2}(2 - \sin^2\chi') \\ &= \frac{\hbar^2\alpha^2}{2m_e^2c^2}(1 + \cos^2\chi').\end{aligned}$$

Dealing with soft X–ray photons from novae, we continue with Thomson scattering as the appropriate low energy approximation to Compton scattering. Electrons have a total cross section for scattering:

$$\begin{aligned}\sigma_T &= \frac{\hbar^2\alpha^2}{2m_e^2c^2}\int_0^{2\pi} d\phi' \int_0^{\pi} \sin\chi' d\chi'(1 + \cos^2\chi') \\ &= \frac{\hbar^2\alpha^2}{m_e^2c^2}\frac{8\pi}{3} = 6.6525 \cdot 10^{-25} cm^2,\end{aligned} \tag{3.11}$$

and a normalised probability density function for the scattering angle χ' (see Figure 3.7b):

$$\Phi(\chi') = \frac{3}{8}(1 + \cos^2\chi')\sin\chi'. \tag{3.12}$$

With a random scattering angle χ' from this probability distribution, and an azimuth angle ϕ' uniform between 0 and 2π, the four-momentum $P_{\gamma_o}'c = (h\nu_o',\ \vec{p_o'}c)$ of the outgoing photon can be calculated. As for Thomson scattering the photon energy is conserved, $p_o'c$ equals $p_i'c$ in the electron rest frame. Vector $\vec{p_o'}$ is found by first rotating $\vec{p_i'}$ in the (x'y')–plane over χ' to $\vec{p_{\chi'}'}$, then rotating this $\vec{p_{\chi'}'}$ around $\vec{p_i'}$, over the angle ϕ' to $\vec{p_o'}$. The intermediate vector $\vec{p_{\chi'}'}$ will be in the (x'y')–plane,

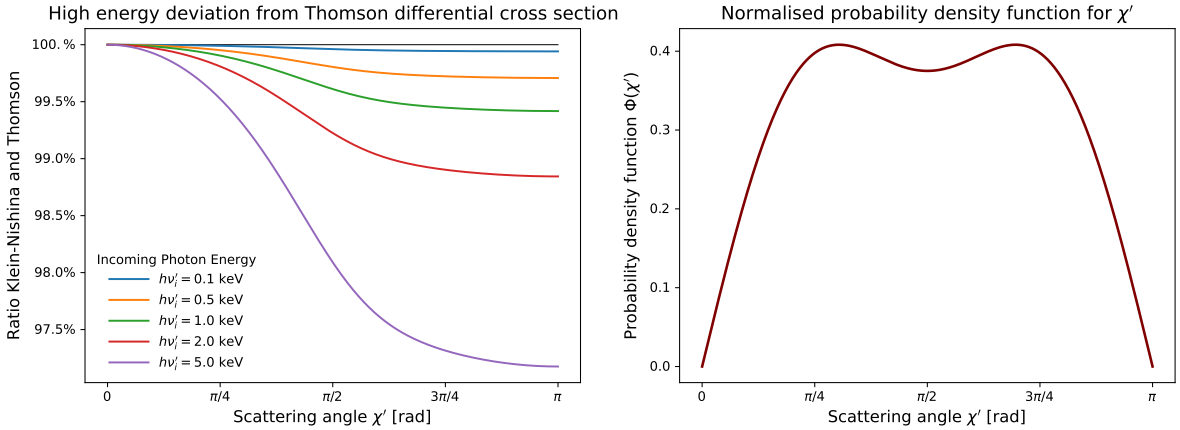

Figure 3.7: (a) Ratio of the Klein-Nishina and Thomson differential cross section as a function of the scattering angle for different photon energies. (b) Normalised probability density function for the Thomson scattering angle.

but most generally $\vec{p_o'}$ will not. First, vector $\vec{p_{\chi'}'}$ is found by performing a 2D rotation of $\vec{p_i'}$ in the (x'y')–plane over χ':

$$\vec{p_{\chi'}'} = (\cos\chi' p_{ix}' - \sin\chi' p_{iy}',\ \ \sin\chi' p_{ix}' + \cos\chi' p_{iy}',\ \ 0), \tag{3.13}$$

with

$$\vec{p_i'} = \frac{h\nu_i'}{c}(\cos\theta',\ \ \sin\theta',\ \ 0). \tag{3.14}$$

The next step applies the Rodrigues formula for 3D rotations citepRodrigues, which states that rotating a vector $\vec{u}$ over an angle α around a unit rotation axis $\vec{a}$, results in a new vector $\vec{c}$:

$$\vec{c} = \vec{u}\ \cos\alpha + (\vec{a}\times\vec{u})\ \sin\alpha + \vec{a}\ (\vec{a}\cdot\vec{u})\ (1-\cos\alpha).$$

Using this formula, $\vec{p_o'}$ is obtained by rotating $\vec{p_{\chi'}'}$ over an angle ϕ' around unit axis $\vec{p_i'}/p_i'$:

$$\begin{aligned}\vec{p_o'} &= \vec{p_{\chi'}'}\ \cos\phi' + \left(\frac{\vec{p_i'}}{p_i'}\times\vec{p_{\chi'}'}\right)\ \sin\phi' + \frac{\vec{p_i'}}{p_i'}\left(\frac{\vec{p_i'}}{p_i'}\cdot\vec{p_{\chi'}'}\right)(1-\cos\phi') \\ &= \vec{p_{\chi'}'}\ \cos\phi' + \vec{e_z'}\ p_i'\sin\chi'\sin\phi' + \vec{p_i'}\ \cos\chi'(1-\cos\phi'),\end{aligned} \tag{3.15}$$

with $p_i' = p_{\chi'}'$, as rotations do not change vector lengths, and:

$$\begin{aligned}\vec{p_i'}\times\vec{p_{\chi'}'} &= p_i'^2\ \sin\chi'\ \vec{e_z'} \\ \vec{p_i'}\cdot\vec{p_{\chi'}'} &= p_i'^2\ \cos\chi'.\end{aligned}$$

The x'–component of $\vec{p_o'}$ is found by combining Equation 3.13, 3.14 and 3.15 to:

$$\begin{aligned}p_{ox}' &= p_{\chi' x}'\cos\phi' + p_{ix}'\cos\chi'(1-\cos\phi') \\ &= p_{ix}'\cos\chi'\cos\phi' - p_{iy}'\sin\chi'\cos\phi' + p_{ix}'\cos\chi'(1-\cos\phi') \\ &= p_{ix}'\cos\chi' - p_{iy}'\sin\chi'\cos\phi' \\ &= \frac{h\nu_i'}{c}\big(\cos\theta'\cos\chi' - \sin\theta'\sin\chi'\cos\phi'\big).\end{aligned} \tag{3.16}$$

We are interested in how the incoming photon energy $h\nu_i$ shifts to an energy $h\nu_o$ in the reference frame of the observer, as this is how spectral features could be spread by scattering on a plasma of fast electrons. For soft photons with $h\nu_o{}' = h\nu_i{}'$, connecting Equation 3.5 with respectively Equation 3.16, 3.2, 3.6 and 3.7, leads to $h\nu_o$ as a function of $h\nu_i$:

$$\begin{aligned}
h\nu_o &= \gamma(h\nu_i' + \beta p_{ox}' c) \\
&= \gamma h\nu_i'\big(1 + \beta(\cos\theta'\cos\chi' - \sin\theta'\sin\chi'\cos\phi')\big) \\
&= \gamma^2 h\nu_i\big(1 - \beta\cos\theta\big)\big(1 + \beta(\cos\theta'\cos\chi' - \sin\theta'\sin\chi'\cos\phi')\big) \\
&= \gamma^2 h\nu_i\big(1 - \beta\cos\theta\big)\left(1 + \frac{\beta(\cos\theta - \beta)\cos\chi'}{1 - \beta\cos\theta} - \frac{\beta\sin\theta\sin\chi'\cos\phi'}{\gamma(1 - \beta\cos\theta)}\right) \\
&= h\nu_i\left(\frac{1 + \beta\cos\theta(\cos\chi' - 1) - \beta^2\cos\chi'}{1 - \beta^2} - \frac{\beta\sin\theta\sin\chi'\cos\phi'}{\sqrt{1 - \beta^2}}\right).
\end{aligned}$$

And so the Doppler factor $f = h\nu_o / h\nu_i$, by which the incoming photon energy changes, is:

$$\boxed{f(\theta,\ \chi',\ \phi') = \frac{1 + \beta\cos\theta(\cos\chi' - 1) - \beta^2\cos\chi'}{1 - \beta^2} - \frac{\beta\sin\theta\sin\chi'\cos\phi'}{\sqrt{1 - \beta^2}}.} \tag{3.17}$$

This factor can be written as a Maclaurin series in β, which allows the first order contribution to f, and higher order corrections with increasing β to be distinguished:

$$\begin{aligned}
f &= \big(1 + A\beta - B\beta^2 - C\beta(1 - \beta^2)^{1/2}\big)\big(1 - \beta^2\big)^{-1} \\
&= \big(1 + A\beta - B\beta^2 - C\beta + \frac{C\beta^3}{2} + \mathcal{O}(\beta^5)\big)\big(1 + \beta^2 + \mathcal{O}(\beta^4)\big) \\
&= 1 + (A - C)\beta + (1 - B)\beta^2 + (A - \frac{C}{2})\beta^3 + \mathcal{O}(\beta^4),
\end{aligned} \tag{3.18}$$

with $A = \cos\theta(\cos\chi' - 1)$, $B = \cos\chi'$ and $C = \sin\theta\sin\chi' cos\phi'$. The first order relative shift f_1 on the incoming photon energy is defined as $\Delta h\nu / h\nu_i = f_1 + \mathcal{O}(\beta^2)$ and given by:

$$\boxed{f_1(\theta,\ \chi',\ \phi') = \big(\cos\theta(\cos\chi' - 1) - \sin\theta\sin\chi' cos\phi'\big)\beta.} \tag{3.19}$$

3.3.2 *SKIRT* implementation

We now have a look at the *SKIRT* implementation for the Doppler shift on photon energies in result of Thomson scattering by a population of fast electrons. The *SKIRT* code version 9 does allow photons to scatter on a medium of moving electrons; however, photon wavelengths are only shifted in a non–relativistic manner, i.e. *SKIRT* operates in the $\beta \ll 1$ regime, with electron velocities v well below the speed of light. The effect of this non–relativistic implementation will be studied in this section. The *SKIRT* code keeps track of wavelengths instead of photon energies, and the observed wavelength λ_o is shifted from its value λ_o' at the electron rest frame by the function

`PhotonPackage::shiftedEmissionWavelength`:

$$\begin{aligned} h\nu_o &= \frac{hc}{\lambda_o} \\ &\equiv \frac{hc}{\lambda'_o(1-\beta k'_{ox})} \\ &= \frac{h\nu'_o}{1-\beta k'_{ox}}, \end{aligned} \tag{3.20}$$

which is a non–relativistic approximation of the exact Lorentz transformation on P'_{γ_o}:

$$\begin{aligned} h\nu_o &= \gamma h\nu'_o(1+\beta k'_{ox}) \\ &= \frac{h\nu'_o}{\gamma(1-\beta k_{ox})}. \end{aligned}$$

Both results for $h\nu_o$ agree in the non–relativistic limit of $\gamma = 1$ and $\vec{k_o} = \vec{k'_o}$ (*SKIRT* does not take relativistic aberration into account, i.e. angles are not altered by Lorentz boosting). The *SKIRT* implementation of Thomson scattering is exact, with $\cos\chi'$ generated from the Thomson scattering phase function by the function `ElectronMix::generateCosineFromPhaseFunction`, azimuth angle ϕ'_S uniform between 0 and 2π, and $h\nu'_o = h\nu'_i$. Given the value for $\cos\chi'$, the outgoing photon direction $\vec{k'_o}$ is calculated by the function `Random::direction`, which first rotates $\vec{k'_i}$ over χ' towards the z'–axis, then rotates this vector to $\vec{k'_o}$ over a random ϕ'_S around $\vec{k'_i}$ according to the right hand rule:

$$\begin{aligned} k'_{ox} &= k'_{ix}\cos\chi' + k'_{iy}\sin\chi'\sin\phi'_S \\ &= k'_{ix}\cos\chi' - k'_{iy}\sin\chi'\cos\phi'. \end{aligned} \tag{3.21}$$

Because *SKIRT* first rotates $\vec{k'_i}$ towards the z'–axis and not in the (x'y')–plane, $\phi'_S = \phi' - \frac{\pi}{2}$, with $\sin\phi'_S = -\cos\phi'$. Multiplying Equation 3.21 by p'_o yields the same expression for p'_{ox} as Equation 3.16. As *SKIRT* does not take relativistic aberration into account, $\vec{k'_i} = \vec{k_i}$ with:

$$k'_{ix} = k_{ix} = \cos\theta \tag{3.22}$$

$$k'_{iy} = k_{iy} = \sin\theta, \tag{3.23}$$

instead of Equation 3.6 and 3.7 respectively. Incoming photon wavelengths λ_i are Doppler shifted to λ'_i by the function `PhotonPacket::shiftedReceptionWavelength`:

$$\begin{aligned} h\nu'_i &= \frac{hc}{\lambda'_i} \\ &\equiv \frac{hc}{\lambda_i}(1-\beta\cos\theta) \\ &= h\nu_i\,(1-\beta\cos\theta), \end{aligned} \tag{3.24}$$

in contrast to the exact expression $\gamma h\nu_i(1-\beta\cos\theta)$ in Equation 3.2, but again consistent in the non–relativistic limit of $\gamma = 1$. Combining Equation 3.20 with $h\nu'_o = h\nu'_i$ and Equations 3.21–3.24,

SKIRT obtains an outgoing photon energy:

$$\begin{aligned} h\nu_o &\equiv \frac{h\nu'_i}{1-\beta k'_{ox}} \\ &\equiv \frac{h\nu'_i}{1-\beta(k'_{ix}\cos\chi' - k'_{iy}\sin\chi'\cos\phi')} \\ &\equiv \frac{h\nu'_i}{1-\beta(\cos\theta\cos\chi' - \sin\theta\sin\chi'\cos\phi')} \\ &\equiv \frac{h\nu_i\,(1-\beta\cos\theta)}{1-\beta(\cos\theta\cos\chi' - \sin\theta\sin\chi'\cos\phi')}, \end{aligned}$$

which results in a Doppler factor $f_S = h\nu_o/h\nu_i$, to be compared with f in Equation 3.17:

$$\boxed{f_S(\theta,\ \chi',\ \phi') = \frac{1-\beta\cos\theta}{1-\beta(\cos\theta\cos\chi' - \sin\theta\sin\chi'\cos\phi')}.} \tag{3.25}$$

This expression for f_S can be written as a Maclaurin series in β:

$$\begin{aligned} f_S &= (1-A\beta)(1+B\beta+B^2\beta^2+\mathcal{O}(\beta^3)) \\ &= 1+(B-A)\beta+(B^2-AB)\beta^2+\mathcal{O}(\beta^3), \end{aligned} \tag{3.26}$$

with $A = \cos\theta$ and $B = \cos\theta\cos\chi' - \sin\theta\sin\chi'\cos\phi'$. The first order relative shift f_{S1} on the incoming photon energy as calculated by *SKIRT*, is then given by:

$$f_{S1}(\theta,\ \chi',\ \phi') = \big(\cos\theta(\cos\chi'-1) - \sin\theta\sin\chi' cos\phi'\big)\beta,$$

which is the same first order result for the Doppler shift as the exact formula, Equation 3.19. However, the second order correction to f_S (see Equation 3.26) deviates from the $(1-\cos\chi')\beta^2$ term in the expansion for f (see Equation 3.18). The non–relativistic implementation in *SKIRT* is exact up to first order in β, which works perfectly for its intended use at $\beta \ll 1$. For a plasma of relativistic electrons, as $\beta > 0.01$, higher order corrections to Equation 3.19 should be taken into account to obtain a 1% precision on the result.

3.3.3 Doppler–shifted photons

We can now study how Thomson scattering on a plasma of relativistic electrons does shift soft X–ray photon energies. For a given electron speed $v = \beta c$, the probability distribution for the Doppler factor $f(\theta,\chi',\phi')$ can be obtained numerically from Equation 3.17, with scattering angle χ' distributed according to the normalised probability density function $\Phi(\chi')$ given by Equation 3.12, and a uniform distribution for both angles θ and ϕ'. Using the univariate transformation method for probabilities, a

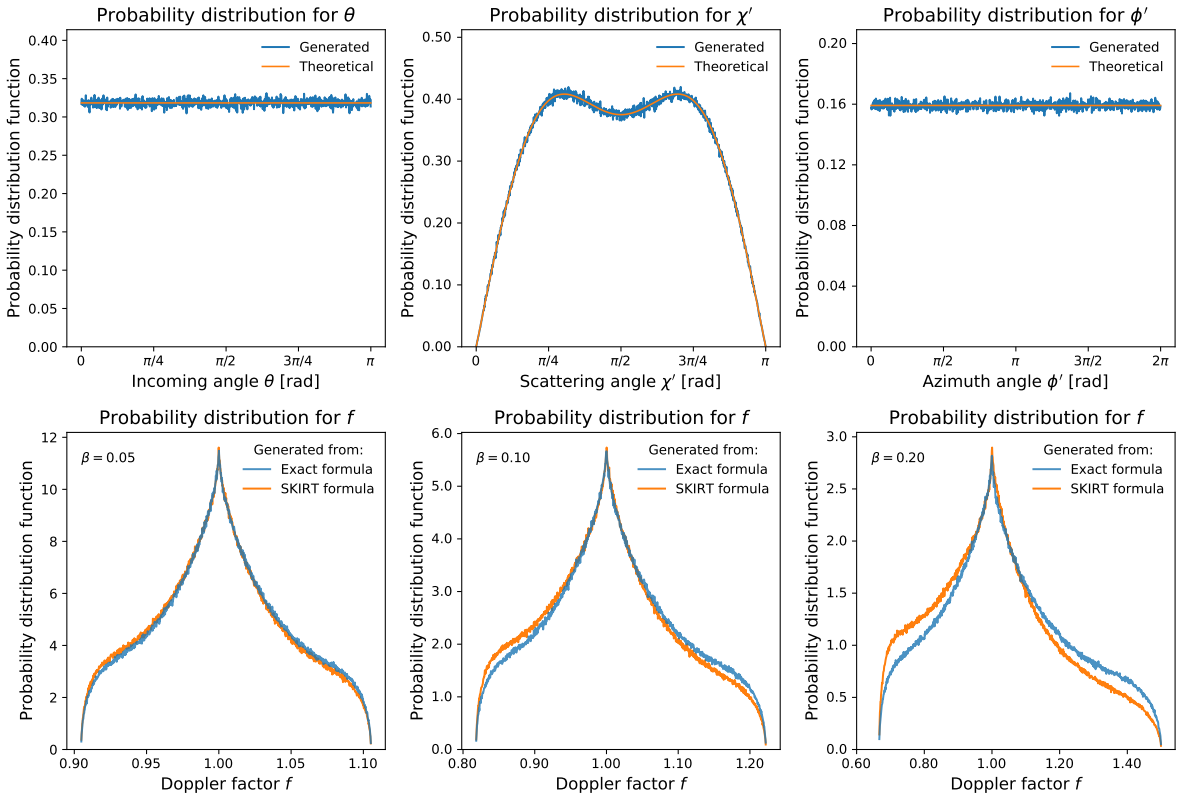

Figure 3.8: Normalised probability density function for the incoming angle θ, the scattering angle χ', the azimuth angle ϕ', and the Doppler factor $f = h\nu_o/h\nu_i$ at three different electron velocities.

random χ' between 0 and π can be generated from a uniform deviate U_1 between 0 and 1:

$$\begin{aligned} U_1 &= \int_0^{\chi'} \Phi(x)dx \\ &= \frac{3}{8}\int_0^{\chi'} \sin x\,(1+\cos^2 x)\,dx \\ &= \frac{3}{8}\int_{\cos\chi'}^{1} (1+u^2)\,du \\ &= \frac{1}{2} - \frac{3\cos\chi'}{8} - \frac{\cos^3\chi'}{8}. \end{aligned}$$

This is a cubic equation in $\cos\chi'$, with only one non–complex root:

$$\cos\chi' = \sqrt[3]{\sqrt{16U_1^2 - 16U_1 + 5} - 4U_1 + 2} - \frac{1}{\sqrt[3]{\sqrt{16U_1^2 - 16U_1 + 5} - 4U_1 + 2}}. \tag{3.27}$$

As $f(\theta, \chi', \phi')$ does only contain the scattering angle in the form of $\cos\chi'$ and $\sin\chi'$, Equation 3.27 can be used to generate a random $\cos\chi'$, and from this cosine, $\sin\chi'$ can be calculated as $\sqrt{1-\cos^2\chi'}$. After a substitution $U_1 \leftrightarrow 1-U_1$, Equation 3.27 is the same formula as the one used in the *SKIRT* implementation `ElectronMix::generateCosineFromPhaseFunction`. Both formulas for $\cos\chi'$ are equivalent, as both $1-U_1$ and U_1 will be distributed uniformly between 0 and 1. Generating a random θ between 0 and π, and a random ϕ' between 0 and 2π, starting from two uniform

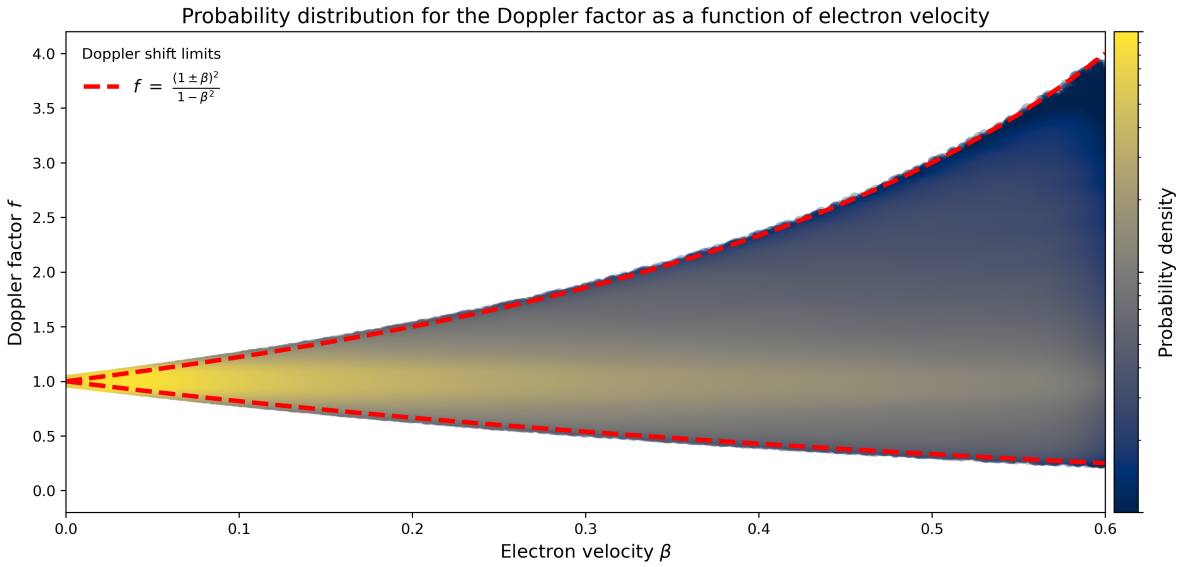

Figure 3.9: Doppler factor $f = h\nu_o/h\nu_i$ as a function of the electron velocity $v = \beta c$.

deviates U_2 and U_3, is much more straightforward:

$$\theta = \pi\, U_2 \tag{3.28}$$

$$\phi' = 2\pi\, U_3. \tag{3.29}$$

From a large number of (θ, χ', ϕ')–points, generated as described by Equation 3.27–3.29 (top panel Figure 3.8), the probability distribution for the Doppler factor f (Equation 3.17) is obtained numerically for three fixed electron velocities, as shown in the bottom panel of Figure 3.8. At low β, the Doppler factor shows little variation around $f = 1$. In the limit of $\beta \to 0$, the distribution reduces to a Dirac delta on $f = 1$. When using the *SKIRT* formula (Equation 3.25) for f instead, both probability distributions agree in the low–relativistic regime only, as the *SKIRT* implementation is only exact up to first order in β. Towards higher electron velocities, the dispersion around $f = 1$ increases and the distribution becomes more asymmetric, with a longer tail towards strong Doppler upshifts, but always limited by the lower bound $f = 0$, as photon energies cannot become negative. The bottom panel of Figure 3.8 suggests that the Doppler shift limits for the *SKIRT* implementation are equal to the exact limits. In Figure 3.9, the distribution for f is shown as a function of the electron velocity, up to $\beta = 0.6$. For each β, Doppler shifts range between a maximum of $f = \frac{1+\beta}{1-\beta}$ for $\theta = \pi$ and $\chi' = \pi$ (head-on backscattering), and a minimum of $f = \frac{1-\beta}{1+\beta}$ for $\theta = 0$ and $\chi' = \pi$ (parallel backscattering), see Equation 3.17. At these angles, the exact and *SKIRT* formula for f both reach their global extrema at the same f–values, and so *SKIRT* obtains the same Doppler shift limits, see Figure 3.8.

For each β, there is a single distribution for the Doppler factor, independent of $h\nu_i$. However, the probability distribution for the outgoing photon energy will be a function of the incoming energy, as $h\nu_o = f h\nu_i$. There will be larger Doppler shifts on high energy photons, and in result the high energy side of a source spectrum will be spread out more than the low energy side. For a fixed electron velocity β and a given $h\nu_i$, the probability distribution for the outgoing photon energy $h\nu_o$

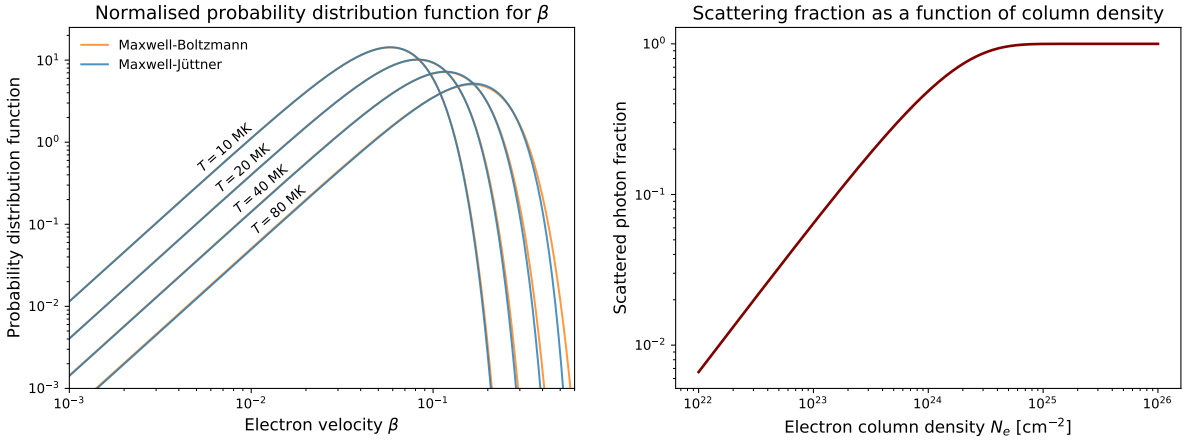

Figure 3.10: (a) Normalised Maxwell–Boltzmann and Maxwell–Jüttner probability distribution at different T. (b) Scattered photon fraction $1 - e^{-N_e \sigma_T}$ as a function of the column density.

can be written as:

$$R(h\nu_o;\, h\nu_i) = \frac{\Phi_f\left(\frac{h\nu_o}{h\nu_i}\right)}{h\nu_i}, \tag{3.30}$$

with Φ_f the normalised probability distribution for f at β (see Figure 3.8), and $R(h\nu_o;\, h\nu_i)$ normalised to one for each $h\nu_i$. $R(h\nu_o;\, h\nu_i)$ can be interpreted as the photon redistribution function $h\nu_i \rightarrow h\nu_o$, and has the same shape of Φ_f, but centred on $h\nu_i$, stretched in the horizontal direction by a factor $h\nu_i$ and normalised to one by an extra factor $1/h\nu_i$.

For an astrophysical plasma of electrons, the electron velocity may not be constant throughout the medium. It will follow its own probability distribution $\Phi(\beta)$, from which β needs to be generated in calculating the Doppler factor f. For example, consider a thermal plasma at temperature T, with a Maxwell–Boltzmann distribution for the electron velocity:

$$\Phi(\beta) = \sqrt{\frac{2}{\pi}\left(\frac{m_e c^2}{kT}\right)^3}\, \beta^2 e^{-\frac{m_e c^2 \beta^2}{2kT}}. \tag{3.31}$$

The above distribution is normalised between $\beta = 0$ and $\beta = +\infty$, and describes the behaviour of a non–relativistic gas. Deviations from the relativistic Maxwell–Jüttner distribution (Jüttner, 1911), which is normalised between $\beta = 0$ and $\beta = 1$, are negligibly small for temperatures below 80 MK (see Figure 3.10a). The Maxwell–Boltzmann distribution can be used to describe thermal electrons with relativistic speeds up to $\beta \sim 0.2$. Generating velocities from Equation 3.31 is easily implemented, and we come back to this in subsection 3.3.5. In the next subsection, we study the effect of Doppler shifts at fixed β on spectral absorption features.

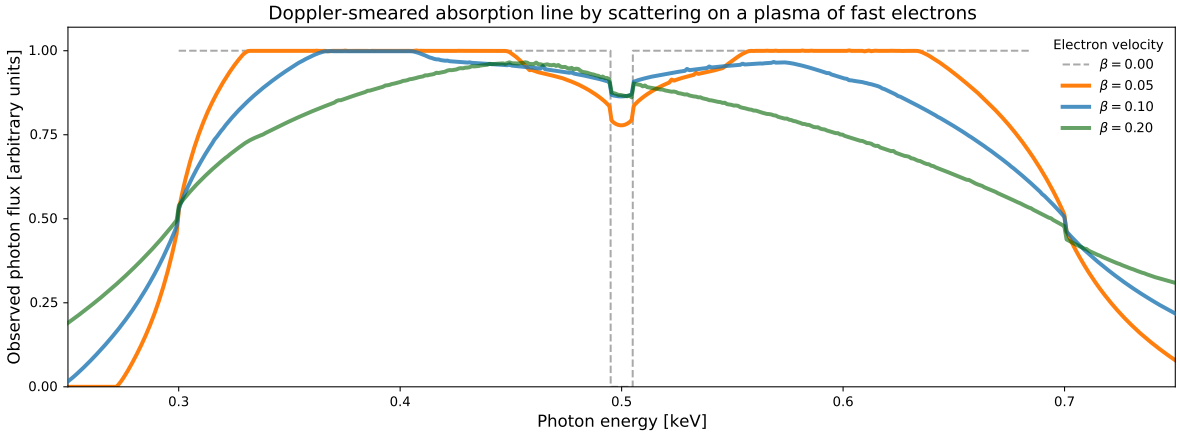

Figure 3.11: Doppler–smeared absorption line of width $W = 0.01$ keV, for various fixed electron velocities and an electron column density $N_e = 5 \cdot 10^{24}$ cm^{-2}.

3.3.4 Smeared absorption lines

We consider a square toy model for an absorption line of width W, superimposed on a flat SSS–continuum and defined by:

$$F_{h\nu}(h\nu) = \begin{cases} 1 & 0.3 \text{ keV} < h\nu < 0.5 \text{ keV} - W/2 \\ 0 & 0.5 \text{ keV} - W/2 < h\nu < 0.5 \text{ keV} + W/2 \\ 1 & 0.5 \text{ keV} + W/2 < h\nu < 0.7 \text{ keV}, \end{cases} \tag{3.32}$$

with $F_{h\nu}$ the photon flux emitted by the source in arbitrary units. The fraction of photons that scatters on an electron when sent through an electron cloud, depends on the total number of electrons in this cloud. This can be characterised by the column density N_e, which is defined as the surface density obtained by integrating the electron number density n_e along the path through the cloud. When traversing a medium of column density N_e, the optical depth will be $\tau = N_e \sigma_T$, with σ_T the Thomson scattering cross section given by Equation 3.11. The fraction of scattered photons is shown for a variety of column densities in Figure 3.10b. After the first scattering event, photons can scatter a second time and even more, and so gain additional Doppler shifts. This is a complex problem that should be studied using a MCRT code such as *SKIRT*, as each photon scatters at a random location, into a random direction.

Given the source spectrum $F_{h\nu}(h\nu)$ in Equation 3.32 and only considering primary scattering, the observed spectrum $O_{h\nu}(h\nu)$ that emerges from the electron cloud can be calculated:

$$O_{h\nu}(h\nu_o) = e^{-N_e\sigma_T} F_{h\nu}(h\nu_o) + (1 - e^{-N_e\sigma_T}) \int_{0.3 \text{ keV}}^{0.7 \text{ keV}} F_{h\nu}(h\nu_i)\, R(h\nu_o;\, h\nu_i)\, dh\nu_i, \tag{3.33}$$

with redistribution function $R(h\nu_o;\, h\nu_i)$ given by Equation 3.30 and a functional form for the probability distribution Φ_f obtained by interpolation on the numerical distribution in Figure 3.8. For a given column density N_e, Equation 3.33 can be integrated numerically for each $h\nu_o$, and so the resulting spectrum $O_{h\nu}(h\nu)$ can be obtained. For an N_e of $5 \cdot 10^{24}$ cm^{-2}, the scattering fraction

$1 - e^{-N_e \sigma_T} = 0.964$ and spectra for different fixed electron velocities are shown in Figure 3.11. The figure illustrates how the spectrum is spread out more at higher photon energies, as discussed in the previous subsection. Although the function Φ_f was obtained from a Monte Carlo method on Equation 3.17, little Poisson noise can be observed on the results, as Φ_f was sufficiently sampled by 5 million (θ, χ', ϕ')–points over a thousand f–bins. The integral of $F_{h\nu}(h\nu)$ over the full energy range yields 0.39 in arbitrary photon units. When the emerging photon flux $O_{h\nu}(h\nu)$ is numerically integrated, the same value is obtained, as Thomson scattering conserves the total number of photons while shifting them between energy bins. From the spectra in Figure 3.11, one can see that scattering on a plasma of relativistic electrons provides an efficient mechanism for smearing out spectral absorption lines. Thomson scattering on an accretion disk corona above the nova system might provide a plausible explanation for the absence of atmospheric absorption features in nova spectra.

3.3.5 Electron scattering with *SKIRT*

In the previous subsection, we modelled the effect of Thomson scattering on absorption lines in SSS–spectra. However, we made a hard division between one fraction of photons scattering just once before being observed, and a second fraction which was observed without being scattered. More advanced scattering modes or the possibility to scatter multiple times were not taken into account. Also, electrons inside the cloud could only have a single fixed velocity β. Within these limitations, Doppler–smeared absorption lines were obtained using the exact formula in Equation 3.17. When interested in the effect on photons travelling through a cloud of electrons with a certain velocity dispersion, e.g. a thermal plasma at temperature T, the Monte Carlo method from the previous subsection could be repeated for generating a new probability distribution for f. This time a large number of random electron velocities β should be generated from Equation 3.31, in addition to random angles θ, χ' and ϕ' as shown in the top panel of Figure 3.8. In this way, the distribution for the Doppler factor can again be obtained numerically, with results similar to those in the bottom panel of Figure 3.8.

Here, we approach this problem using *SKIRT*, and perform a direct simulation of photon propagation through a medium of thermal electrons. When electron velocities are distributed by a Maxwell–Boltzmann distribution, each Cartesian velocity coordinate will be distributed according to a normalised Gaussian, centred on $\mu = 0$ with variance $\sigma^2 = \frac{kT}{m_e c^2}$:

$$\Phi(\beta_i) = \sqrt{\frac{m_e c^2}{2\pi kT}} e^{-\frac{m_e c^2 \beta_i^2}{2kT}}.$$

In *SKIRT*, Gaussian deviates G_i, with $\mu = 0$ and $\sigma = 1$, can easily be generated by the function `random::gauss`, which uses an efficient implementation of the Box–Muller method from Press et al. (2002). From three such Gaussian deviates, a random electron velocity is obtained as:

$$\vec{\beta} = \sqrt{\frac{kT}{m_e c^2}} \, (G_1, \, G_2, \, G_3), \tag{3.34}$$

with a magnitude β distributed according to the Maxwell–Boltzmann distribution.

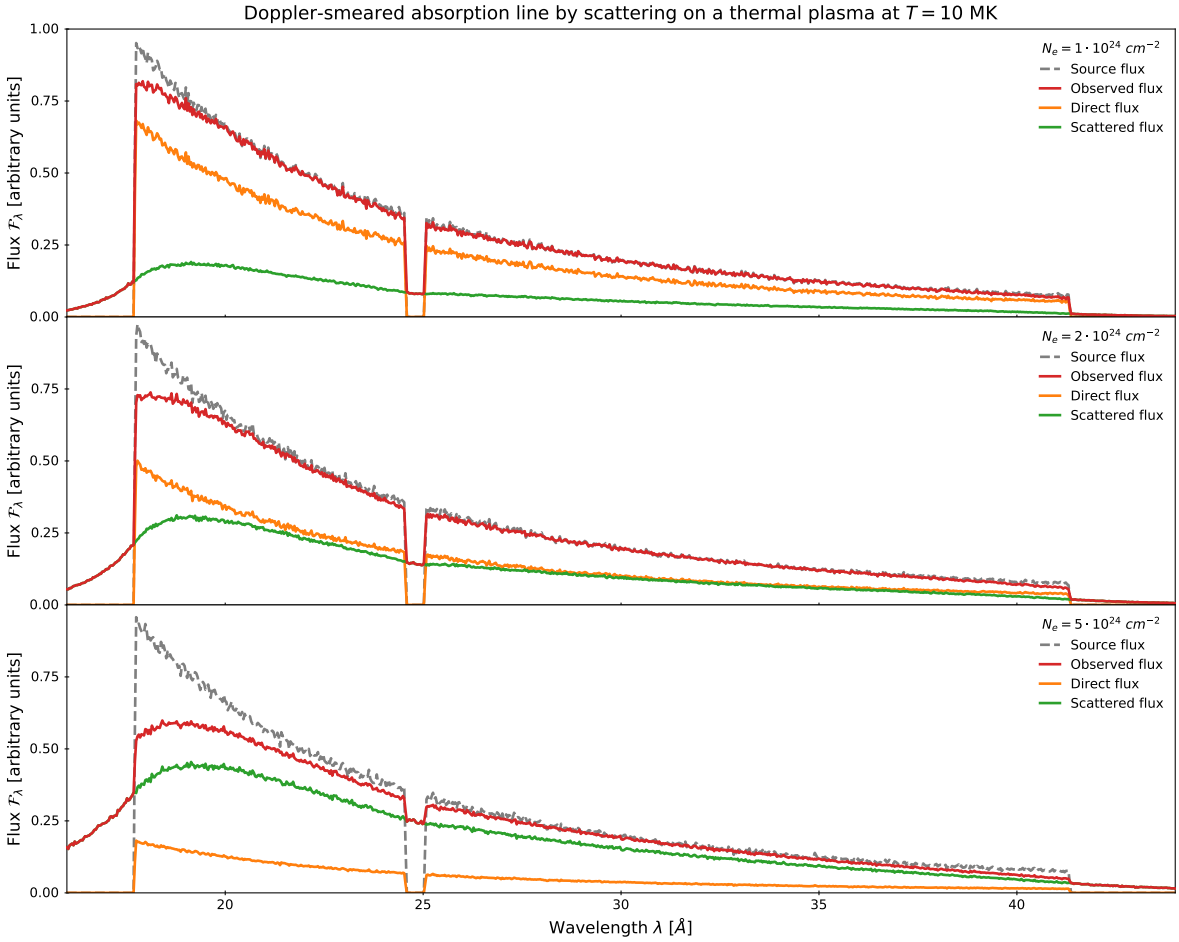

Figure 3.12: Doppler–smeared absorption line of width $W_\lambda = 0.50$ Å, for various electron column densities at $T = 10$ MK.

Proceeding with *SKIRT*, we can now incorporate a more general treatment of scattering. In the MCRT approach, each photon interacts at an optical depth τ along the photon path, drawn from the exponential distribution in Equation 2.32. If this τ is larger than the total optical depth of the transfer medium, the photon will pass through without interaction. Otherwise, it determines the location where scattering will happen, as free electrons cannot absorb photons. The photon is then redirected into a new direction, drawn from the differential cross section for Thomson scattering. In addition, the photon energy is updated with a non–relativistic Doppler factor, given by Equation 3.25. The photon will continue on its new path, and a next τ is drawn to determine a possible interaction point for further scattering. *SKIRT* takes into account a more realistic sequence of scattering events, compared to just applying one single Doppler shift or none at all, as was done in the previous subsection.

We set up a *SKIRT* simulation for a model that represents a transfer medium of thermal electrons at temperature T. The model configuration contains a spherically symmetric shell of electrons, centred on a point source at the origin, which is observed from the outside. The total number of electrons is set by the column density N_e in the radial direction, and the velocity dispersion follows from the electron temperature T, see Equation 3.31. The central point source has a spectral energy distribution

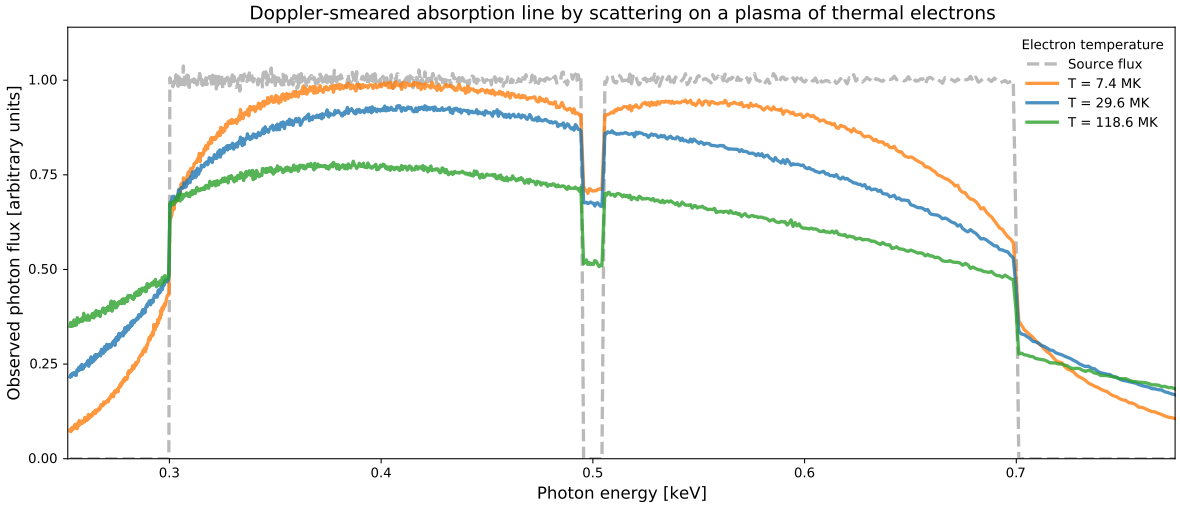

Figure 3.13: Doppler–smeared absorption line of width $W = 0.01$ keV, for various temperatures and an electron column density of $N_e = 5 \cdot 10^{24}$ cm^{-2}.

as given by Equation 3.32, and this photon flux $F_{h\nu}$ in units s^{-1} cm^{-2} keV^{-1} can be converted to an energy flux $\mathcal{F}_\lambda$ in units W m^{-1} as needed for *SKIRT* input SEDs:

$$\mathcal{F}_\lambda(\lambda) = 1.602 \cdot 10^{-16} \cdot \frac{(h\nu)^3}{hc}\, F_{h\nu}\Big(\frac{hc}{10^{-6} \cdot \lambda}\Big), \tag{3.35}$$

with λ the wavelength in micron, $h\nu$ the photon energy in keV, $hc = 1.240 \cdot 10^{-9}$ keV m and 1 keV $= 1.602 \cdot 10^{-16}$ J. As $F_{h\nu}$ is a flat photon spectrum, the energy flux $\mathcal{F}_\lambda$ will follow a power law $\mathcal{F}_\lambda \propto \lambda^{-3}$, shown as the source flux in Figure 3.12. Centred on $\lambda = 24.80$ Å, a single absorption line of width $W_\lambda = 0.50$ Å is superimposed on this power-law continuum. The spectral energy distribution of the central point source is normalised to a luminosity of $10^4 \cdot L_\odot$ in the 0.3–0.7 keV range, a typical value for novae in their SSS–phase.

Simulation results for three different electron column densities at $T = 10$ MK are shown in Figure 3.12. The observed flux is the sum of a direct flux component, observed without being scattered, and a scattered flux component, summed over all scattering levels. At each wavelength, the direct flux is a fraction of the source flux, and shows a distinct absorption line. At the originally absorbed wavelengths around $\lambda = 24.80$ Å, the observed flux equals the scattered flux, which is essentially flat over the absorption line for all N_e at this temperature. So at 10 MK, the absorption line is already flattened in the scattered spectrum, and the residual absorption feature as observed originates entirely from the direct flux component. The scattered flux fraction will increase at the expense of the direct flux with increasing optical depth, i.e. at higher N_e. At this temperature, the level to which the absorption line is blurred, is set by the electron column density N_e, which determines the relative importance of the scattered flux. For column densities beyond $N_e = 5 \cdot 10^{24}$ cm^{-2}, noise starts to dominate the simulated spectrum, as too few photons emerge from the optically thick electron shell to be efficiently treated in a Monte Carlo scheme (Camps & Baes, 2018).

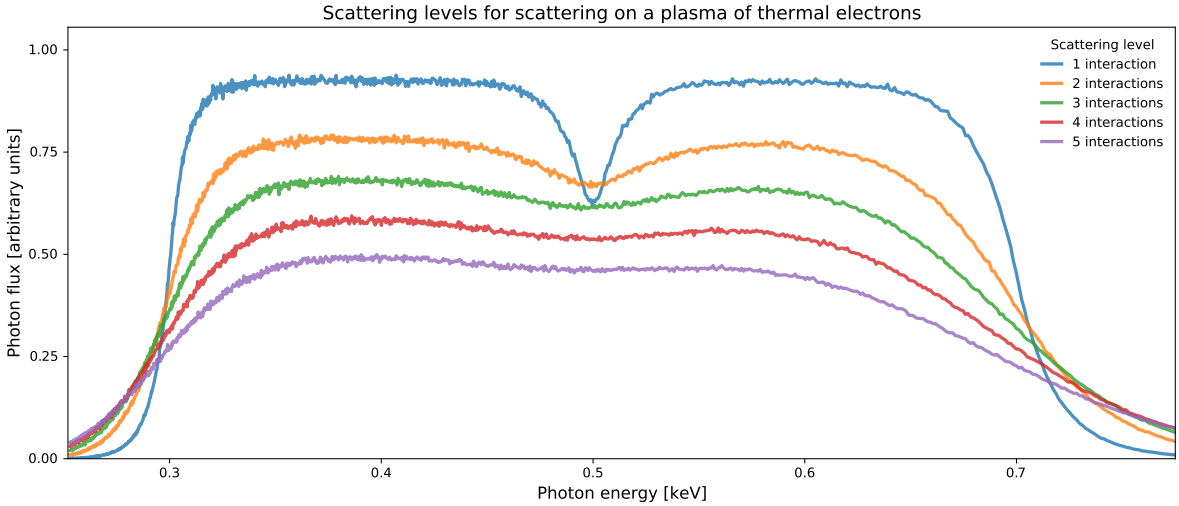

Figure 3.14: Contribution of the different scattering levels to the scattered component of the observed photon flux, for an electron column density of $N_e = 5 \cdot 10^{23}$ at 7.4 MK.

In Figure 3.13, simulation results are shown for a thermal plasma at three different electron temperatures. For a given temperature T, the Maxwell–Boltzmann distribution in Equation 3.31 peaks at an electron velocity β_M:

$$\beta_M = \sqrt{\frac{2kT}{m_e c^2}}, \tag{3.36}$$

which yields a peak velocity β_M of 0.05, 0.1 and 0.2 for the temperatures in Figure 3.13. Converting the simulation output SEDs back to photon flux using Equation 3.35, these results can be compared to the semi-analytical results for fixed electron velocities in Figure 3.11. It should be noted how the depth of the absorption line is strictly decreasing with increasing electron velocity and temperature, even though the observed photon flux at 0.5 keV reaches its lowest value for the highest temperature in Figure 3.13. However, the depth of an absorption line is measured relative to the surrounding continuum, which has decreased dramatically at higher temperatures, by photons scattering out of the 0.3–0.7 keV range. The observed absorption feature changes only little with the electron temperature, and is mainly dominated by the electron column density N_e, as discussed above.

Overall, the two different approaches to Doppler–smeared spectra reach an acceptable level of agreement, with the simulated continua in Figure 3.13 somewhat more spread out by scattering. This is mainly caused by the inclusion of multiple scattering in *SKIRT*, with consecutive Doppler shifts for each scattering event. We have access to the population of each scattering level, as shown in Figure 3.14. At this high column density, most photons scatter more than once. Single Doppler–shifts can barely spread out the absorption feature, and the total scattered flux component, which is a flat curve (see bottom panel Figure 3.12), is dominated by multiple scattering. For more than three scattering events, the flux spectrum has no memory of an absorption line and is essentially flat. For energies outside of the 0.3–0.7 keV range, high scattering levels are needed to produce such large total Doppler shifts, and the level populations are inverted. Even more with the inclusion of multiple scattering, one can see that Thomson scattering on a plasma of relativistic electrons provides

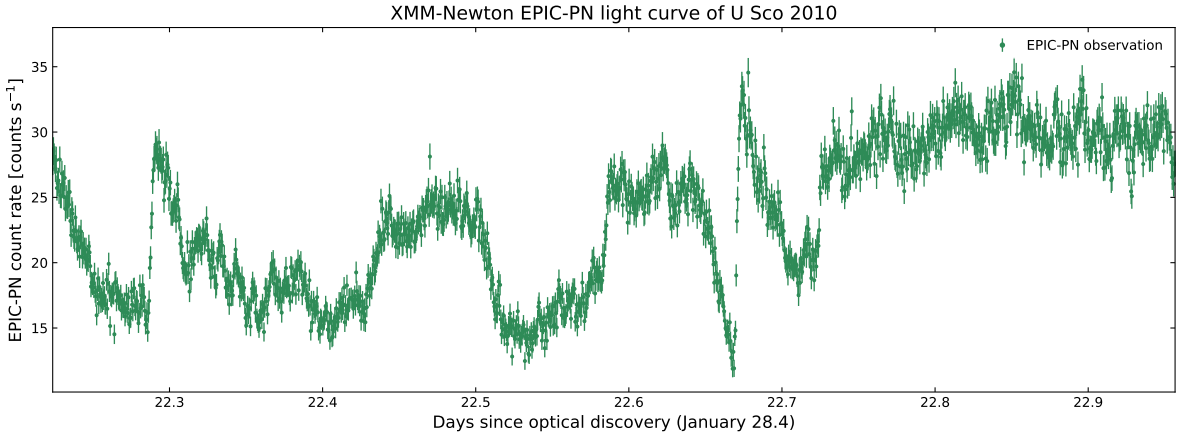

Figure 3.15: *EPIC–PN* light curve of U Sco 2010, 22 days after optical discovery.

a plausible explanation for the absence of atmospheric absorption features in nova spectra, which are blurred out by reflection on the accretion disk corona. In the next section, additional evidence for such corona from the X–ray light curves will be discussed.

3.4 Light curve modelling

The *EPIC–PN* soft X–ray light curve for the first *XMM–Newton* observation of U Sco 2010 is shown in Figure 3.15, with 63.8 ks of exposure time, which covers the ephemeris for the primary eclipse. We focus on the *EPIC–PN* data only, as the *EPIC–MOS* instrument, which tracks the same evolution, is about five times less sensitive. The observed light curve is highly variable between two fixed flux levels, at a count rate about 15 counts s^{-1} and 30 counts s^{-1}, respectively. Four clear dips can be distinguished, as well as one flare–like event centred on day 22.67. Simultaneously, the *Optical Monitor* on board of *XMM–Newton* observed a single clean eclipse in the UV and optical light curves, without any additional dips. The X–ray light curves of U Sco 2010 have been studied thoroughly before, and are discussed in the literature by Ness et al. (2012). In this section, their established light curve model will be reproduced, in order to evaluate the science output of the *DaRT* code.

The Ness et al. (2012) light curve model assumes a central white dwarf photosphere, which contributes to the soft X–ray flux for about 14.5 counts s^{-1} when observed directly (i.e. unobscured). This direct SSS–emission is sequentially occulted by the companion star at day 22.38, and by three obscuring bodies at day 22.27, 22.54 and 22.69. Ness et al. (2012) proposed that the X–ray obscuration in U Sco was caused by cold (i.e. non–ionised) hydrogen–rich material from the companion star, which is fully opaque to soft X–rays and transparent to UV and optical emission. This material could originate from a fragmented accretion stream, which suggests ongoing reformation of the disk around the white dwarf primary. During the X–ray dips, the direct contribution to the SSS–emission is occulted entirely, and one observes the baseline count rate at 15.0 counts s^{-1}, which is visible throughout the entire science exposure. This steady contribution was interpreted as radiation originating from further outside (i.e. outside the binary orbit), being central SSS–emission scattered by the

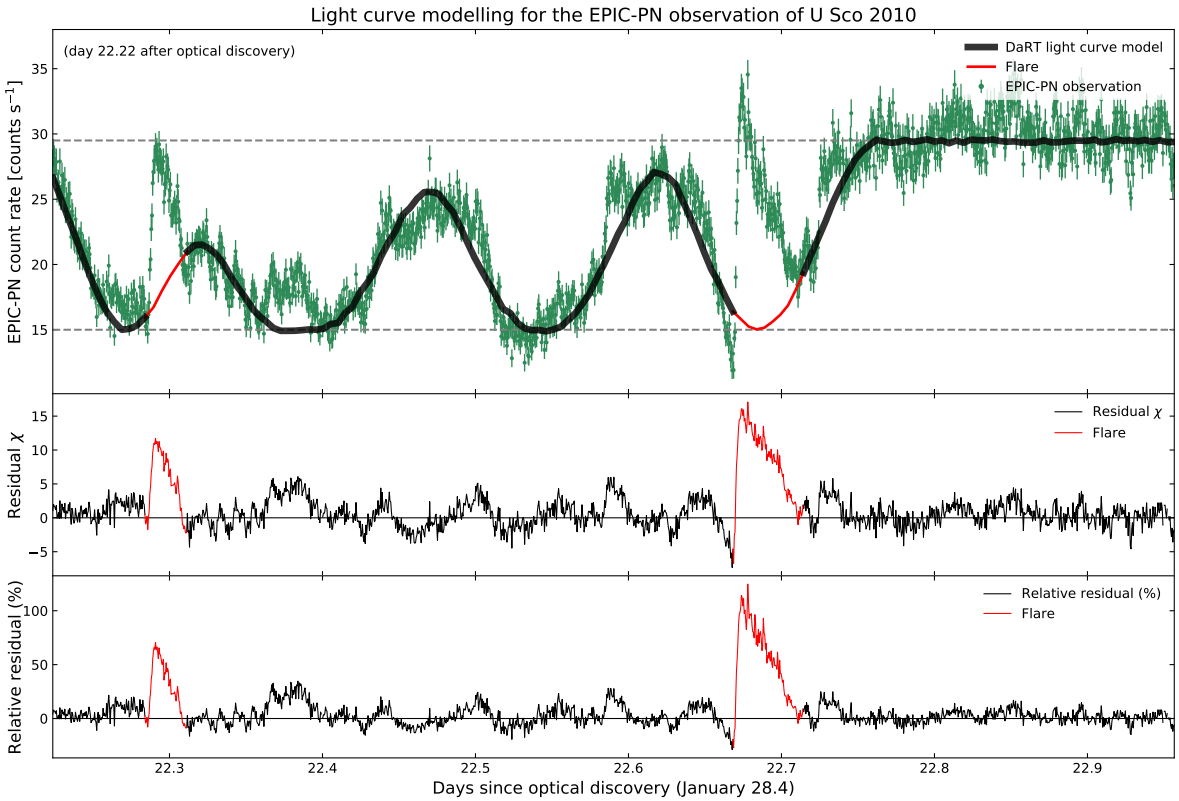

Figure 3.16: *DaRT* light curve model for Nova U Sco 2010, observed with the *XMM–Newton EPIC–PN* instrument on day 22.22 after optical discovery.

accretion disk corona, as discussed in the previous section. The intrinsic flare at day 22.67, which is also present in the optical, UV and hardness light curves, was not included in this light curve model.

The observed X–ray light curve is easily reproduced by introducing four spherical bodies in orbit around a compact central source, with system parameters (i.e. the orbital separation and the component radii) similar to those found by Ness et al. (2012). The *DaRT* simulation results are shown in Figure 3.16, and match the observational *EPIC–PN* data reasonably well, especially considering the simplicity of the proposed light curve model. If one excludes the flare at day 22.67 and a possible second flare at day 22.30, the residuals of the simulation results are consistent with the variability as observed during the high flux state after day 22.77. This geometric light curve model serves as a proof of concept for the hypothesis that the soft X–ray emission extends beyond the binary orbit, and could contribute significantly after scattering on an accretion disk corona. The *DaRT* code is able to reproduce the science results from Ness et al. (2012), and further offers the interface to test the observational implications of more complex light curve models, if they would be proposed at some time. In the next chapters, more intricate light curve models will be discussed, including asymmetric occulter geometries and non–spherical orbits.

Chapter 4

V5116 Sgr 2005

4.1 Introduction

The classical nova V5116 Sgr was discovered by W. Liller on July 4th 2005, at an optical magnitude $\lesssim 8.0$ (Liller, 2005). It was the second nova detection of 2005 in the constellation of Sagittarius, hence it's alternative name of *Nova Sgr 2005b*. With no record of any previous activity in V5116 Sgr, the system was not known as a cataclysmic variable before its 2005 eruption, and consequently, no pre–outburst optical monitoring is available. The field was last observed in quiescence on June 12th, with frequent amateur observations starting only after the optical discovery on July 4.05. However, on July 5.09 the system was observed at a peak magnitude of 7.2, which suggests that the optical discovery was close to the actual outburst, as the optical emission was still rising towards its peak luminosity (Liller, 2005). Later observations did all sample the fading optical light curve as shown in Figure 4.1 (Waagen et al., 2005). Hachisu & Kato (2007) extrapolated this light curve to a nova outburst on JD 2453552.0 (i.e. July 1.5). The nova eruption was confirmed by optical and IR spectroscopy, with expansion velocities for the ejecta between 1300 and 2200 km s^{-1}, as derived from various P–Cygni profiles and emission line widths (Liller, 2005; Russell et al., 2005). Attempts to identify the progenitor system from archival data failed by the presence of a 15–magnitude star close to the nova position, that was too far off to be V5116 Sgr in quiescence, and too bright to reveal the fainter stars nearby (Gilmore & Kilmartin, 2005).

The IR and optical light curves of classical novae follow a universal decline law after rescaling them by a time parameter, which depends mostly on the white dwarf mass and slightly on its composition. From the fading AAVSO optical light curve as shown in Figure 4.1, Hachisu & Kato (2007) could estimate a mass for the white dwarf primary of 0.9 ± 0.1 $M_{\odot}$. This value was later updated to a white dwarf mass of 1.07 ± 0.07 $M_{\odot}$, and the distance towards V5116 Sgr was determined from the absolute magnitude in the theoretical light curve model as 12 ± 1 kpc (Hachisu & Kato, 2010). In 13 observation runs between August and October 2006, 1256 unfiltered photometric measurements were obtained for V5116 Sgr, to study the presence of superhumps in this nova remnant (Dobrotka et al., 2008). Superhumps are periodic brightness variations observed in interacting binaries, caused

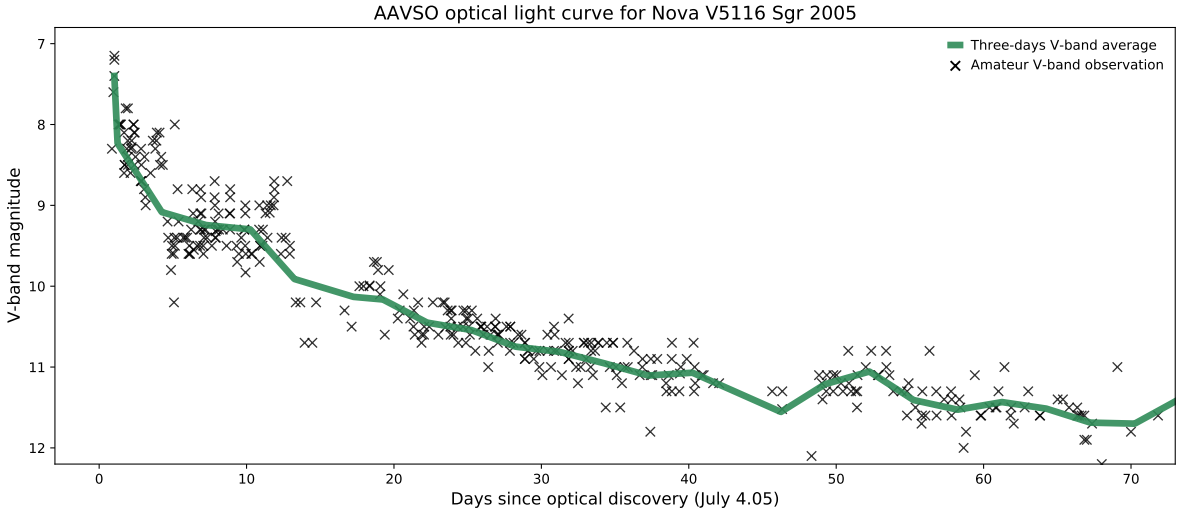

Figure 4.1: Optical monitoring of V5116 Sgr throughout the 2005 eruption, with 375 magnitude measurement from the AAVSO–database within the first 70 days after optical discovery.

by a resonance between a precessing accretion disk and the orbital period. They are expected in cataclysmic variables with a mass ratio $q_2 < 0.35 \pm 0.02$ (i.e. $M_2 \ll M_{\rm WD}$), and have a period slightly above or below the orbital period, depending on retrograde or prograde precession (Patterson et al., 2005). Superhumps trace the presence of a reformed accretion disk, which was destroyed by the initial blast of the nova outburst (Drake & Orlando, 2010). A 0.1238 ± 0.0001 days (i.e. 2.97 hours) modulation was found in the photometric data of V5116 Sgr, which was interpreted as the orbital period in a high inclination system, with the ephemeris for the primary eclipse at:

$$\mathrm{E_{eclipse}} = 2453978.0726 + \mathrm{N} \cdot 0.1238 \text{ days}, \tag{4.1}$$

with N the number of cycles since the eclipsing minimum at JD 2453978.0726 ± 0.0009 (Dobrotka et al., 2008). No superhumps were detected, and from the empirical mass–period relation for cataclysmic variables, a secondary mass of 0.26 ± 0.05 $\mathrm{M_\odot}$ was estimated (Smith & Dhillon, 1998).

As the *Swift* gamma–ray burst mission was only just operational in 2005, no extensive X–ray monitoring campaign was set up to track the evolution of V5116 Sgr in soft X–rays. Instead, a single pointed *XRT* observation was obtained on day 56.7 after optical discovery, with 3.1 ks of exposure time. *Swift* did only detect a marginal X–ray signal above the background level, with a count rate of $(1.2 \pm 1.0) \cdot 10^{-3}$ counts $\mathrm{s^{-1}}$ (Ness et al., 2007a). No follow–up observations were requested, and V5116 Sgr 2005 was about to go down as a rather uninteresting classical nova.

4.2 SSS light curves

In August 2007, *Swift* observed V5116 Sgr again for 3.4 ks of exposure time, to verify the nova turn–off and to look for shocks within the ISM. Rather unexpected, the system was detected as a luminous source at SSS–energies, as late as 765 days after optical discovery. Two additional *Swift* observations

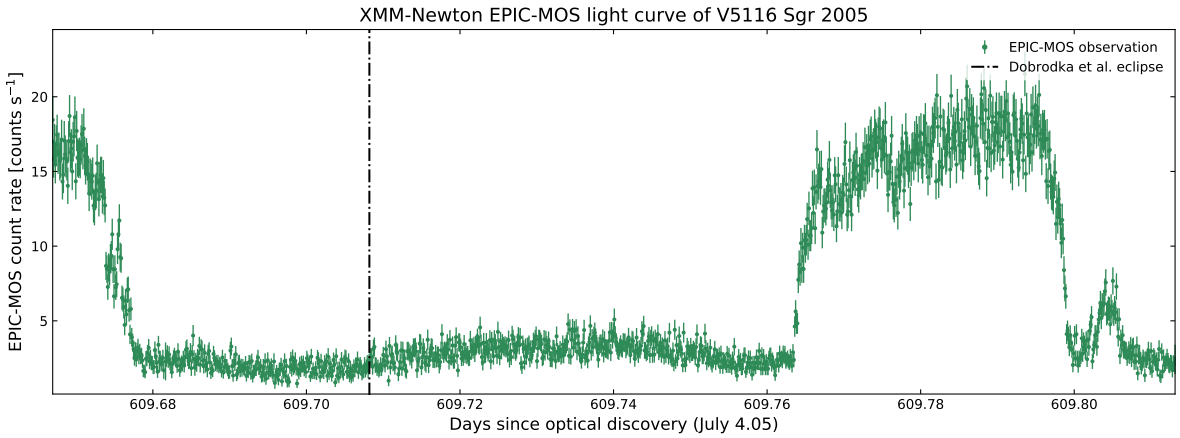

Figure 4.2: *EPIC–MOS* light curve of V5116 Sgr 2005, 609 days after optical discovery.

confirmed the discovery of a SSS–phase in V5116 Sgr, and implied ongoing residual H–burning on top of the white dwarf surface. The soft X–ray flux was detected at 0.56 ± 0.1 counts s^{-1}, with the *XRT* spectra showing an atmospheric SSS–continuum, resembling a blackbody curve of effective temperature $T \approx 450$ kK (Ness et al., 2007b). As target–of–opportunity observations with the *XMM–Newton* X–ray grating observatory were about to be requested, it became apparent that V5116 Sgr had already been observed at SSS–energies six months earlier, as an *XMM–Newton* target included in a larger study on the evolution of galactic classical novae in their post–outburst stages.

V5116 Sgr was observed by *XMM–Newton* on March 5th 2007, for a modest 12.9 ks of exposure time. The system was detected as a bright X–ray source, with a photon flux constrained to soft X–ray energies below 0.7 keV. The *EPIC* CCD spectra were analysed excluding the central pixels affected by pile–up (see subsection 1.2.3), and showed a SSS–continuum of $T = 610 \pm 60$ kK (Sala et al., 2007). Even more interesting were the X–ray light curves obtained in this observation, 609 days after the optical discovery of the nova outburst. The *EPIC–MOS* soft X–ray light curve (see Figure 4.2) showed a high degree of variability, and although the *XMM–Newton* observation covered only just more than one cycle, a ~ 0.12 days periodicity could be recognised, which is consistent with the orbital period of $P = 0.1238$ days as suggested by Dobrotka et al. (2008). During one cycle, the system was found at a low flux state (around 3 counts s^{-1}) for 70% of the time, until the X–ray emission increased abruptly to a high flux state of about 17 counts s^{-1}. Additional substructure could be observed during the low flux state, with a photon flux sequentially increasing and decreasing between 2 and 3.5 counts s^{-1}. The more sensitive *EPIC–PN* instrument observed this same trend with a count rate between 10 and 60 counts s^{-1}, but recorded the light curve for only 9 ks, which does not cover one full cycle. Additional observation time was triggered on Chandra, which observed the system for 35 ks on August 28th 2007, covering three full cycles and confirming the observed periodicity in the soft X–ray light curve (Nelson & Orio, 2007). V5116 Sgr was observed a last time by *Swift* in June 2008, 1065 days after optical discovery. The classical nova was detected at a marginal count rate of $(4 \pm 1) \cdot 10^{-3}$ counts s^{-1}, which indicated that the SSS–phase had ended. In the next section, the enigmatic *EPIC–MOS* soft X–ray light curve will be studied.

4.3 Light curve modelling

4.3.1 Introduction

The soft X–ray light curve of V5116 Sgr was observed to be highly variable 20 months after the optical discovery of the classical nova, with SSS–emission transitioning between a low flux and high flux state, see the *EPIC–MOS* light curve in Figure 4.2. The duration of one such cycle is consistent with the orbital period of $P = 0.1238$ days, hence the temporal variability should be linked to the binary motion in the post–outburst nova system. As the low flux state is observed for 70% of the time in each cycle, the entire light curve cannot be explained by an eclipse of the companion star alone, obscuring the SSS–emission in this high inclination binary longer than half a period. The ephemeris for this primary eclipse is marked on Figure 4.2, as calculated from Equation 4.1. However, with 1512 cycles since the eclipsing minimum on JD 2453978.0726, the absolute error on the orbital period could cause a drift as large as $1.2P$ on this ephemeris. Furthermore, the *Optical Monitor* (*OM*) on board of *XMM–Newton* was operated in the sub–optimal imaging mode, which produced a simultaneous U–band light curve with only five data points and little information on the NUV–emission. We conclude that the ephemeris for the primary eclipse in the *EPIC–MOS* light curve data is not well–constrained.

A detailed analysis of the *EPIC* and *RGS* spectra showed that the spectral shape did not change between the low flux and high flux states, i.e. a similar white dwarf atmosphere temperature and constant hardness ratio was detected throughout the observation, with only the normalisation changing by a factor of six (Sala et al., 2007, 2008, 2010, 2017). Consequently, one could rule out intrinsic variations in the residual hydrogen burning as origin of the observed flux changes. The low flux spectra showed some additional emission lines, which were not visible during the high flux states (Sala et al., 2017). However, this line component could be present throughout the entire observation, but outshined by the high flux SSS–continuum emission. The presence of emission lines in SSS atmospheric white dwarf spectra appears to be a general theme in obscured novae (Ness et al., 2013). Motivated by this spectral evidence, we advocate a model for the observed variability based on the dynamical obscuration of a steady, compact source of SSS-emission.

4.3.2 Asymmetric accretion disk model

We propose a light curve model for the *EPIC–MOS* data as observed by *XMM–Newton*. In this model, we consider a central white dwarf photosphere, bright in supersoft X–rays, which is occulted by both the binary companion and the accretion disk. Around the white dwarf, we introduce a flared accretion disk with an asymmetric rim height, which partially obscures the SSS–emission depending on the viewing angle. This non–uniform rim height is caused by the impact of the accretion stream on the accretion disk, forming a so–called *accretion bulge*: i.e. a local thickening of the disk, becoming less prominent further away from the stream impact at the *hot spot*. The "hot" spot causes additional X–ray emission, although not at SSS–energies, and we just use the hot spot to label the exact location of the stream impact on the accretion disk. As the accretion bulge is always facing the stream of

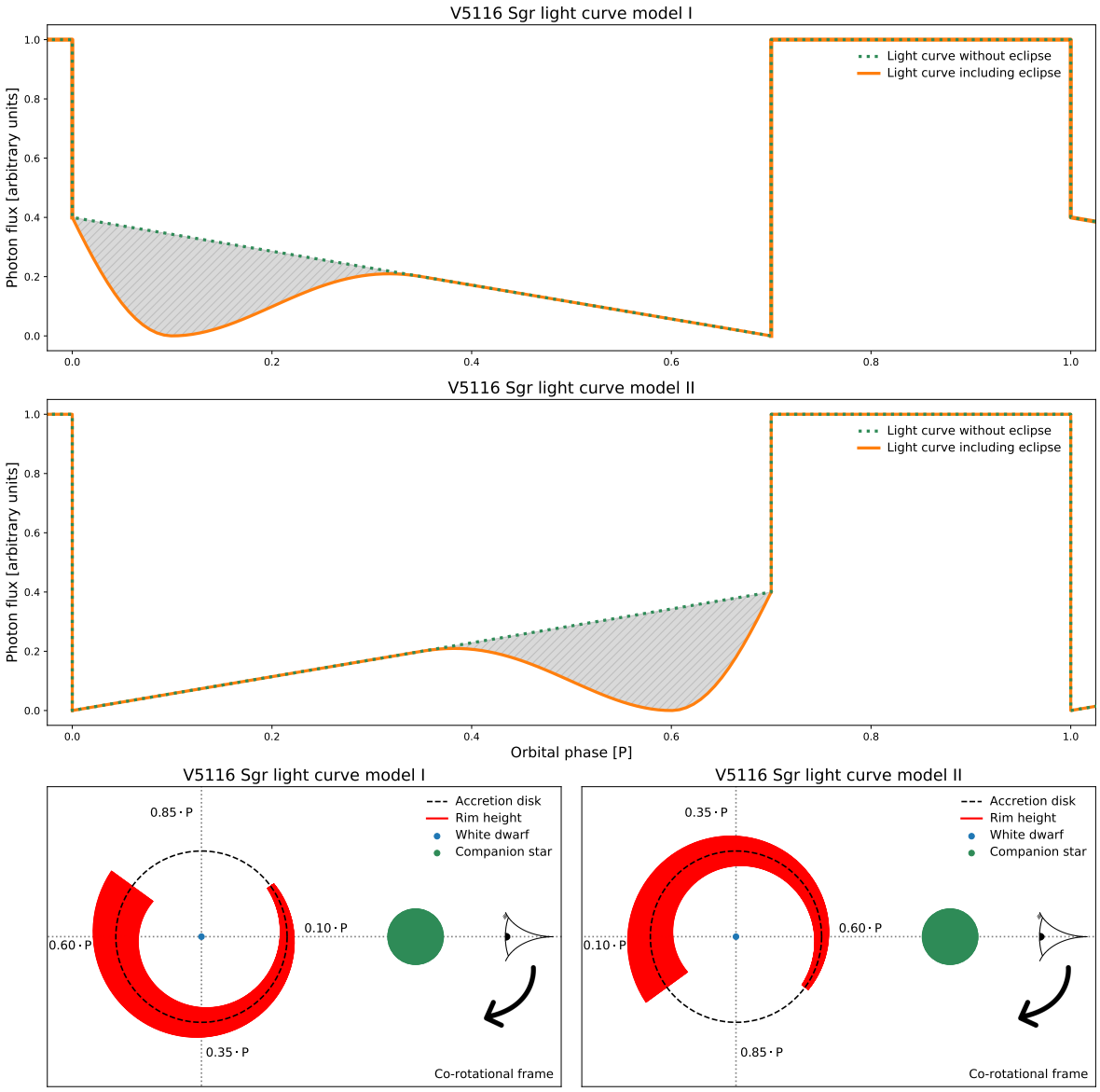

Figure 4.3: Simplified representation of two scenarios for the V5116 Sgr light curve model.

matter provided by Roche–lobe–overflowing companion star, the accretion disk profile is fixed in the co–rotational frame of binary motion. Consequently, the disk rim covering the central photosphere is observed to vary throughout the orbit, causing a dynamical obscuration of the SSS–emission.

Depending on the orientation of the downward slope of the accretion bulge, two scenarios for the V5116 Sgr light curve model are illustrated in Figure 4.3. In model I, the final end of the accretion bulge is observed at phase 0.0, and as the disk rim height increases between phase 0.0 and 0.7, the observed emission decreases. In the bottom panel of Figure 4.3, the disk rim height is represented schematically in red, with the observer moving clockwise in the co–rotational frame (for counter-clockwise binary motion). In model II, the hot spot is observed at phase 0.0, with the accretion bulge decreasing until phase 0.7. The light curve rises, until the primary eclipse is observed at phase 0.6. In each model, one observes the flat disk between phase 0.7 and 1.0, where the obscuration is minimal.

4.3.3 Physical motivation

Although the stellar masses in V5116 Sgr are somewhat uncertain, we stick with the following numbers as discussed in section 4.1: a white dwarf primary mass from Hachisu & Kato (2010) of $M_{\mathrm{WD}} = 1.07 \pm 0.07$ M$_\odot$ (consistent with $M_{\mathrm{WD}} = 1.04 \pm 0.02$ M$_\odot$ from Dobrotka et al. (2008)), and a secondary mass of $M_2 = 0.26 \pm 0.05$ M$_\odot$, calculated from the Smith & Dhillon (1998) mass–period relation (Dobrotka et al., 2008). The orbital period of $P = 0.1238 \pm 0.0001$ days has been determined with high precision by Dobrotka et al. (2008), and using the third law of Kepler (see Equation 2.12), we find the orbital separation:

$$a = 5.3 \cdot 10^{-3} \text{ AU}.$$

From the mass ratios $q_1 = 4.1$ and $q_2 = 0.24$, we can calculate the Roche lobe radii for both stellar components using the Eggleton (1983) Formula 2.21:

$$R_{\mathrm{Roche,\,1}} = 2.7 \cdot 10^{-3} \text{ AU}$$
$$R_{\mathrm{Roche,\,2}} = 1.4 \cdot 10^{-3} \text{ AU}.$$

The companion star fills its Roche lobe, with $R_2 \approx R_{\mathrm{Roche,\,2}} = 1.4 \cdot 10^{-3}$ AU. The compact white dwarf resides within $R_{\mathrm{Roche,\,1}}$, with a white dwarf core radius between $5 \cdot 10^{-5}$ AU and $10 \cdot 10^{-5}$ AU. More important for the light curve model are the extents of the white dwarf photosphere, which is bloated by the radiation pressure from the residual hydrogen burning, and could be over a hundred times larger than the white dwarf core (Ness et al., 2012). Around this photosphere, the accretion disk has reformed. Paczynski (1977) derived an upper limit for the outer extent of this disk, beyond which it gets disrupted by tidal forces. This limit is $\sim 70\%$ of the accretor's Roche lobe radius, and should approximately correspond to the actual outer extent of the accretion disk in case of mass transfer by Roche lobe overflow. We obtain the radius for the white dwarf accretion disk:

$$R_{\mathrm{AD}} = 1.9 \cdot 10^{-3} \text{ AU}.$$

From the orbital separation a and the radius of the companion star R_2, the maximal duration of the primary eclipse can be estimated as:

$$\tan\frac{\delta}{2} = \frac{R_2}{a}$$
$$\iff \delta = 29.6^\circ,$$

with $\delta/180^\circ \approx 20\%$ the fraction of one period that is covered by the eclipse. This corresponds roughly to the duration of the grey–shaded eclipses in Figure 4.3. Similar reasoning constrains the inclination of the binary system to $i > 75^\circ$, in order to produce a notable eclipse.

To motivate the complex shape of the proposed accretion disk geometry, we collaborated with people from the *Centre for Mathematical Plasma–Astrophysics*, which is part of *Leuven University*. We set up hydrodynamical simulations of the Roche lobe overflow in V5116 Sgr using their parallelised adaptive mesh refinement *MPI-AMRVAC* code version 2.0 (Xia et al., 2018; Keppens et al.,

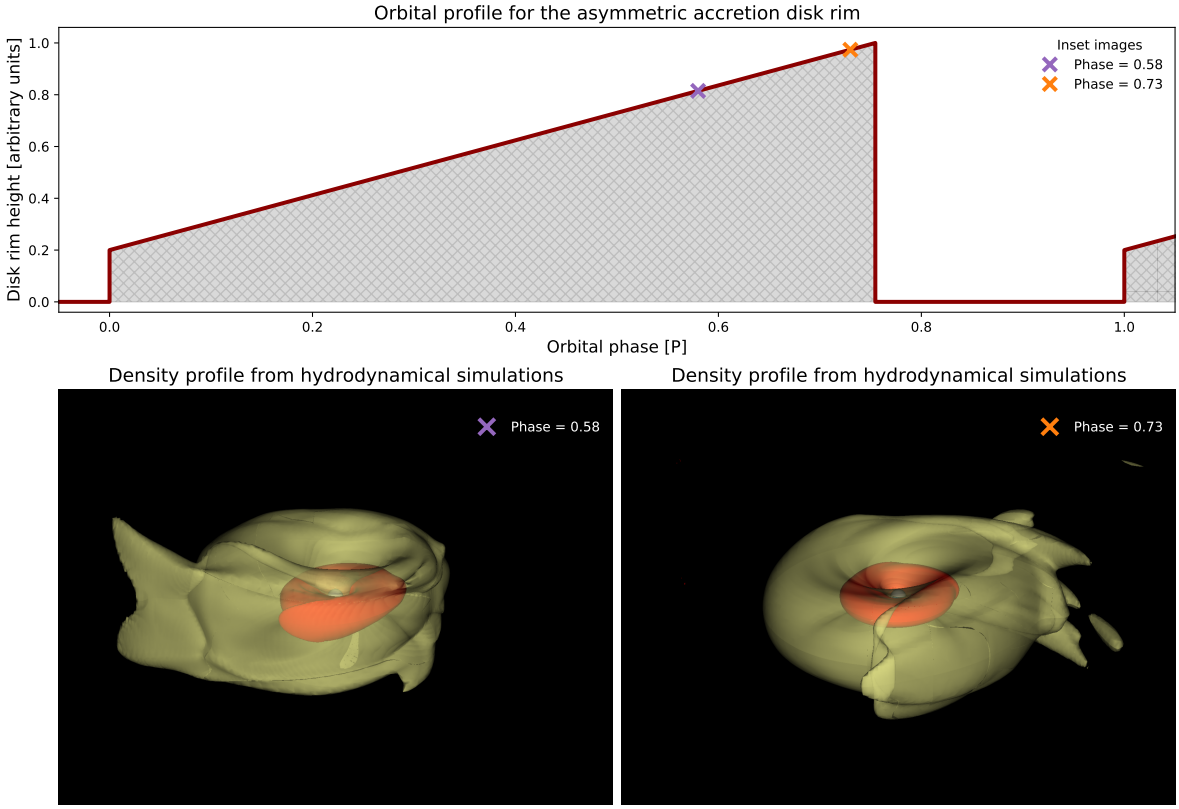

Figure 4.4: (top) Orbital profile for the accretion disk rim corresponding to the model I scenario. (bottom) Hydrodynamical simulations of the Roche lobe overflow in V5116 Sgr.

2003), with system parameters as described above. As the accretion stream impacts the accretion disk from the counterclockwise direction, an asymmetric accretion bulge develops which is consistent with the light curve model I scenario, see the simulated density profiles in the bottom panel of Figure 4.4 (El Mellah, priv. communication, 2020). In the top panel of Figure 4.4, the corresponding orbital profile for the asymmetric accretion disk rim is shown. The maximal rim height can be estimated from the hydrodynamical simulation output as $H_{\rm rim} \approx 4.3 \cdot 10^{-4}$ AU. Note how one could use the full density distribution as obtained in these hydrodynamical simulations directly as the disk geometry. However, as we did not study how different material properties and assumptions for the thermodynamics affect the obtained disk geometry, we will just approach these simulation results as a qualitative test of our proposed light curve model.

The model I disk configuration requires a primary eclipse centred on phase ~ 0.1 (see Figure 4.3). And although we argued that the primary ephemeris is not well–constrained in the *EPIC–MOS* light curve, this placement is actually supported by the sparse amount of observational data. First, the primary ephemeris from Dobrotka et al. (2008) is as close as $0.15P$ (see Figure 4.2), even though it might have drifted as much as $1.1P$. Second, the *OM* U–band light curve, which was obtained simultaneously with *XMM–Newton* but only contained five data points, shows a small dip around phase 0.6 (Sala et al., 2008). We interpret this as the secondary eclipse, supported by observations which showed that the optical emission is dominated by the companion star, irradiated by the SSS–

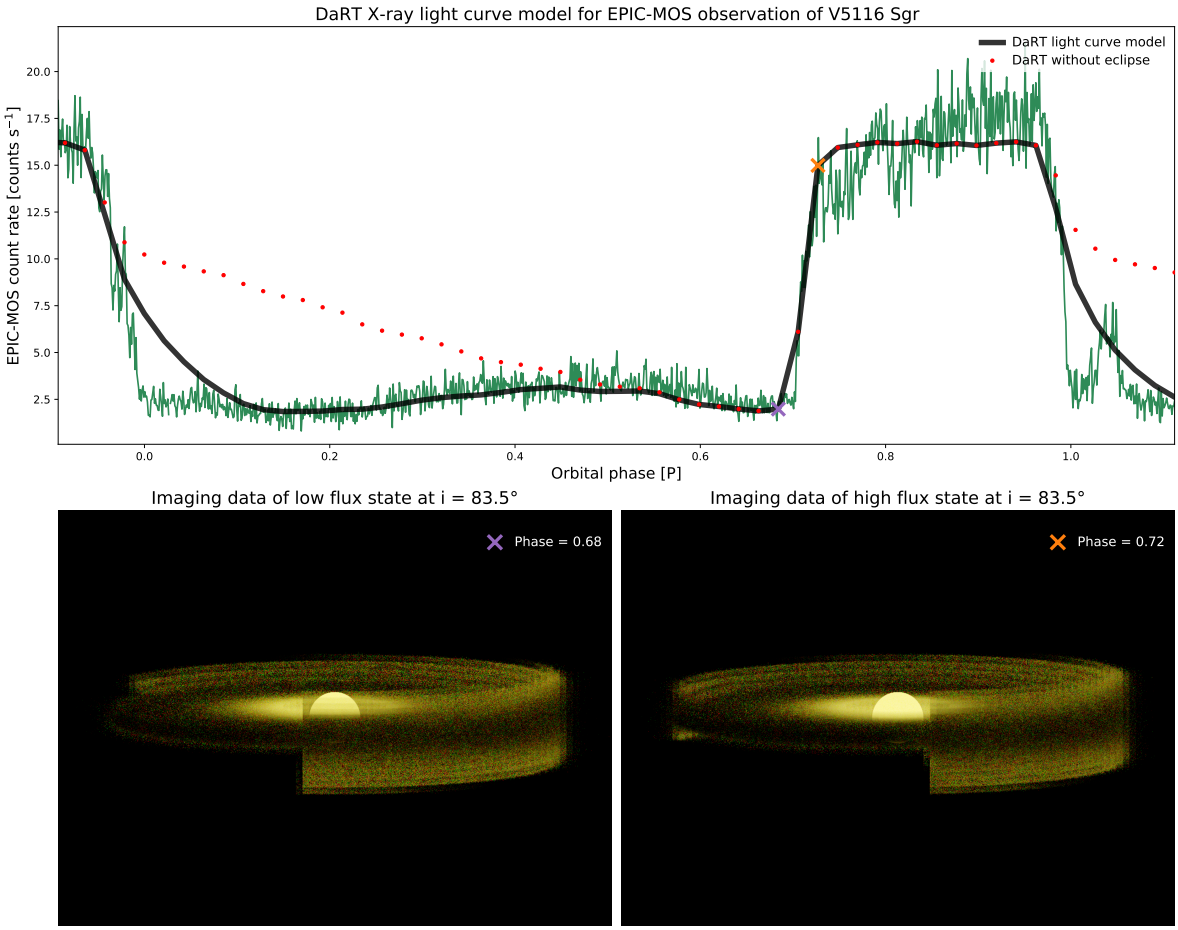

Figure 4.5: *DaRT* simulation results for the two–parameter disk light curve model for V5116 Sgr.

emission from the white dwarf photosphere (Dobrotka et al., 2008). This placement of the secondary eclipse further evidences a primary eclipse at phase ~ 0.1, as required for the model I scenario.

4.3.4 Simulation results

To test the proposed light curve model for V5116 Sgr against observational data, *DaRT* simulations were set up as described in section 2.4. An asymmetric flared accretion disk was introduced to these *DaRT* simulations as a *.fits* data cube, with the following parameterisation for the disk rim height: a first parameter H_0 for the rim fraction at phase zero, and a second parameter P_1 for the phase of the hot spot, where the rim fraction equals unity (see the orbital rim profile in the top panel of Figure 4.4). The absolute dimensions for the accretion disk (i.e. the disk outer radius and the maximal rim height) were obtained in the previous subsection. The disk geometry is centred on the white dwarf primary, and throughout the binary motion, the hot spot will maintain a fixed orientation with respect to the companion star, as shown in the bottom left panel of Figure 4.3. To this end, both the position and position angle of the accretion disk component are updated at each time step in the *DaRT* simulation.

In the previous subsection, we discussed how the size of the white dwarf photosphere is not well–constrained during the SSS–phase. In addition, we face a degeneracy between the white dwarf

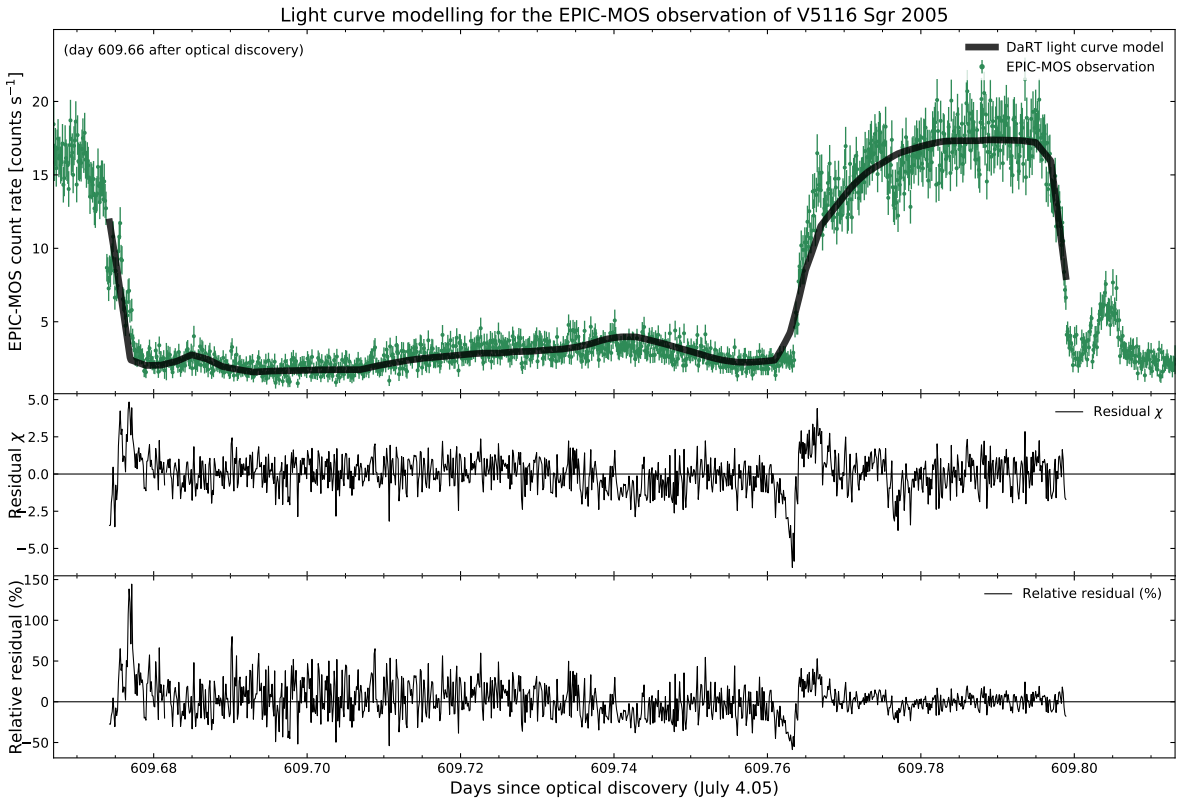

Figure 4.6: *DaRT* light curve model for Nova V5116 Sgr 2005, observed with the *XMM–Newton EPIC–MOS* instrument on day 609.66 after optical discovery.

photospheric radius and the inclination of the binary system while modelling the observed light curve. We fix the photospheric radius at $R_{\mathrm{WD}} = 2.2 \cdot 10^{-4}$ AU for $i = 83.5°$, but we keep in mind that the same simulation results can be obtained at higher inclinations, after rescaling the white dwarf photosphere to the corresponding larger radii. This fixed value for the white dwarf photospheric radius is close to the typical white dwarf core size, which could be expected late in the SSS–phase. Two different types of instruments were added to the simulation setup, to provide *EPIC–MOS*–like SEDs, and resolved imaging data offering a unique view on the V5116 Sgr configuration.

The *DaRT* simulation results for the two–parameter accretion disk light curve model are shown in the top panel of Figure 4.5, both with and without the sinusoidal eclipse centred on phase 0.14. The best–fit configuration for the V5116 Sgr system corresponds to a rim height of $H_0 \cdot H_{\mathrm{rim}} = 0.65 \cdot 4.3 \cdot 10^{-4}$ AU $= 2.8 \cdot 10^{-4}$ AU at phase zero, and a hot spot at phase $P_1 = 0.73$, see the orbital rim profile in the top panel of Figure 4.4. This pair of parameters was found as the result of an extensive *DaRT* grid search in conjunction with a chi–square optimisation routine. Throughout these *DaRT* simulations, the dynamic transfer media were hierarchically gridded by *SKIRT*, with a minimal and maximal octree subdivision level of 4 and 7, respectively, which provided an optimal balance between resolution and computational runtime (see the V5116 Sgr imaging data in the bottom panel of Figure 4.5). For each time in the *DaRT* time grid, *SKIRT* MCRT simulations were performed in the time–frozen configuration, with $N_{pp} = 10^6$ photon packages.

The resulting *DaRT* light curve in the top panel of Figure 4.5 reproduces the *EPIC–MOS* observational data reasonably well, especially for a disk model which was parameterised by just two parameters. We still had difficulties reproducing the sharp decrease and increase in the soft X–ray light curve, while the flare–like bump at phase 1.05 and the additional substructure in the high flux state were not included in our model. We may conclude that this *DaRT* model serves as a proof of concept for our asymmetric accretion disk light curve model for V5116 Sgr as proposed in subsection 4.3.2. With the flexibility of importing any data cube geometry into the *DaRT* light curve simulation, we can arbitrarily fine–tune this asymmetric accretion disk model in order to obtain an arbitrarily close fit to the observational data, e.g. see the simulation results for a disk rim profile defined by seven rim heights along the disk in Figure 4.6. Note how it would be straightforward to add the Roche lobe geometry for the companion star as an additional *.fits* data cube, see chapter 6.

4.3.5 Conclusions

We deciphered the enigmatic *EPIC–MOS* soft X–ray light curve of V5116 Sgr, which was observed 20 months after the optical discovery of the classical nova in 2005. For this, we proposed a model based on a central white dwarf photosphere, which was dynamically obscured by both the companion star and the accretion disk in a high inclination binary. The V5116 Sgr system allows us to learn about disk reformation in classical novae. While it is believed that the accretion disk is destroyed by the initial blast of the nova outburst, it is uncertain how quickly it will reform (Drake & Orlando, 2010). The absence of superhumps in the Dobrotka et al. (2008) optical photometry, which were expected at this mass ratio of $q_2 = 0.24$ (see section 4.1), suggests that the accretion disk reformed between 15 and 20 months after the optical discovery of the nova outburst. Furthermore, V5116 Sgr offers the opportunity to study the spectra of both obscured and direct SSS–novae (i.e. *SSe* and *SSa* spectra, with emission and absorption features, respectively, see Ness et al. (2013)) in the same system, all within one period of three hours.

Chapter 5

V3890 Sgr 2019

5.1 Introduction

V3890 Sgr is a recurrent nova system in the constellation of Sagittarius, with recorded outbursts in 1962, 1990 and 2019, suggesting a recurrence timescale of about 29 years. It is one of the ten RNe in our galaxy, and it has a red giant secondary which classifies V3890 Sgr as a symbiotic nova (Harrison et al., 1993). In symbiotic binaries, the red giant stellar wind forms a circumstellar nebula, and during quiescence one observes absorption features from both the red giant and the nebula, plus nebular emission lines excited by the hot white dwarf (Bryan & Kwok, 1991). In the folded light curve for V3890 Sgr, which was constructed from all available optical and IR photometry, shallow eclipses were detected, with the ephemeris for the primary minimum at a Julian Date (Schaefer, 2009):

$$\mathrm{E_{eclipse}} = 2454730 + \mathrm{N} \cdot 519.7 \text{ days}. \tag{5.1}$$

An additional 103.8 ± 0.4 days modulation was found in the J–band photometric data, associated with the typical pulsations in red giant stars (Schaefer, 2009; Fraser et al., 2008). Optical light curve modelling of the 1990 outburst obtained a white dwarf mass of $\sim$1.35 $\mathrm{M_\odot}$ (Hachisu & Kato, 2001).

With an orbital period of 519.7 ± 0.3 days, it has been doubted whether the companion star could fill its critical Roche lobe at $\mathrm{R_{Roche}} \approx 126$ $\mathrm{R_\odot}$ (see Equation 2.21), to enable mass transfer by Roche lobe overflow. A wind accretion model has been proposed, with a Roche lobe underfilling red giant losing mass in a dense stellar wind, which is then partly captured by the white dwarf primary (Hachisu & Kato, 2001; Dobrzycka et al., 1996). Wind capture could be the only way to explain mass transfer in symbiotic novae, in the case that the companion does not fill its Roche lobe. However, given the typical mass loss rate for M-type red giants, the stellar wind fails to provide hydrogen at the extreme accretion rates $\gtrsim 10^{-7}$ $\mathrm{M_\odot}$ $\mathrm{yr^{-1}}$, as needed for the short recurrence timescales in RNe, and the wind accretion model breaks down by many orders of magnitude (Schaefer, 2009; Hachisu & Kato, 2001). In symbiotic novae, accretion thus proceeds by Roche lobe overflow, with the whole system being embedded in an envelope of red giant stellar wind. The companion star needs to have a mass $M_2 \lesssim 1.1$ $\mathrm{M_\odot}$ in order to avoid accretion instabilities, causing common envelope evolution and the associated spiral–in of the symbiotic binary (Frank et al., 2002). Assuming a Roche lobe filling red

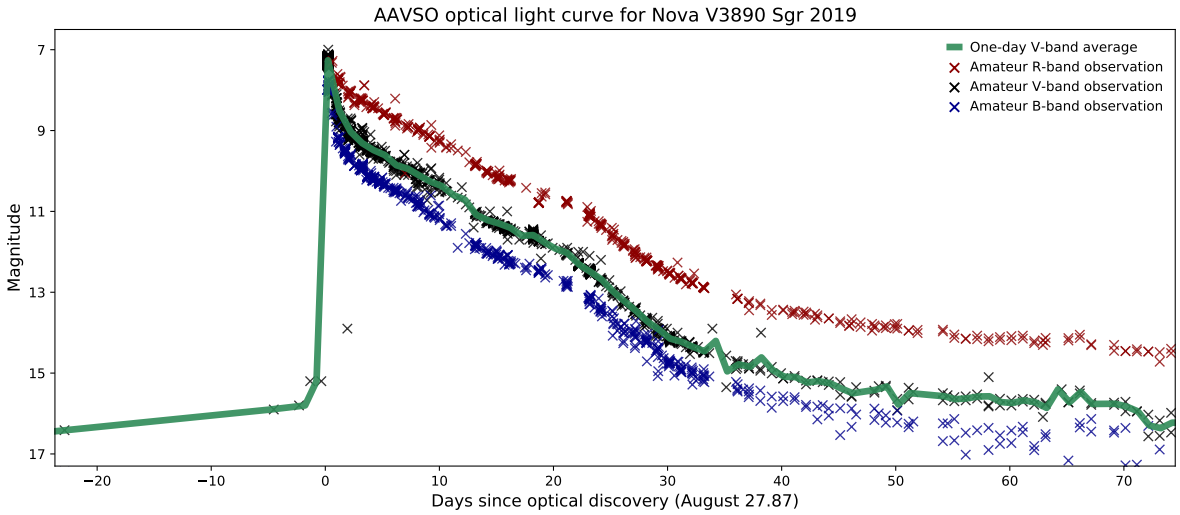

Figure 5.1: Optical monitoring of V3890 Sgr throughout the 2019 eruption, with over 4500 magnitude measurement from the AAVSO–database within the first 75 days after outburst.

giant, the flux distance towards V3890 Sgr can be obtained as 7 ± 1.6 kpc, which places V3890 Sgr inside the galactic bulge (Schaefer, 2010a). A reliable *Gaia* distance has not been obtained yet, as more data is needed to correct the measured parallaxes for binary motion (Schaefer, 2018).

The 2019 outburst of V3890 Sgr was discovered by A. Pereira on August 27th. Within three hours, the outburst was confirmed from optical spectroscopy, with broad P Cygni profiles indicating expansion velocities well above 4200 km s^{-1} (Strader et al., 2019). With a last pre–outburst observation by R. Stubbings on August 27.52, and a saturated data point in the ASAS-SN survey covering this field five hours later, the 2019 outburst is constrained to a Julian date of 2458723.15 ± 0.1, i.e. August 27.65. During the first 75 days after discovery, the optical light curve was frequently sampled by amateur observations, see the AAVSO light curve in Figure 5.1. With measurements in three different bands, the colour was observed to evolve from blue at the eruption, to red in the quiescent state, where the emission is dominated by the red giant at an R–band magnitude of 14.3. The expansion velocity of the ejecta was monitored with optical spectroscopy, and a decreasing linewidth for the narrow H_α component showed that the ejecta were slowing down in the red giant stellar wind (Teyssier et al., 2019). Characteristic C–lines were discovered with IR spectroscopy, suggesting a CO–composition for the white dwarf primary and making the system a SNIa progenitor candidate (Evans et al., 2019).

V3890 Sgr was first observed in X–rays with *Swift*, twelve hours after the optical discovery. Significant X–ray emission was discovered straightaway, at a count rate of 1.15 counts s^{-1}, with X–ray photons centred around 3 keV (i.e. hard emission compared to the SSS–range). At a distance of 7 kpc, this hard component traces strong $1.1 \cdot 10^{36}$ erg s^{-1} shocked emission from the expanding ejecta which is colliding with the red giant stellar wind or pre–outburst circumstellar material (Sokolovsky et al., 2019). The collisional origin for these hard X–rays was further evidenced by the detection of synchrotron radiation at radio wavelengths (Pavana et al., 2019). Regular *Swift* X–ray monitoring in the 0.3–10.0 keV range continued on a daily basis, see the X–ray light curve in Figure 5.2a. During

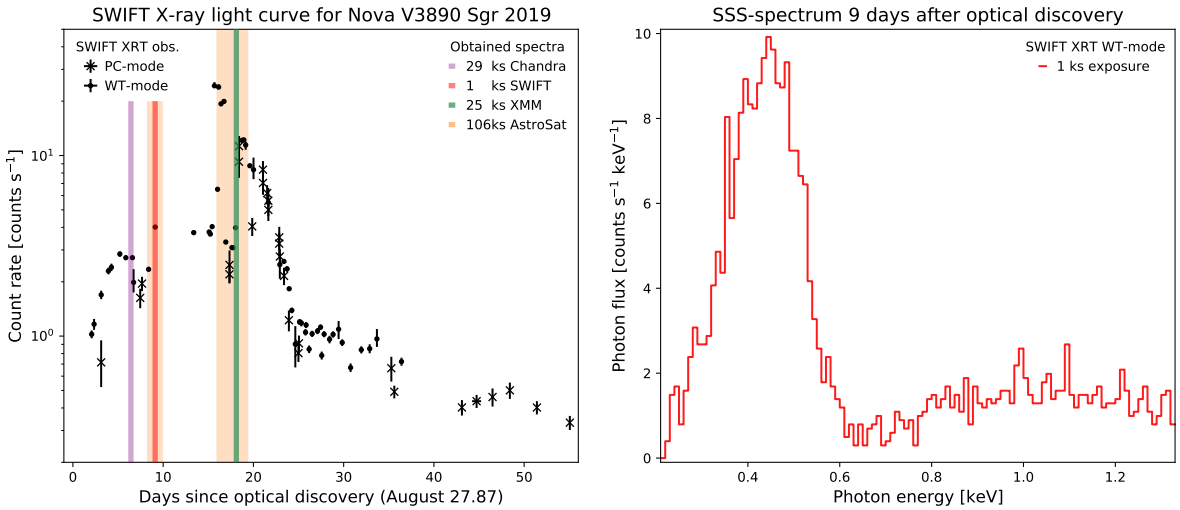

Figure 5.2: (a) *Swift* X–ray monitoring of V3890 Sgr 2019 in the 0.3–10.0 keV range. (b) *Swift XRT* spectrum showing V3890 Sgr as a SSS–continuum, 9 days after optical discovery.

the first six days, the *Swift XRT* spectra shifted towards slightly lower energies, indicating that the collisional plasma was cooling, and the total absorption column decreased by a factor of ten, showing that the ejecta were becoming more transparent while expanding (Page et al., 2019b). On day 7, V3890 Sgr was observed for 29 ks with the High Energy Transmission Grating (HETG) on board of the Chandra X–ray observatory. The high–resolution grating spectrum showed rich emission lines, indicating the presence of a collisional plasma, similar to the observed early X–ray stages of symbiotic novae such as RS Oph (Orio et al., 2019). A detailed spectral analysis revealed collisional ionisation equilibrium radiation associated with two distinct shocks (one at 1 keV and another at 4 keV), or possibly the emission from a complex two–phasic medium of ejecta, having a hot component colliding with the red giant wind, mixed with cold clumpy material (Orio et al., 2020). Various line ratios were measured, which may support the CO–composition of the white dwarf primary.

On day 9 after optical discovery, the *Swift* soft X–ray monitoring detected a significant rise in the count rate at energies below 1 keV, and the low–resolution *XRT* spectra confirmed the start of the SSS–phase for V3890 Sgr, as shown in Figure 5.2b: The SSS–continuum centred on 0.45 keV can be fitted with a white dwarf atmosphere model of effective temperature 720 ± 10 kK, with residual hydrogen–burning exposed on its surface (Page et al., 2019b). At 7 kpc, the total unabsorbed luminosity was calculated to be $7.8 \cdot 10^{36}$ erg s^{-1}. Centred on 1.05 keV, the collisional plasma component is still present, and both spectral components are absorbed with the same column density of $N_H = (3.3 \pm 0.4) \cdot 10^{21}$ cm^{-2} (Page et al., 2019b). The appearance of SSS-emission in V3890 Sgr was fully covered by a long *AstroSat SXT* observation from day 8.1 to day 9.9, which will be discussed in section 5.2. With only 9 days passed since the nova eruption, the supersoft X–ray source in V3890 Sgr was revealed exceptionally early, which could be linked to having a very massive white dwarf primary, as was suggested for the symbiotic nova V745 Sco 2014 which had its SSS-phase starting 4 days after the outburst (Page et al., 2015).

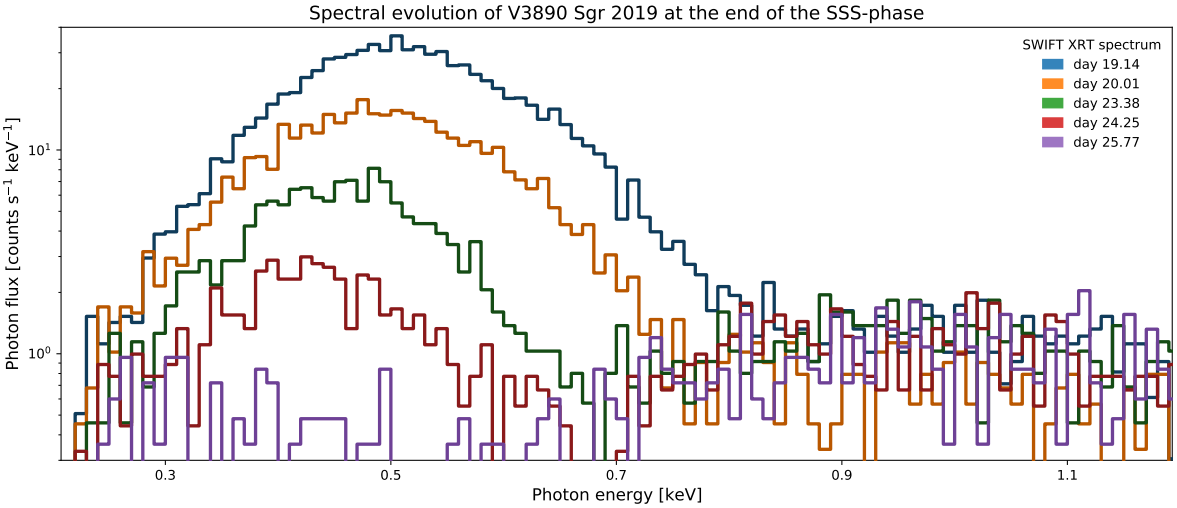

Figure 5.3: *Swift XRT* spectra of V3890 Sgr 2019 during the last seven days of the SSS-phase.

While lunar constraints prohibited further *Swift* monitoring during its rise to maximum SSS-emission, V3890 Sgr was observed with the *NICER* soft X–ray telescope installed on the International Space Station. On day 10, *NICER* observed a SSS-flux which was three times higher than the *Swift* detection on day 9, while also discovering an 83 s modulation in the soft X–ray light curve, originating from the SSS–continuum component (Beardmore et al., 2019b). Short–period oscillations below 1 keV have been detected during the SSS–phase in five more novae, and could be explained by g–mode pulsations in the white dwarf, driven by nuclear burning instabilities (Ness et al., 2015). *Swift* monitoring continued on day 15, and a highly variable soft X–ray state was detected, with a count rate between 3.7 and 26.7 counts s^{-1} (Beardmore et al., 2019a). The variable X–ray flux was confined to the SSS–continuum component, and might reflect the early post–outburst stages of novae, with dynamical obscuration effects from the cold and clumpy ejecta eclipsing the residual hydrogen burning. From day 16 to day 19.5, V3890 Sgr was observed with the *AstroSat* mission, and on day 18 after optical discovery, a continuous 25 ks observation with the *XMM–Newton* X–ray grating observatory was triggered. Both observations are marked on the *Swift* X–ray light curve in Figure 5.2a and will be discussed in the next section.

From day 20 to day 25, a strong decline was observed in the *Swift* light curve, see Figure 5.2a. The low–resolution *XRT* spectra could attribute this decrease in soft X–ray flux to a fading SSS–continuum component, see Figure 5.3. Each of these spectra were extracted from the UK Swift Science Data Centre and have an exposure time of $\sim$ 900 s. Figure 5.3 indicates that the residual hydrogen burning on top of the white dwarf was turned off gradually, and shows that the SSS–phase ended 25 days after optical discovery. Both the high peak temperature (800 kK) and the short duration (16 days) of the SSS-phase suggest a high paced residual hydrogen burning, which is associated with massive white dwarf primaries (Page et al., 2019a; Wolf et al., 2013). On day 25, a small bend could be recognised in the optical light curve (see Figure 5.1), which might indicate that a minor fraction of the soft X–ray radiation was reprocessed and contributed to the optical emission, although without the

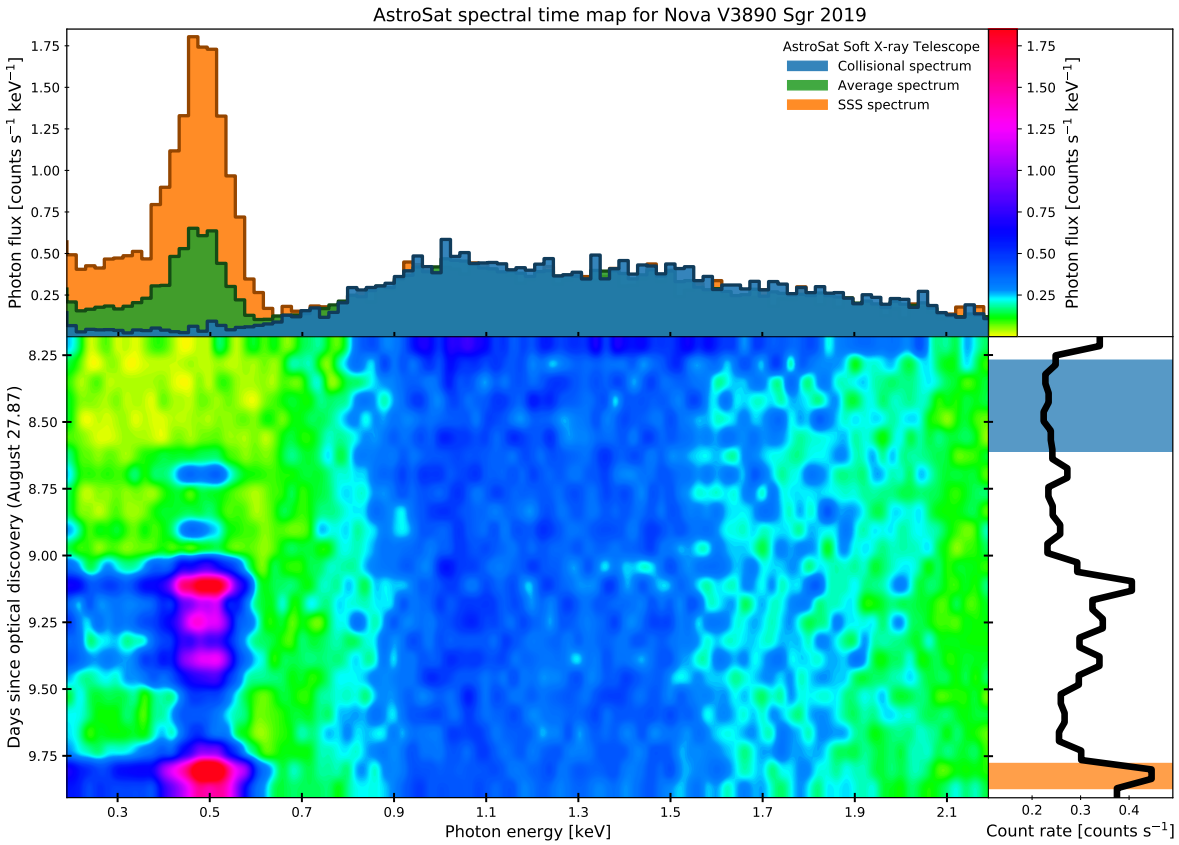

Figure 5.4: Spectral evolution of Nova V3890 Sgr 2019 from day 8.1 to day 9.9 after optical discovery, covering the start of the SSS–phase with the *AstroSat SXT* (data provided by the P.I. K. P. Singh).

formation of a significant optical plateau, as discussed for U Sco 2010 in section 3.1. Once the SSS-emission disappeared, the hard plasma component at $\sim$ 1 keV dominated the *XRT* spectra, as was the case before the SSS-phase. From day 25 on, the collisional plasma continued its gradual cooling, while the total absorption of the system kept reducing by the expansion of the ejecta (Page et al., 2019a). By day 55 after optical discovery, the excessive nova emission had faded in each wavelength regime, and V3890 Sgr returned to its quiescent state.

5.2 Spectral time maps

From day 8.1 to day 9.9, V3890 Sgr was observed with the Soft X–ray Telescope (*SXT*) on board of the multi-wavelength *AstroSat* mission, covering the *Swift* discovery time of SSS-emission on day 9.11. During the X–ray observation, the CCD at the *SXT* focal plane recorded the arrival time and energy of each individual photon to an event file (see subsection 1.2.3), from which X–ray spectra and light curves can be constructed by filtering on energy and time, respectively. However, the wealth of information contained in the event files of longer X–ray observations can also be represented in its entirety as a spectral time map (STM), as shown in Figure 5.4. By visualising the photon flux in the 2D energy–time plane, STMs provide an organised overview of the spectral time evolution

of the observed system. The spectral time map in the bottom left panel of Figure 5.4 shares its x–axis (energy) with the spectra in the top panel, and shares its y–axis (time) with the light curve on the right-hand side. The colour scale for the STM photon flux is provided in the top right corner. The light curve on the right was obtained by integrating the STM over the 0.2–2.2 keV energy range, with time running in the negative y–direction. The top panel contains the time–averaged spectrum for the entire observation (green), and two more spectra extracted before (blue) and after (orange) the appearance of SSS-emission, with times as marked on the light curve.

During the first ten hours, V3890 Sgr was observed at a steady X–ray state, with a photon flux around 0.3 counts s^{-1} and spectra only showing the collisional plasma component above 0.9 keV, see Figure 5.4. On day 8.6 after the optical discovery, small flares appeared in the X–ray light curve, which were confined to photon energies in the 0.4–0.6 keV range, and could be attributed to a first glimpse on the white dwarf, burning residual hydrogen. Strong SSS–emission was observed on day 9.0, which confirmed the *Swift* discovery of the SSS-phase in V3890 Sgr. The atmospheric continuum component was found to be highly variable throughout the early SSS-phase, with substantial flux changes on short timescales. The *SXT* spectra could be fitted with an absorbed blackbody plus *VAPEC* model (i.e. an emission model for collisionally-ionised diffuse gas), yielding a plasma temperature kT in the 2.5–4.0 keV range, and a column density N_H fluctuating between $3.5 \cdot 10^{21}$ cm^{-2} and $7.3 \cdot 10^{21}$ cm^{-2} (Singh et al., 2019). While the intensity of the SSS-continuum emission changed by a factor ten between the high and low flux states, the blackbody temperature remained constant at about 750 kK (Singh et al., 2019). This spectral stability indicates that the SSS-variability is caused by dynamical obscuration of the central soft X–ray source rather than intrinsic changes in the nuclear burning. Cold ejecta moving on highly elliptical trajectories can easily reproduce the observed X–ray light curve, as will be demonstrated in section 5.3. *AstroSat* observed V3890 Sgr again from day 16 to day 19.5, covering the end of the SSS–phase. The Wien tail of the atmospheric continuum was detected at slightly higher energies compared to the first observation, indicating a small rise in the effective temperature. The soft component was still observed to be highly variable, suggesting that the emission never stabilised throughout the SSS–phase.

At the same time, V3890 Sgr was observed with the *XMM–Newton* X–ray grating observatory from day 18.1 to day 18.4, offering the opportunity to study the short–period variability at high–spectral resolution. Figure 5.5 shows the spectral time map for this observation, visualising the evolution of the *RGS1*+*RGS2* merged grating spectra over the 0.425–0.750 keV range. During the 25 ks of *XMM* exposure time, the system was found at a high flux state of about 15 *RGS* counts s^{-1}, until the photon flux dropped to almost zero for $\sim$3.5 ks on day 18.24, as shown in the light curve on the right-hand side. Some smaller dips could be recognised in the second half of the science exposure, and during the first 0.4 ks, the SSS-emission was rising from a lower flux state. In the top panel of Figure 5.5, the high flux (blue) and low flux (orange) *RGS* spectra are shown, extracted during the times as marked on the light curve. The high flux grating spectrum contains the soft X–ray continuum emission, although with much more structure than observed with the *SXT* and *XRT* instruments. The overall spectral shape can be reproduced by an absorbed blackbody continuum of effective tem-

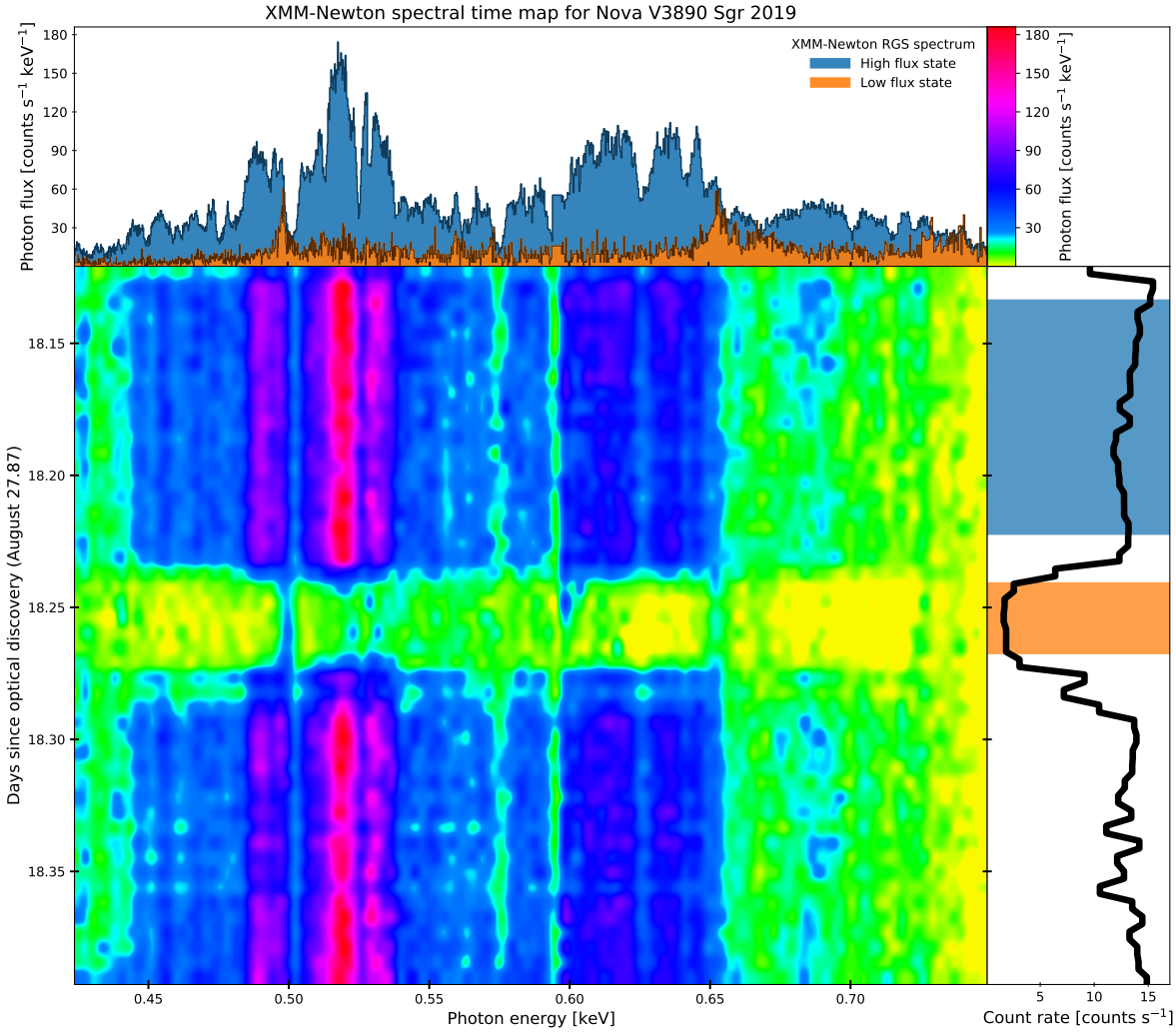

Figure 5.5: Spectral evolution of Nova V3890 Sgr 2019, observed with the *XMM–Newton RGS* on day 18 after optical discovery (data provided by the P.I. J. U. Ness).

perature $T \approx 600$ kK, with strong atmospheric absorption and emission features superimposed (Ness et al., 2019). The spectral structure is dominated by the absorption edges of interstellar OI at 0.54 keV (i.e. the OI K–edge) and local NVII at 0.67 keV. The narrow OI K_α interstellar absorption line can be recognised at 525 eV. On day 18.24, the SSS–continuum emission disappeared over the entire 0.425–0.750 keV range, leaving only the soft part of the shocked plasma spectrum, with collisionally excited emission lines of hydrogen–like NVII Ly_α and OVIII Ly_α at 0.50 keV and 0.65 keV, respectively, as shown in the low flux *RGS* spectrum in the top panel of Figure 5.5. During the low flux state, no residual continuum emission was detected, in contrast to the reflected X–ray component observed during the dips in the light curve of U Sco 2010, with emission originating from a large scattering region around the central soft X–ray source, see section 3.2. No short–period oscillations < 100 s were found in the *XMM* data (and neither in the *Swift* nor *AstroSat* data), and therefore the *NICER* detection of a 83 s modulation at soft X–ray energies was not confirmed (Ness et al., 2019).

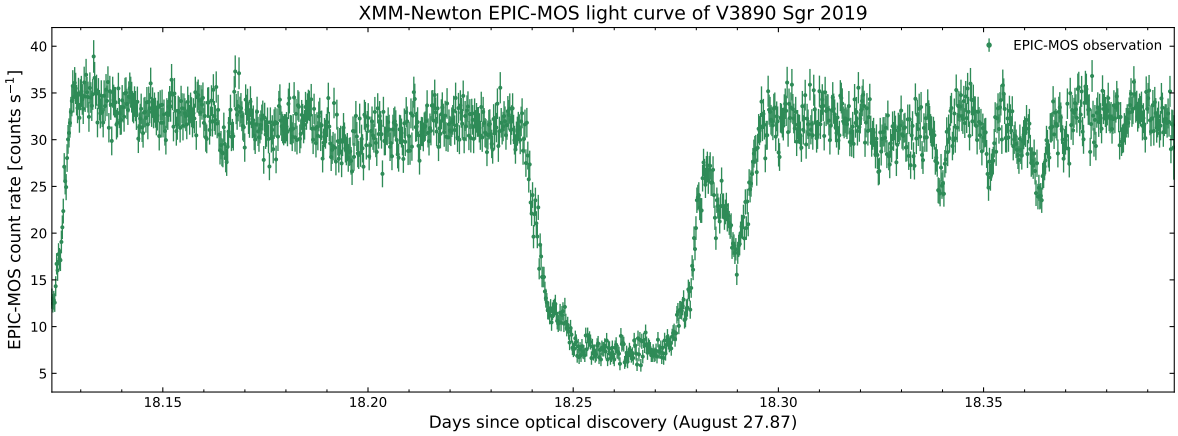

Figure 5.6: *EPIC–MOS* light curve of V3890 Sgr 2019, 18 days after optical discovery.

5.3 Light curve modelling

The recurrent symbiotic nova V3890 Sgr 2019 was observed with *XMM–Newton* for 25 ks during the SSS–phase, on day 18 after optical discovery. In the previous section we discussed the *RGS* grating spectra, and here we focus on the *EPIC* light curves. During the first 7 minutes of exposure time, the *EPIC–MOS* light curve was observed to rise from 12 counts s^{-1} to a stable level around 33 counts s^{-1}, see Figure 5.6. The *EPIC–PN* detector was opened some time later and did not contain this first feature, but further observed the exact same evolution of the count rate. Throughout the pronounced dip centred on day 18.26, the photon flux was detected at a constant rate of 7.48 counts s^{-1}, which was attributed to the collisional line flux in the soft X–ray range during a period of total obscuration of the SSS–continuum emission, see the *RGS* spectral time map in Figure 5.5.

Guided by the observational evidence as presented in the previous section, we propose a light curve model for the *EPIC–MOS* data of V3890 Sgr, based on dynamical obscuration by clumpy ejecta. The SSS–continuum emission is confined to the white dwarf photosphere, and can easily be eclipsed by clumps of cold material, in motion around the white dwarf star, while the collisional emission emerges from a much more extended region and suffers less from local obscuration. In order to reproduce the steep ingress and egress of the central eclipse, highly elliptical trajectories were introduced for the clumpy ejecta. Covering only seven hours of the total 520 days orbital period, the system can be studied in the white dwarf reference frame, neglecting any binary motion.

Starting from a configuration with seven clumps of cold material moving in the gravitational potential of the nuclear–burning white dwarf primary, we performed a grid–search for the system parameters using the *DaRT* code in conjunction with a chi–square optimisation routine. For each component we obtained the extend (radius), together with the eccentricity, radius and orientation of their orbit, and their position at the start of the *XMM–Newton* observation. The observational *EPIC–MOS* data can be reproduced by a model with six small and one larger clump, sequentially obscuring the central source of SSS–emission, plus a base level collisional contribution of 7.48 counts s^{-1}, with results as shown in Figure 5.7. While this basic light curve model faces a high degree of degeneracy,

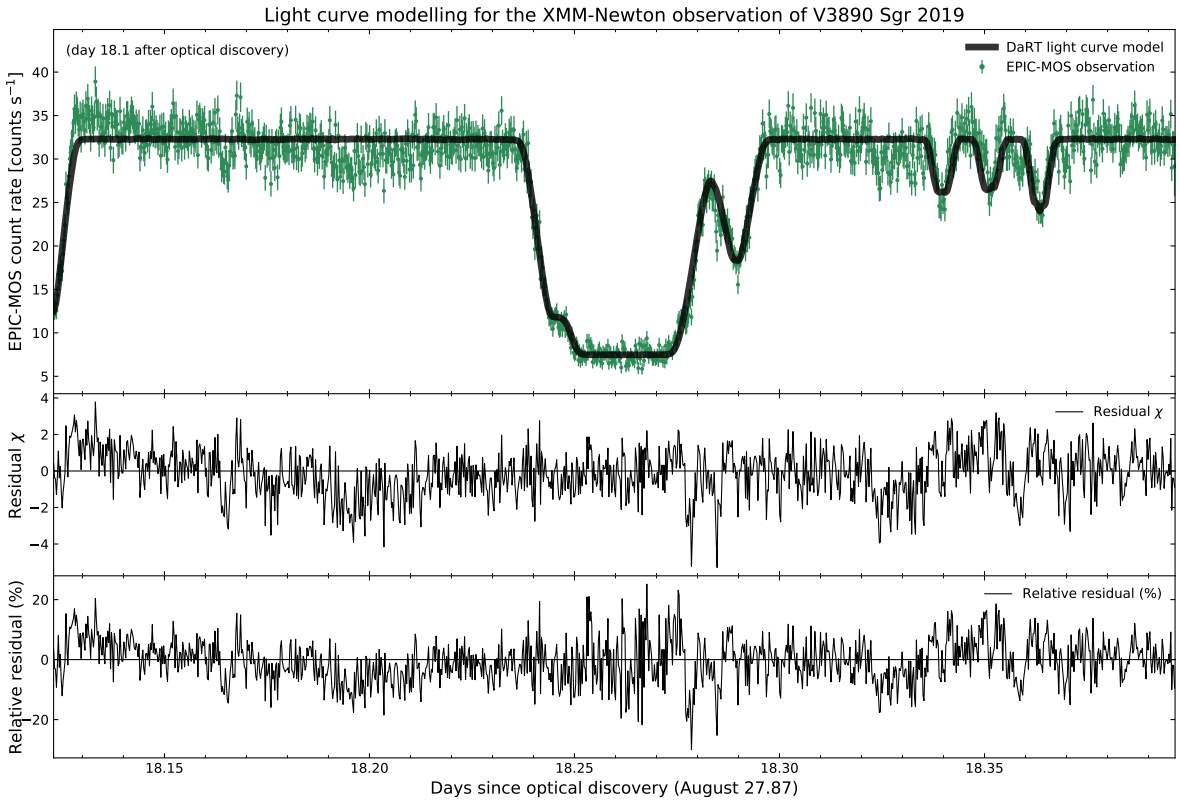

Figure 5.7: *DaRT* light curve model for Nova V3890 Sgr 2019, observed with the *XMM–Newton EPIC–MOS* instrument on day 18.1 after optical discovery.

and does not constrain the clump parameters uniquely, it serves as a proof of concept for the hypothesis of dynamical obscuration effects from clumpy ejecta causing the observed short–period variability in the light curves of novae during their SSS–phase. The model is dynamically self–consistent and its conciseness should be favoured over any more elaborate model without strong physical motivation. However, the *DaRT* code offers all the flexibility to study the more complex models (with advanced transfer media, arbitrary geometries and tabulated kinematics, see section 2.4), and has the potential to reveal the observational implications of any forthcoming light curve model for V3890 Sgr, if it is now or in 29 years from now.

Chapter 6

Conclusions and Prospect

In the previous chapters, we discussed three different novae in great detail, focusing on the supersoft X–ray emission in the final stages of their outburst. We showed how the advanced X–ray observatories *Swift*, *XMM–Newton* and *Chandra* are well–suited to study the SSS–phase of novae: the *Swift* observatory allows for high cadence monitoring of the soft X–ray flux evolution, and guides deeper, continuous observations with the X–ray grating observatories. These grating instruments introduce high–resolution spectroscopy to observational X–ray astronomy, and could identify individual line transitions in the nova spectra. The SSS–spectra of novae show a bright atmospheric continuum, which could be approximated by an absorbed black body spectrum of effective temperature $T_{\rm eff} \approx 500$ kK. While detailed spectral modelling of these atmospheric nova spectra could provide physical information on the photospheric radius, the white dwarf composition and its surface gravity (linked to the white dwarf mass), a lot of work is still needed in this field. Currently, the most reliable approach is based on static white dwarf atmosphere models, with absorption features which are blue–shifted afterwards in order to account for the effects of radiative transfer in the expanding nova environment (Rauch et al., 2010). Efforts in NLTE radiative transfer modelling through an expanding medium, using massive stellar wind codes such as *PHOENIX*, have shown promising results (van Rossum & Ness, 2010). However, little developments were made over the last ten years. Considering these poorly documented, non–publicly available, old codes (the *PHOENIX* X–ray radiative transfer module dates from 2005), the next breakthroughs will most likely involve a fresh start, based on a more modern radiative transfer code. We see potential in future versions of *SKIRT* with full X–ray support, supplemented with ideas from the *PoWR* code, which models radiative transfer in NLTE expanding Wolf–Rayet atmospheres (Sander et al., 2015; Hamann & Gräfener, 2003).

In addition, one could learn about the SSS–phase of novae and the nova system parameters by studying their soft X–ray light curves. During the SSS–phase, the nova emission is observed to be highly variable, and modelling this variability could provide information on the photospheric radius, the binary inclination, the system extents and the structure of the ejecta. While the light curve is variable, the spectral shape does not change over time, suggesting obscuration effects rather than intrinsic changes in the nuclear burning. To model these X–ray light curves, we have designed the

flexible light curve simulation code *DaRT*, which combines binary dynamics with advanced Monte Carlo radiative transfer (*DaRT*: Dynamics and Radiative Transfer). We have successfully applied this *DaRT* code to disentangle some of the enigmatic light curves of novae during their SSS-phase. We reproduced the U Sco 2010 light curve model from the literature, by introducing three clumps of cold material from the companion star in orbit around the central white dwarf source. These clumps were proposed to originate from a fragmented accretion stream, signalling disk reformation in U Sco as soon as 22 days after the nova outburst. Furthermore, this light curve model provided evidence for the presence of an accretion disk corona, which was also observed in the nova spectra, with Doppler–smeared absorption lines from scattering on a relativistic plasma of electrons. The enigmatic soft X–ray light curve for V5116 Sgr 2005 was observed to transition between a low flux and high flux state, with a periodicity consistent with the orbital period. This behaviour could be explained by proposing an asymmetric accretion disk model, with a disk geometry imported to *DaRT* from a *.fits* data cube. This geometric light curve model was physically well–motivated, and will be the first model that is proposed since the *XMM–Newton* observations in 2007. The symbiotic nova V3890 Sgr 2019 was observed recently, and showed multiple dips in its X–ray light curve, that could not be explained by the companion star eclipse. In a medium of clumpy ejecta, the *EPIC–MOS* light curve data could be reproduced by assuming multiple clumps that were moving on highly eccentric trajectories. This allows us to better understand the messy environment around the white dwarf star shortly after the nova outburst.

Some further work could be added to our proposed light curve models, based on functionalities which are already implemented in *DaRT*. The Roche lobe shape of the binary companion could be added to our U Sco 2010 and V5116 Sgr 2005 models, to produce more realistic, self–consistent eclipses in the simulated light curves. Note how it would be straightforward to introduce the Roche lobe geometry from a *.fits* data cube into *DaRT*. The possibility to import turn–key geometries for the accretion stream and accretion bulge, based on restricted three–body calculations, would be especially useful for the V5116 Sgr and U Sco light curves. The latter nova system was observed a second time with *XMM–Newton* and showed a single asymmetric eclipse, which could be explained by obscuration effects from the reestablished accretion stream. All of the discussed novae were also targeted with other X–ray missions such as *Chandra* and *AstroSat*. Modelling these X–ray light curves in parallel would result in better constraints on the system parameters. With a possible extension of the *SKIRT* code towards full X–ray support, by including X–ray radiative processes involving both energy–dependent absorption and re–emission at the absorption sites (e.g. X–ray fluorescence), it would be possible to simulate spectral time maps self–consistently, instead of integrated light curves only. Note how it is already possible to account for relativistic electron scattering with corresponding Doppler shifts. The *DaRT* code provides a flexible tool to the astronomical community to test geometric models against observed light curve data, as we are committed to making the well–documented *DaRT* code publicly available (Vander Meulen et al., in prep.).

Bibliography

Arai, A., Yamanaka, M., Sasada, M., & Itoh, R. 2010, Central Bureau Electronic Telegrams, 2152

Ashok, N. M., Das, R. K., & Banerjee, D. P. K. 2010, Central Bureau Electronic Telegrams, 2153

Baes, M., Davies, J. I., Dejonghe, H., et al. 2003, MNRAS, 343, 1081

Baes, M., Gordon, K. D., Lunttila, T., et al. 2016, A&A, 590, A55

Baes, M., Verstappen, J., De Looze, I., et al. 2011, ApJS, 196, 22

Beardmore, A. P., Osborne, J. P., Page, K. L., et al. 2019a, The Astronomer's Telegram, 13104

Beardmore, A. P., Page, K. L., Markwardt, C. B., et al. 2019b, The Astronomer's Telegram, 13086

Bode, M. F. & Evans, A. 2008, Classical Novae, 2nd edn., Cambridge Astrophysics (Cambridge University Press)

Bryan, G. L. & Kwok, S. 1991, ApJ, 368, 252

Camps, P. & Baes, M. 2015, Astronomy and Computing, 9, 20

Camps, P. & Baes, M. 2018, ApJ, 861, 80

Camps, P. & Baes, M. 2020, Astronomy and Computing, 31, 100381

Casanova, J., José, J., García-Berro, E., Shore, S. N., & Calder, A. C. 2011, Nature, 478, 490

Darnley, M. J., Henze, M., Steele, I. A., et al. 2015, A&A, 580, A45

Das, R. K., Banerjee, D. P. K., & Ashok, N. M. 2010, Central Bureau Electronic Telegrams, 2157

Dobrotka, A., Retter, A., & Liu, A. 2008, A&A, 478, 815

Dobrzycka, D., Kenyon, S. J., Proga, D., Mikolajewska, J., & Wade, R. A. 1996, AJ, 111, 2090

Drake, J. J. & Orlando, S. 2010, ApJ, 720, L195

Ebisawa, K., Rauch, T., & Takei, D. 2010, Astronomische Nachrichten, 331, 152

Eggleton, P. P. 1983, ApJ, 268, 368

Elam, W., Ravel, B., & Sieber, J. 2002, Radiation Physics and Chemistry, 63, 121

Evans, A., Banerjee, D. P. K., Geballe, T. R., et al. 2019, The Astronomer's Telegram, 13088

Evans, P. A., Beardmore, A. P., Page, K. L., et al. 2009, MNRAS, 397, 1177

Evans, P. A., Beardmore, A. P., Page, K. L., et al. 2007, A&A, 469, 379

Frank, J., King, A., & Raine, D. 2002, Accretion power in astrophysics (Cambridge university press)

Fraser, O. J., Hawley, S. L., & Cook, K. H. 2008, AJ, 136, 1242

Gatuzz, E., Ness, J. U., Gorczyca, T. W., et al. 2018, MNRAS, 479, 2457

Gehrz, R. D., Truran, J. W., Williams, R. E., & Starrfield, S. 1998, PASP, 110, 3

Gilmore, A. C. & Kilmartin, P. M. 2005, IAU Circ., 8559, 2

Greiner, J. 1996, Supersoft X-Ray Sources, Vol. 472 (Springer)

Hachisu, I. & Kato, M. 2000a, ApJ, 536, L93

Hachisu, I. & Kato, M. 2000b, ApJ, 540, 447

Hachisu, I. & Kato, M. 2001, ApJ, 558, 323

Hachisu, I. & Kato, M. 2007, ApJ, 662, 552

Hachisu, I. & Kato, M. 2010, ApJ, 709, 680

Hamann, W. R. & Gräfener, G. 2003, A&A, 410, 993

Harrison, T. E., Johnson, J. J., & Spyromilio, J. 1993, AJ, 105, 320

Henyey, L. G. & Greenstein, J. L. 1941, ApJ, 93, 70

José, J., Hernanz, M., & Iliadis, C. 2006, Nucl. Phys. A, 777, 550

Jüttner, F. 1911, Annalen der Physik, 339, 856

Kahabka, P. & van den Heuvel, E. P. J. 1997, ARA&A, 35, 69

Kato, M. 1990, ApJ, 355, 277

Keppens, R., Nool, M., Tóth, G., & Goedbloed, J. P. 2003, Comput. Phys. Commun., 153, 317

Klein, O. & Nishina, T. 1929, Zeitschrift fur Physik, 52, 853

Liller, W. 2005, IAU Circ., 8559

Livio, M. 1994, in Interacting Binaries (Springer), 135–262

Livio, M. & Truran, J. W. 1992, ApJ, 389, 695

Manousakis, A., Revnivtsev, M., Krivonos, R., & Bozzo, E. 2010, The Astronomer's Telegram, 2412

Mason, E. 2011, A&A, 532, L11

Mason, E. 2013, A&A, 556, C2

Maxwell, M., Rushton, M., & Eyres, S. 2014, in ASP Conference 490 Stella Novae, ed. P. Woudt & V. Ribeiro, Vol. 490 (Astronomical Society of the Pacific), 205–206

Nelson, T. & Orio, M. 2007, The Astronomer's Telegram, 1202, 1

Ness, J. U., Beardmore, A. P., Osborne, J. P., et al. 2015, A&A, 578, A39

Ness, J. U., Orio, M., Starrfield, S., et al. 2019, The Astronomer's Telegram, 13124

Ness, J. U., Osborne, J. P., Henze, M., et al. 2013, A&A, 559, A50

Ness, J. U., Schaefer, B., Drake, J. J., et al. 2010, The Astronomer's Telegram, 2469

Ness, J. U., Schaefer, B. E., Dobrotka, A., et al. 2012, ApJ, 745, 43

Ness, J. U., Schwarz, G. J., Retter, A., et al. 2007a, ApJ, 663, 505

Ness, J. U., Starrfield, S., Schwarz, G., Page, K. L., & Osborne, J. P. 2007b, Central Bureau Electronic Telegrams, 1030

Nomoto, K. 1982, ApJ, 253, 798

Nomoto, K., Thielemann, F. K., & Yokoi, K. 1984, ApJ, 286, 644

Orio, M., Behar, E., Gallagher, J., et al. 2013, MNRAS, 429, 1342

Orio, M., Drake, J., Ness, J.-U., et al. 2019, The Astronomer's Telegram, 13083

Orio, M., Drake, J. J., Ness, J.-U., et al. 2020, arXiv e-prints, arXiv:2004.11263

Orio, M., Nelson, T., Luna, J., et al. 2010, The Astronomer's Telegram, 2451

Osborne, J. P., Page, K. L., Wynn, G., et al. 2010, The Astronomer's Telegram, 2442

Paczynski, B. 1977, ApJ, 216, 822

Page, K. L., Beardmore, A. P., Osborne, J. P., et al. 2019a, The Astronomer's Telegram, 13137

Page, K. L., Beardmore, A. P., Osborne, J. P., et al. 2019b, The Astronomer's Telegram, 13084

Page, K. L., Osborne, J. P., Kuin, N. P. M., et al. 2015, MNRAS, 454, 3108

Patterson, J., Kemp, J., Harvey, D. A., et al. 2005, PASP, 117, 1204

Pavana, M., Roy, N., Anupama, G. C., & Singh, K. P. 2019, The Astronomer's Telegram, 13092

Press, W. H., Teukolsky, S. A., Vetterling, W. T., & Flannery, B. P. 2002, Numerical Recipes Example Book (C++): The Art of Scientific Computing (Cambridge University Press)

Rauch, T., Orio, M., Gonzales-Riestra, R., et al. 2010, ApJ, 717, 363

Russell, R. W., Lynch, D. K., & Rudy, R. J. 2005, IAU Circ., 8579, 3

Saftly, W., Baes, M., & Camps, P. 2014, A&A, 561, A77

Saftly, W., Camps, P., Baes, M., et al. 2013, A&A, 554, A10

Sala, G., Hernanz, M., & Ferri, C. 2007, The Astronomer's Telegram, 1184

Sala, G., Hernanz, M., Ferri, C., & Greiner, J. 2008, ApJ, 675, L93

Sala, G., Hernanz, M., Ferri, C., & Greiner, J. 2010, Astronomische Nachrichten, 331, 201

Sala, G., Ness, J. U., Hernanz, M., & Greiner, J. 2017, A&A, 601, A93

Sander, A., Shenar, T., Hainich, R., et al. 2015, A&A, 577, A13

Schaefer, B. E. 2005, ApJ, 621, L53

Schaefer, B. E. 2009, ApJ, 697, 721

Schaefer, B. E. 2010a, ApJS, 187, 275

Schaefer, B. E. 2010b, arXiv e-prints, arXiv:1009.3197

Schaefer, B. E. 2013, in American Astronomical Society Meeting Abstracts, Vol. 221, American Astronomical Society Meeting Abstracts #221, 233.06

Schaefer, B. E. 2018, MNRAS, 481, 3033

Schaefer, B. E. 2019, in American Astronomical Society Meeting Abstracts, Vol. 234, American Astronomical Society Meeting Abstracts #234, 122.07

Schaefer, B. E., Pagnotta, A., Osborne, J. P., et al. 2010a, The Astronomer's Telegram, 2477

Schaefer, B. E., Pagnotta, A., Xiao, L., et al. 2010b, AJ, 140, 925

Schaefer, B. E. & Ringwald, F. A. 1995, ApJ, 447, L45

Schlegel, E. M., Schaefer, B., Pagnotta, A., et al. 2010a, The Astronomer's Telegram, 2419

Schlegel, E. M., Schaefer, B., Pagnotta, A., et al. 2010b, The Astronomer's Telegram, 2430

Singh, K. P., Girish, V., Anupama, G. C., & Pavana, M. 2019, The Astronomer's Telegram, 13102

Smith, D. A. & Dhillon, V. S. 1998, MNRAS, 301, 767

Sokolovsky, K. V., Orio, M., Page, K. L., et al. 2019, The Astronomer's Telegram, 13050

Starrfield, S., Bose, M., Iliadis, C., et al. 2020, The Astrophysical Journal, 895, 70

Starrfield, S., Sparks, W. M., & Shaviv, G. 1988, ApJ, 325, L35

Starrfield, S., Sparks, W. M., & Truran, J. W. 1985, ApJ, 291, 136

Steinacker, J., Baes, M., & Gordon, K. D. 2013, ARA&A, 51, 63

Strader, J., Chomiuk, L., Aydi, E., et al. 2019, The Astronomer's Telegram, 13047

Teyssier, F., Boyd, D., Sims, F., et al. 2019, Eruptive Stars Information Letter, 43, 2

Thoroughgood, T. D., Dhillon, V. S., Littlefair, S. P., & Marsh, T. R. 2001, MNRAS, 327, 1323

Truran, J. W. & Livio, M. 1986, ApJ, 308, 721

van den Heuvel, E. P. J., Bhattacharya, D., Nomoto, K., & Rappaport, S. A. 1992, A&A, 262, 97

van Rossum, D. R. 2012, ApJ, 756, 43

van Rossum, D. R. & Ness, J. U. 2010, Astronomische Nachrichten, 331, 175

Vanbeveren, D. 2000, Astrophysics and Space Science Library, Vol. 255, The Evolution of Binaries (Springer), 139

Vander Meulen, B., Ness, J. U., & El Mellah, I. in prep., 2020

Verstocken, S., Van De Putte, D., Camps, P., & Baes, M. 2017, Astronomy and Computing, 20, 16

Waagen, E., Shida, R., Linnolt, M., Bedient, J., & Pearce, A. 2005, IAU Circ., 8559, 4

Webbink, R. F., Livio, M., Truran, J. W., & Orio, M. 1987, ApJ, 314, 653

Whelan, J. & Iben, Icko, J. 1973, ApJ, 186, 1007

Wilms, J., Allen, A., & McCray, R. 2000, ApJ, 542, 914

Wolf, W. M., Bildsten, L., Brooks, J., & Paxton, B. 2013, ApJ, 777, 136

Xia, C., Teunissen, J., El Mellah, I., Chané, E., & Keppens, R. 2018, ApJS, 234, 30